Annual Report 2018

HI JENA

HELMHOLTZ

Helmholtz Institute Jena

Helmholtz Institute Jena
Fröbelstieg 3
07743 Jena
www.hi-jena.de

seit 1558

GSI

HZDR
HELMHOLTZ
ZENTRUM DRESDEN
ROSSENDORF

DESY
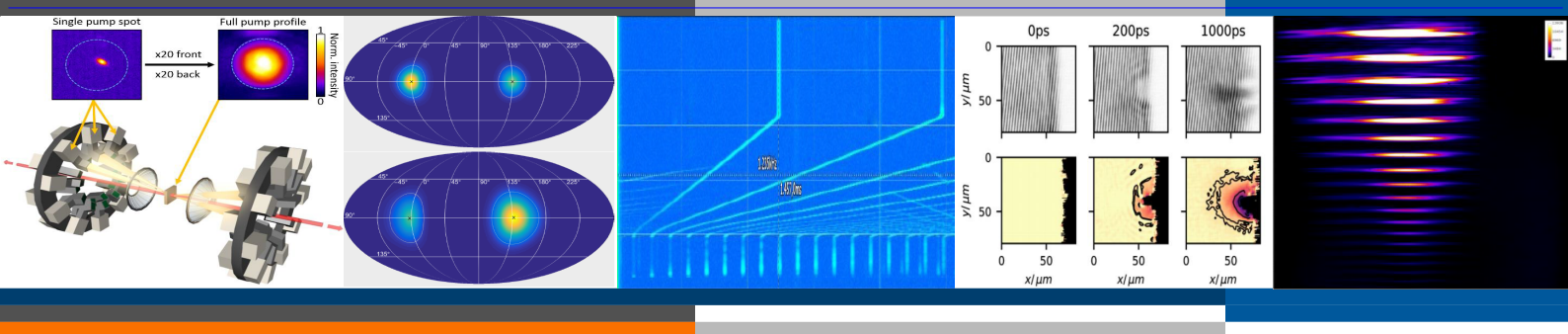
Helmholtz Institute Jena

Annual Report 2018

Contents

Laser Particle Acceleration

Photon and Particle Spectroscopy   41

Theory

Introduction

The institute's mission is excellence in fundamental and applied research based on high-power lasers, particle accelerators, and X-ray science, addressing the coupling of intense light with matter. One particular focus of the institute is the research and the development of advanced instrumentation for dedicated experiments at the flagship facilities for extreme matter research, the EU-XFEL at Hamburg and the international FAIR project at Darmstadt. With this Annual Report for 2018, we present an overview of the achievements in science and technology made at the institute over the last year.

Various research highlights have been achieved using its own experimental facilities at Jena (high-power laser POLARIS and JETI200), the ion storage rings and the PHELIX laser at GSI campus Darmstadt, the photon facilities at DESY and the facilities of collaborative partners. Some examples of are: Laser Development "High-flux ultrafast extreme-ultraviolet photoemission spectroscopy at 18.4 MHz pulse repetition rate"; Laser-Particle acceleration "Laser Acceleration of Highly Energetic Carbon Ions Using a Double-Layer Target Composed of Slightly Underdense Plasma and Ultrathin Foil"; Atomic and Nuclear Astrophysics/Spectroscopy "Approaching the Gamow Window with Stored Ions: Direct Measurement of ^{124}Xe(p,γ) in the ESR Storage Ring" Theory "All-optical signatures of quantum vacuum nonlinearities in generic laser fields".

One particularly important event for the Friedrich-Schiller-University Jena was in 2018 the decision of granted funding for the Cluster 'Balance of the Microverse' by the German "Exzellenzstrategie" for the following seven years. In the Cluster of Excellence 'Balance of the Microverse', the University cooperates with its University Hospital and external research institutions – among them the Helmholtz Institute Jena, underlining the close collaboration of HI Jena with the university. Moreover, as a result of an accumulated expertise in the X-ray physics and in order to further consolidate the institute's efforts in the development of laser-based X-ray sources, a new research collaboration (Forschungsgruppe) has been established at HI Jena since May 2018. The funding has been awarded by the Thüringer Aufbaubank and the European Social Fund. The new research collaboration builds on expertise in the fields of laser development, X-ray optics and detector technology already existing at the institute. Its primary goal is to prepare access to novel advances in the interlocking fields of X-ray generation and detection for potential users in industry and medicine by realizing demonstrator experiments featuring high-resolution polarimetric and imaging measurements in the X-ray spectral range. Also, we are pleased to mention that the ATHENA ("Accelerator Technology Helmholtz iNfrAstucture") project has been approved for funding. This project strongly enhances a focus on the accelerator research and development based on the resources of all six Helmholtz accelerator institutions (GSI with the Helmholtz Institute Jena, as well as DESY, Jülich Research Centre, Helmholtz Centre Berlin, Helmholtz Centre Dresden-Rossendorf HZDR and KIT).

Further progress has been achieved with respect to the ongoing efforts for the realization of the institute's additional new building at the campus of the FSU Jena, which is financed by the Federal State of Thuringia. With the completion of the architecture competition, "Neubau Helmholtz Institut Jena" the last milestone has been achieved on the way towards civil construction. It is expected that the construction activities will start in autumn 2019.

A further important task of HI Jena is the education of students in science and technology related to the physics of extreme matter physics. Meanwhile, structured PhD education is well-

11

established within the framework of the "Research School of Advanced Photon Science" (RS-APS) of HI-Jena which interacts closely with the GSI Graduate School HGS-HIRe as well as with the local Graduate Schools at FSU Jena under the umbrella of the Graduate Academy of the university. Many students make use of the benefits offered by the research school, e.g. most students regularly use the personal travel money offered to attend conferences to present their own research work. The Research School has now close to 60 participating doctoral students, of whom more than 50% are financed via 3rd party funding.

Status of the Research School of Advanced Photon Science of the Helmholtz Institute Jena

R. Märtin[1], Ch. Spielmann[1,2] , G. Weber[1], and Th. Stöhlker[1,2,3]

[1]HI-Jena, Jena, Germany; [2]University Jena, Jena, Germany; [3]GSI, Darmstadt, Germany

Over six years past meanwhile since the foundation of Research School of Advanced Photon Science of the Helmholtz Institute Jena in 2012. The Research School was established for all students associated to the Helmholtz Institute Jena and its research mission. Although there were already existing PhD programs at the Helmholtz partner centers, there was the need for own local structured PhD education one the one hand due to the remoteness on the campus of the Friedrich-Schiller University Jena and on the other hand due to the research at the interface of optics and accelerator technology.

Since the foundation the number of participating student steadily increased. In the year 2018 over 50 students working directly at the institute or the partner centers GSI, DESY or HZDR took part in the program of the school. Almost the half of the students is third party funded, while the rest of the doctoral students either receiving a scholarship or have a doctoral position supported by the Helmholtz Institute Jena. In addition every participant has its own annual travel money to visit conferences and workshops. The offered travel money is of great importance for the professional and international network of the future researcher and most of the students take advantage of their yearly budget.

The financial support is among other things an incentive to participate actively in the academic and soft skill program offered by the research school of the Helmholtz Institute Jena and its collaborating partners the HGS-HIRe Graduate School for FAIR and the Graduate Academy of the FSU Jena.

Together with HGS-HIRe RS-APS organizes already since six years an annual Lecture Week In 2018 the Lecture Week addressed the interface and interplay between atomic physics and nuclear physics. Hosted by the "Jugendbildungsstätte Hütten" with its stimulating atmosphere, Carsten Brandau (U Giessen), Sven Bernitt (U Heidelberg), Andrey Volotka (HI Jena) and the participating students discussed together various aspects of this crossdisciplinary topic.

The internationalization of the school is well developing, while the percentage of female participants is stagnating. Meanwhile over 35% of the doctoral students are foreigners while 5% are female.

To fully utilize the developing potential of the structures for PhD education at the Helmholtz Institute Jena, the research school applied for the "International Helmholtz Research school" program in 2018 together with the PLAS@PAR school at Sorbonne Universities. Unfortunately the application was rejected this time, but Helmholtz Institute Jena is encouraged to apply once more in 2019 for an International Helmholtz Research School.

Finally in 2018 four members of the Graduate School successfully completed their doctoral studies.

Figure 1: The participants of the sixth joint Lecture Week of HGS-HIRe and RS-APS in Hütten. The photograph was taken during an excursion to the pumped-storage plant PSW Hohenwarte.

High Power Laser Development

Current status and future development of the POLARIS laser system

M. Hornung[1,2 ,#], S. Keppler[1], I. Tamer[1] A. Kessler[1], M. Mäusezahl[2], M. Reuter[2], G.A. Becker[2], F. Schorcht[1], M. Hellwing[2], J. Hein[1,2], M.C. Kaluza[1,2]

[1]Helmholtz-Institute Jena, Germany; [2]Institute of Optics and Quantum Electronics, Jena, Germany.

We report on the operation and an ongoing upgrade of the POLARIS laser system [1]. In 2018, an extensive experimental campaign was carried out in order to investigate the influence of the temporal intensity contrast on proton acceleration. A key element for the investigations during this experimental campaign was the successful installation and implementation of a plasma-mirror in the POLARIS laser system to further enhance the temporal contrast [2].

After the experimental campaign, which lasted until august 2018, an upgrade of POLARIS started. Three parts of the laser were and will be further optimized.

At first, the free aperture of the pulse compressor was previously limited to a diameter of 140 mm due to a specific design limitation of the used vacuum chambers. A flange with a diameter of 320 mm, where the laterally dispersed laser pulse travels through during compression, was increased in diameter to 400 mm. With this modification the pulse compressor (as well as the following transport beamline) supports now a circular aperture of 160 mm, which means an increase of free aperture area and therewith peak power of 30 %. Since the acceptance aperture of the pulse compressor is currently limiting POLARIS's peak power the experimental performance directly benefits from this improvement.

Secondly an adaptive optics system was installed in front of the fifth and final amplifier A5. The output energy of this amplifier and hence of the whole laser system is currently limited by the quality of the near field profile of the amplified pulses (cf. [1]). Due to the non-imaging multi-pass design with 17 passes through the active material and 90 m of propagation the amplifier is very sensitive to wavefront aberrations. Basically the influence on the near field profile originating in three types of aberrations should be minimized: 1. Wavefront aberrations from the seed-pulses which were amplified by A4. 2. Wavefront aberrations originating from the large aperture multi-pass mirrors (more than 35 reflections). 3. Wavefront aberrations of the active material due to the optical pumping and electronic stimulation. The adaptive optics system consists of a wavefront sensor based on lateral shearing interferometry (Phasics SID 4, France) with a resolution of 160 x 120 phase sampling points and a large aperture deformable mirror. The deformable mirror (ISP MD60-C53, France) based on a patented stepper motor design with 53 actuators has an active aperture with a diameter of 60 mm (clear aperture 70 mm). This part of the POLARIS upgrade is still ongoing and will be finished soon.

The third major part of the upgrade was the installation of a newly developed active stretcher in the POLARIS laser chain. This active stretcher is used to stretch high-contrast seed pulses to nanosecond pulse durations. A first prototype of an active stretcher was demonstrated in 2017 [3] on a separate optical table. Since then this active stretcher was continuously used in experiments during the last two years due to its significantly increased pulse duration stability compared to the conventional and formerly used pulse stretcher. Due to stability and space constraints an implementation of the active stretching technology onto the optical tables of POLARIS was necessary. In Figure 1 a photography of the newly developed active stretcher is
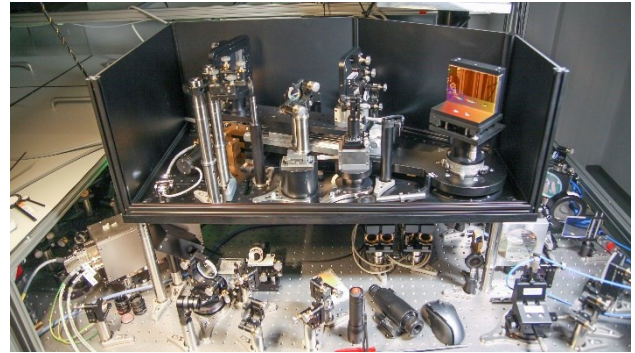
Figure 1: Active nanosecond stretcher. The amplifier is built on the optical table and the intracavity pulse stretcher is located in the black housing above the amplifier.

shown. The Offner-type stretcher uses a spherical telescope with focal lengths of f = 300 mm and f = -150 mm and a high efficiency (94 %) gold-grating with 1480 lines/mm from Horiba Jobin-Yvon (France). The active stretcher increases the pulse duration, which could be freely chosen, up to a few nanoseconds. Currently, the amplified stretched pulses exhibit a bandwidth of 25 nm (FWHM) centred at 1030 nm in a TEM_{00}-mode. The pulse energy is limited to 500 µJ due to an intermediate focal spot in the stretcher which is unavoidable with a spherical Offner telescope. Using the tiled-grating compressor the stretched pulses could be compressed to a pulse duration of 110 fs (FWHM).

References

[1] M. Hornung, H. Liebetrau, S. Keppler, A. Kessler, M. Hellwing, F. Schorcht, G. A. Becker, M. Reuter, J. Polz, J. Körner, J. Hein, and M. C. Kaluza, "54 J pulses with 18 nm bandwidth from a diode-pumped chirped pulse amplification laser system", Optics Letters 41, 21, 5413-5416 (2016).

[2] S. Keppler, M. Hornung, G.A. Becker, I. Tamer, A. Massinger, F. Irshad, M. Hellwing, F. Schorcht, A. Kessler, J. Hein, and M. C. Kaluza, "POLARIS – current status and experimental results", Helmholtz-Institute annual report (2017).

[3] H. Liebetrau, M. Hornung, S. Keppler, M. Hellwing, A. Kessler, F. Schorcht, J. Hein, and M. C. Kaluza, "Intracavity stretcher for chirped-pulse amplification in high-power laser systems", Optics Letters 42, 2, 326-329 (2017).

#Marco.Hornung@uni-jena.de

JETi200 high intensity upgrade

A. Sävert[1,2], G. Schäfer[1], B. Beleites[2], F. Ronneberger[2], C. Zepter[2], A. Seidel[2], and M. Zepf[1,2]

[1]GSI Helmholtz Institut Jena, Jena, Germany; [2]Friedrich Schiller Universität Jena, Jena, Germany

The JETi200 laser system is operated at the Helmholtz Institute Jena. It delivers up to 4 J on target within a pulse duration of 17 fs. This results in a peak power in excess of 200 TW. After successful experiments in the field of Surface High Harmonic Generation and Laser Wakefield Acceleration, the laser was upgraded in the 2018 summer shut down. The goal of this shut down was to boost the peak intensity in the focal spot.

First a fourth pump laser (Titan 6, Amplitude Technologies) for the final amplifier was installed. This lead to an increase in pump energy from 15 J to 21 J. Hence, the amplified energy of the uncompressed JETi beam was increased from 5.5 J to 7.8 J.

The additional energy made it necessary to increase the beam diameter from 100 mm to 120 mm to decrease the fluence on the beam optics along the beamline. This was done by exchange the existing refractive telescope to an all reflective expanding telescope. Thus chromatic aberrations which play a dominant role for these broadband laser pulses were reduced at the same time.

Nevertheless, there were still chromatic aberrations left which became apparent in the focal spot. In Fig. 1 the focal spot is shown as it was recorded during the LWFA beam time in spring 2018. Imaging the full spectral bandwidth onto the focus diagnostic resulted in an elongated focal spot with an elliptical shape. Using a band pass filter to narrow the spectrum in front of the CCD gives a nearly diffraction limited focal spot.

full spectrum (FWHM: 80 nm)
FWHM: 55 µm x 25 µm, q=0.46

10 nm band pass
FWHM: 25 µm x 23µm, q=0.45
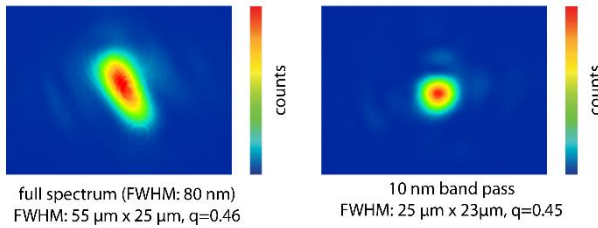
Figure 1: Optimized focal spot using a deformable mirror and an F/25 off-axis parabola resulting in a vacuum peak intensity of 5×10^{18} W/cm^2 (a_0=1.7).

The very good quality factor of q=0.45, meaning that 45% of the total energy is located inside the FWHM of the focal spot, is achieved by using a deformable mirror (ISP Systems) to remove remaining wavefront aberrations.

Residual chromatic aberrations are due to an uncompensated angular chirp in the beam. The rotation stages in the pulse compressor which were delivered by Amplitude Technologies aren´t sensitive enough to align the compressor grating parallel to one and another. Based on the grating mounts of the POLARIS laser, new mounts were designed to attribute this issue. At the same time, the vertical dis-

tance between the gratings had to be reduced to avoid clipping of the now bigger laser beam. The result of this design is shown in Fig. 2.
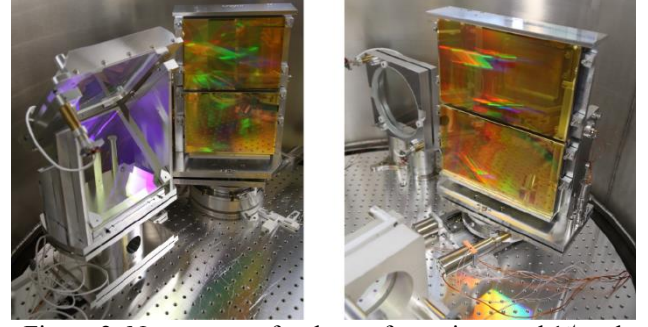
Figure 2: New mounts for the rooftop mirror and 1st and 4th compressor grating (left) and for the 2nd and 3rd compressor grating (right).

At the same time the actuators of the mounts were exchanged and now every grating pair has a local tip and tilt option to make them parallel in respect to each other. Global tip, tilt and twist option is available to align the two grating pairs with respect to each other. In total, the sensitivity was increased by a factor of 200. The minimal rotational increment is now 0.15 µrad and allows complete control of the angular chirp down to 1 nrad/nm. The experimental results are shown in Fig. 3. Here the same focusing geometry was used as before. The change in f-number is due to the increased beam diameter.

full spectrum (FWHM: 80 nm)
FWHM: 22 µm x 21 µm, q=0.48

10 nm band pass
FWHM: 23 µm x 21µm, q=0.47
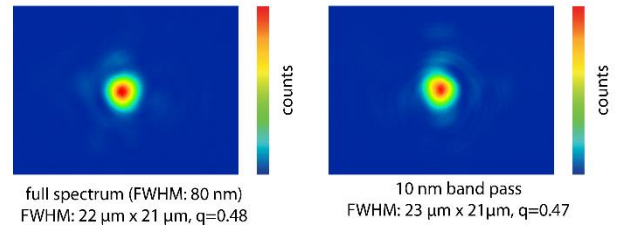
Figure 3: Optimized focal spot using a deformable mirror and an F/21 off-axis Parabola resulting in a vacuum peak intensity of 1.5×10^{19} W/cm^2 (a_0=3.0).

The angular chirp is now completely removed resulting in a diffraction limited focal spot not only for the band pass filtered beam but also for the full bandwidth.

First experiments in the field of LWFA resulted in a boosted maximum electron energy from 600 MeV to more than 850 MeV.

Femtosecond 16 channel multicore fiber laser system

A. Klenke[1,2], M. Müller[2], H. Stark[2], A. Tünnermann[1,2,3] and J. Limpert[1,2,3]

[1]Helmholtz-Institute Jena, Fröbelstieg 3, 07743 Jena, Germany;

[2]Institute of Applied Physics, Abbe Center of Photonics, Friedrich-Schiller-Universität Jena, Albert-Einstein-Str. 15, 07745 Jena, Germany;

[3]Fraunhofer Institute for Applied Optics and Precision Engineering, Albert-Einstein-Str. 7, 07745 Jena, Germany

Coherent combination of multiple laser amplifiers has made in possible to overcome physical performance limitations and has enabled the most powerful femtosecond fiber laser systems to date. These continuous performance improvements have allowed to open up new applications in industry and science. Theoretically, adding additional amplifiers will allow for further scaling while maintaining a high efficiency of the combination process. However, this comes with an equal increase of complexity, footprint and cost, which again sets an effective performance limit. Therefore, new integrated amplifier architectures are of great interest. The proposed architecture is based on multicore fibers, containing multiple amplification channels in a single fiber [1]. Additionally, the beam-splitting and -combination and the phase stabilization are realized with compact and preferably monolithic components. For the required active phase stabilization, a scalable algorithm has been developed [2]. Hence, the number of discrete components is basically independent from the number of parallel amplifier channels and opens up a high scaling potential.
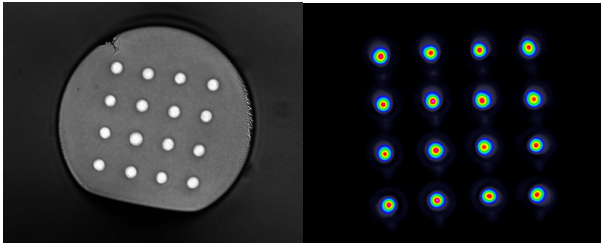
Fig. 1: Microscope image of the end-facet of the 16 core fiber and camera image of the output

A first prototype system based on this laser architecture was realized using an in-house designed step-index fiber with 4x4 cores (19 μm diameter each) in rectangular orientation (see Fig. 1). A novel and cost-effective production process was employed. The fiber possesses a shared pump cladding with 340 μm diameter to allow the use of a single semiconductor pump diode. First, combination of 40 picosecond pulses was realized with up to 80% combination efficiency. Measurements showed that the combined beam is of excellent quality (M² < 1.2x1.1), even surpassing the quality of the beams emitted from the single channels due to the combination related beam cleaning effects. An excellent power stability value was also determined. Later on, the frontend of the laser was replaced with one emitting stretched femtosecond pulses. Additionally, the combined pulses are recompressed to the femtosecond regime in a grating compressor
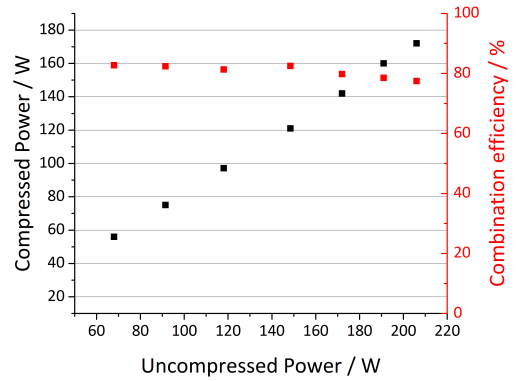
Fig. 2: Combination efficiency depending on the combined average power and the corresponding compressed average power

. The achieved performance values are shown in Fig. 2. Again, a combination efficiency of around 80% could be maintained over the full average power range up to a (uncompressed) combined power of 200 W. After compression, 170 W of average power was achieved. Additional tests have shown an average power capability of the fiber of up to 1.4 kW, without visible signs of modal instabilities.

Further development on this technology will concentrate on realizing multicore fibers with larger core diameters and further increasing the channel count. This will offer the possibility to move fiber laser technology to the high pulse energy regime without sacrificing the intrinsic advantages of optical fibers.

References

[1] A. Klenke, M. Müller, H. Stark, F. Stutzki, C. Hupel, T. Schreiber, A. Tünnermann, and J. Limpert, "Coherently combined 16-channel multicore fiber laser system," Opt. Lett. **43**, (2018).

[2] A. Klenke, M. Müller, H. Stark, A. Tünnermann, and J. Limpert, "Sequential phase locking scheme for a filled aperture intensity coherent combination of beam arrays," Opt. Express **26**, (2018).

1 kW average power ultrafast Tm-doped fiber laser

M. Gebhardt,[1,2] C. Gaida,[2] T. Heuermann,[1,2] Z. Wang,[2] C. Jauregui,[2] J. Rothhardt,[1,2,3] A. Tünnermann[1,2,3] and J. Limpert,[1,2,3,#]

[1]Helmholtz-Institute Jena, Fröbelstieg 3, 07743 Jena, Germany; [2]Institute of Applied Physics, Abbe Center of Photonics, Friedrich-Schiller-Universität Jena, Albert-Einstein-Str. 15, 07745 Jena, Germany; [3]Fraunhofer Institute for Applied Optics and Precision Engineering, Albert-Einstein-Str. 7, 07745 Jena, Germany

Mature laser systems that deliver energetic ultrashort pulses are important tools in industry and in fundamental research. For a large number of scientific investigations, it is the strength of the involved electromagnetic forces and thus, the peak intensity of the light, which is the essential and enabling laser parameter. That is in particular true for highly nonlinear phenomena like the generation of high-order harmonic radiation (HHG) [1]. This process has become extremely popular in recent years, as it allows to produce radiation in the XUV or even in the soft X-ray regime with laser-like coherence (using setups with footprints of a few m²). However, when it comes to turning such laboratory demonstrations into real world applications, i.e. when using the coherent XUV/soft X-rays for subsequent experiments, a certain photon flux is required in order to enable reasonable data acquisition times and good signal to noise ratios. As a result, the community is moving towards laser sources that can operate at higher and higher repetition rates and therefore, produce more HHG flux [2].

Additionally, the HHG driving laser wavelength plays an important role for the achievable photon energy cut-off. In fact, it has been identified that an operation wavelength around 2 µm is most desirable to efficiently address photon energies within the so-called water window (280-530 eV), which is an interesting spectral region for spectroscopy of highly charged ions [3] and coherent diffractive imaging of organic molecules with element-specific contrast [4].

Following these application-driven demands, thulium(Tm)-doped fiber lasers represent a promising solid-state laser concept that has been proven to be suitable for the generation of multi-GW-, 100 fs-pulses at a carrier wavelength of 1.9 µm [5]. Herein, we demonstrate the average power handling capabilities of this technology by reporting the highest average power output of an ultrafast single channel fiber laser with diffraction-limited beam quality to date. The developed laser system is seeded by an 80 MHz fiber-based oscillator and built based on the chirped-pulse amplification (CPA) technique. More details can be found in ref. [6]. The key components of the high power section are two pump clusters (each delivering a pump power of almost 1 kW at 793 nm), a Tm-doped photonic crystal fiber with 36 µm mode-field diameter (allowing for sufficient mitigation of nonlinear effects and efficient amplification), and highly efficient dielectric gratings (used in the pulse compressor of the CPA system with >90% efficiency). Fig. 1 depicts the power slope of the main amplifier as well as simulation results. The maximum output average power of 1150 W was pump power limited

and allowed for a record compressed output of 1060 W (after the grating-based pulse compressor). At this point, the beam quality was confirmed to be close to diffraction-limited (M²<1.1) and a pulse duration of 265 fs was deduced based on an autocorrelation (AC) measurement (Fig. 2). The laser system described herein delivers 13 µJ pulses, which corresponds to a peak power of about 50 MW at 80 MHz repetition rate.
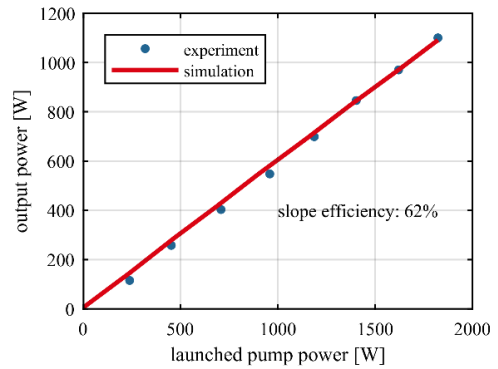
Fig. 1: Power slope of the ultrafast Tm-doped fiber laser
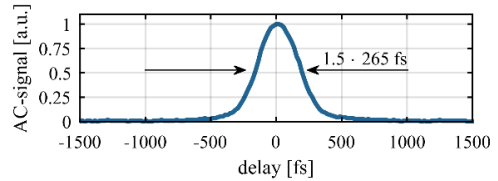
Fig. 2: Measured AC trace at the highest output power

Outlook Our future work will include further power and energy scaling to exploit the full potential of ultrafast Tm-fiber lasers as well as pushing their output pulse durations to the few-cycle regime via nonlinear pulse compression [7]. The developed laser sources will be used for high-flux HHG with photon energies within the water window.

References

[1] T. Popmintchev et al., Nat. Phot. 4: 822 (2014).
[2] S. Hädrich et al., LSA 4(8), e320 (2015).
[3] W. Nörtershäuser, Hyperfine Interact 199: 131, (2011).
[4] K. Giewekemeyer et al., Opt. Express 19, 1037 (2011).
[5] M. Gebhardt et al., Europe-EQEC CJ_11_1J (2017)
[6] C. Gaida et al., Opt. Lett. 43, 5853 (2018).
[7] M. Gebhardt et al., Opt. Lett. 42, 4179 (2017)

[#]jens.limpert@uni-jena.de

POLARIS-Seeded Non-Collinear Optical Parametric Amplifier as an Optical Probe for Relativistic Laser-Plasma Interactions

I. Tamer[1,2], S. Keppler[1,2], M. Hornung[1,2], M. Hellwing[2], F. Schorcht[1], M.C. Kaluza[1,2]

[1]Helmholtz-Institute Jena, Germany; [2]Institute of Optics and Quantum Electronics, Jena, Germany.

Understanding the complex processes that occur within relativistic laser-plasma interactions can yield improvements in laser-based ion acceleration, which is promising for various scientific and medical applications. With the POLARIS [1] laser system at the Helmholtz-Institute Jena, the focused on-target intensity of over 10^{20} W/cm^2 is sufficient to generate a plasma and accelerate ions within the Target Normal Sheath Acceleration (TNSA) regime. Due to the complex dynamics of these relativistic laser-plasma interactions, however, it is challenging to determine the optimum laser and plasma configurations that provide the most energetic ions. Here, an optical probe in the form of an ultrashort laser pulse allows access to significant events via a direct imaging of the interaction with high spatial and temporal resolution, through which relevant information about the plasma density evolution [2] can be extracted.

For the ultrashort pulse to adequately spatially and temporally probe the interactions, the beam size must be large enough (1 mm) to capture the entire interaction region and short enough to fit into a time frame (10 fs) that is significantly shorter than the pulse duration of the POLARIS laser pulse (100 fs). In addition, the spectral profile cannot overlap with the fundamental or harmonic frequencies of the POLARIS laser due to strong plasma emission and reflection. Furthermore, the temporal jitter between the probe and the POLARIS laser must be minimized and the system must be compact and movable. Under these constraints, the ultrashort optical probe was designed, simulated, constructed, and optimized as a POLARIS-seeded non-collinear optical parametric amplifier (NOPA) system.

A schematic of the NOPA setup is shown in Fig. 1. A pulse from the POLARIS oscillator was stretched, amplified to 2 mJ, and compressed to 100 fs in a chirped pulse amplification (CPA) setup to seed the NOPA. The seed pulse is then split into two paths, with 2 µJ for white light generation (WLG) within a YAG crystal and the remaining 2 mJ reserved for the second harmonic generation (SHG) within a KDP crystal. The WLG and SHG pulses meet within a
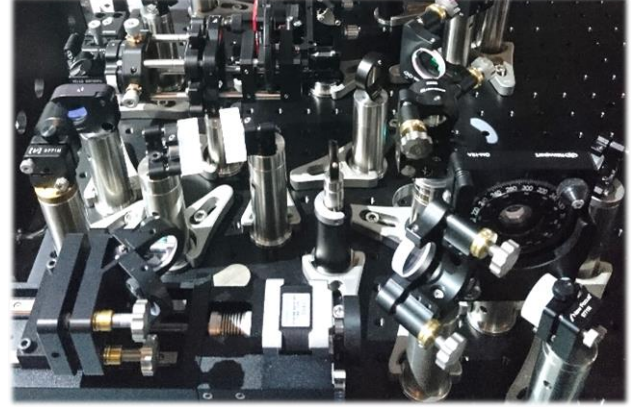
Figure 2: Image of the compact NOPA setup.

BBO crystal under an optimized angle for broadband WLG amplification with a single pass gain in excess of 10^4. Using self-referenced spectral interferometry (Wizzler), the final pulse duration was measured to be 10 fs full-width at half maximum (FWHM). The ultrashort probe pulse intensity of 10^{11} W/cm^2 is sufficiently low to illuminate the desired interaction region without ionizing the target. The NOPA system, seen in Fig. 2, fits within 40 x 40 cm^2. The current setup is ready to be tested under a chirped pulse probing scheme [3] in an upcoming experimental campaign, with live diagnostics for the pulse duration, spectrum, energy, and temporal jitter (setup schematic in Fig. 3). With the successful commissioning of this ultrashort optical probe at the POLARIS laser system, new insight into the intricate dynamics of relativistic laser-plasma interactions can be achieved.
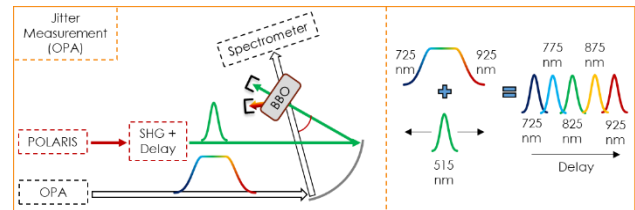
Figure 3: Schematic of the live temporal jitter diagnostic.

References

[1] M. Hornung, H. Liebetrau, S. Keppler, A. Kessler, M. Hellwing, F. Schorcht, G. A. Becker, M. Reuter, J. Polz, J. Körner, J. Hein, and M. C. Kaluza, Opt. Lett. 41, 5413–5416 (2016).

[2] M.B. Schwab, A. Sävert, O. Jäckel, J. Polz, M. Schnell, T. Rinck, L Veisz, M. Möller, P. Hansinger, G.G. Paulus, and M.C. Kaluza, Appl. Phys. Lett. 103, 19111 (2013).

[3] K. Nakagawa, A. Iwasaki, Y. Oishi, R. Horisaki, A. Tsukamoto, A. Nakamura, K. Hirosawa, H. Liao, T. Ushida, K. Goda, F. Kannari, and I. Sakuma, Nat. Photonics 8, 695–700 (2014).

Figure 1: Schematic and results of the NOPA probe.

Spatio-Temporal Thermal Profile Modeling of Joule-class Yb^{3+}-Based Laser Amplifiers

I. Tamer[1,2], S. Keppler[1,2], J. Körner[2], M. Hornung[1,2], J. Hein[1,2], M.C. Kaluza[1,2]

[1]Helmholtz-Institute Jena, Germany; [2]Institute of Optics and Quantum Electronics, Jena, Germany.

An optimization of the POLARIS laser system at the Helmholtz-Institute Jena towards higher laser pulse energies can enrich current investigations on laser-based ion acceleration regimes such as Target Normal Sheath Acceleration (TNSA) and Radiation Pressure Acceleration (RPA). The energy of the laser pulse is amplified to the multi-Joule level in the final two amplifier stages, where large beam diameters are required to reduce the laser fluence below the laser-induced damage threshold of the active materials and long propagation distances are necessary due to the multi-pass configuration. These requirements embolden the impact of strong wavefront aberrations that the active materials, which are pumped with over 250 J for the A4 (4th amplifier) and over 1kJ for the A5 (5th and final amplifier), imbue onto the incident seed beam with every pass and limit the final energy and focusability of the laser system. Such wavefront aberrations form due the spatio-temporal thermal [1] and electronic [2] refractive index changes induced by the pump pulse and the population inversion and can be modeled [3] with the knowledge of the single-pass gain, spatial fluorescence profile, and spatio-temporal thermal profile of the pumped active material.

For complicated 3D pumping configurations with high pump energies, such as those present in the A4 (Fig. 1) and A5 amplifiers, however, the complete characterization of the spatio-temporal thermal profile is challenging to accomplish with conventional methods. Utilizing a thermal infrared imaging camera, for example, only allows access to the surface temperatures of the pumped active material with a limited temporal resolution. Here, with in-depth knowledge of the doping-dependent material parameters and calculations of the inversion-corrected pump

Figure 2: A slice through the simulated pumped active material within the A4 is shown (top). The measured (solid) and simulated (dashed) front and back thermal profiles are displayed (bottom) for various times within the pump cycle.

depletion, a complex highly accurate numerical model [4] can be constructed, benchmarked, and verified using surface thermal measurements. The results of the thermal model for the A4 pumping configuration are displayed in Fig. 2, which have an excellent agreement with the measurements with an RMS discrepancy throughout the pump cycle of less than 1.5% of the maximum temperature.

The results of this spatio-temporal thermal model can now be utilized to calculate the forms of the wavefront aberrations that the pumped active material within the Joule-class A4 amplifier imbues onto the incident seed beam per pass. Furthermore, the ideal form for the pump distribution that is optimized both for the spatial gain profile and for the wavefront aberrations can be constructed to provide an improved focusability and higher final energy for the POLARIS laser system.

Figure 1: Schematic of the 3D pumping configuration of the A4 multi-pass amplifier at POLARIS with an example of a single (top left) and full (top right) pump profile.

References

[1] S. Chénais, F. Druon, S. Forget, F. Balembois, and P. Georges, Prog. Quant. Electron. 30, 89 (2006).

[2] O.L. Antipov, D.V. Bredikhin, O.N. Eremeykin, A. P. Savikin, E.V. Ivakin, and A.V. Sukhadolau, Opt. Lett. 31, 763 (2006).

[3] I. Tamer, S. Keppler, M. Hornung, J. Körner, J. Hein, and M.C. Kaluza, Laser Photonics Rev. 12, 2 (2018).

[4] I. Tamer, S. Keppler, J. Körner, M. Hornung, M. Hellwing, F. Schorcht, J. Hein, and M.C. Kaluza, manuscript submitted.

Diode pumped Q-switched cryogenic cooled bulk Tm:YAG laser oscillator

Jürgen Reiter[1,2], Jörg Körner[1,2], Joachim Hein[1,2], and Malte C. Kaluza[1,2]

[1]Helmholtz Institute Jena, Germany; [2]Institute of Optics and Quantum Electronics, Friedrich-Schiller-University, Germany

Lasers operating in the mid-IR are desirable for spectroscopy, sensing and medical related applications, as well as for seeding or pumping middle-infrared optical parametric oscillators. In addition highly energetic ultra short pulses in this wavelength region could be of interest for particle acceleration, high harmonic generation and THz-generation. One promising candidate for the laser material to realize such lasers is Cr^{2+}:ZnSe. Its broad emission spectrum around 3 μm enables to achieve femtosecond pulses in the mid-IR. Due to the short lifetime of a few micro seconds diode lasers cannot be used for pumping. However, short pulsed lasers emitting between 1800 nm and 1900 nm would be ideal [1].

Our approach is to build a high energy laser system based on Tm^{3+}-doped media. Thulium doped materials emit in the range between 1800 nm and 2050 nm, while they can be excited with available high power laser diodes emitting close to 785 nm. Due to the so called cross relaxation process, allowing to obtain two laser photons for each absorbed pump photon, the quantum defect is still in the range of just 20%.
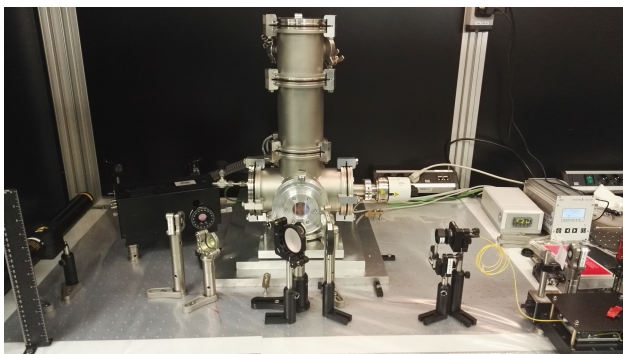
Figure 1: Setup of the cryogenic cooled Tm:YAG oscillator. Used is a stable cavity with approximately 3.5 m length and a 4 pass pump.

Until now mainly fiber lasers with a high power output have been developed [2], which utilize continuous wave pumping. Therefore we want to develop a pulse pumped operating laser with a bulk media for high energy output in the multi-Joule range. Advantageous for thulium media is the about ten times longer fluorescence lifetime in comparison with ytterbium doped media.

In a first step we build a cryogenic cooled stable oscillator of approximately 3.5 m cavity length. The 30 W pump light is absorbed with a 4 pass pump setup in an 8 at.% doped Tm:YAG (thulium doped yttrium-aluminum-garnet)
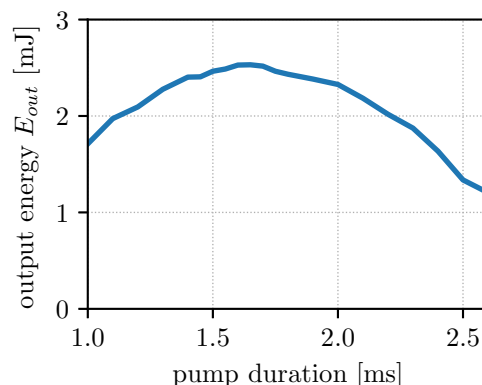
Figure 2: Output energy depending on the pump duration of the q-switched Tm:YAG oscillator. The achieved output pulse duration were in the range of 665 ns - 1224 ns.

crystal. The cryogenic cooling is beneficial because of the increasing emission cross section and quantum efficiency at low temperatures. We already measured the temperature dependent cross sections and re-absorption free fluorescence lifetimes for this material in the temperature range of 80 K to 300 K [3]. The setup of the laser is illustrated in figure 1. With this setup we achieved a maximum output energy of 2.5 mJ in Q-switch operation. The laser pulse length was in the range of 665 ns - 1224 ns for different pump durations. In Figure 2 the exact dependency of the output energy E_{out} on the pump duration is plotted. The drop in the output energy for increasing pump lengths is due to heating effects in the material. Further scaling should be improved by enlarging the beam size and using a lower doped material. In the next step a laser amplifier will be built to produce Joule class laser pulses.

References

[1] L. D. DeLoach, R. H. Page, G. D. Wilke, S. A. Payne, W. F. Krupke, Transition metal-doped zinc chalcogenides: spectroscopy and laser demonstration of a new class of gain media, IEEE Journal of Quantum Electronics 32 (6) (1996) 885–895.

[2] C. Gaida, M. Gebhardt, J. Limpert et al. "Ultrafast thulium fiber laser system emitting more than 1 kW of average power," Opt. Lett. 43, 5853-5856 (2018)

[3] J. Körner, T. Lühder, J. Reiter, M. C. Kaluza et al., "Spectroscopic investigations of thulium doped YAG and YAP crystals between 77 K and 300 K for short-wavelength infrared lasers", Journal of Luminescence 202, 427 - 437 (2018)

Fluence profiles in femtosecond laser sparks and superfilaments in air*

Z. Samsonova[1,2, #], D. Kartashov[1], C. Spielmann[1, 2], S. Bodrov[3], A. Murzanev[3], V. Jukna[4, 5], M. Petrarca[6], A. Couairon[5], and P. Polynkin[7]

[1]IOQ, Abbe Center of Photonics, Friedrich-Schiller-University Jena, Germany; [2]Helmholtz Institute Jena, Germany; [3]Institute of Applied Physics, RAS, Nizhny Novgorod, Russia; [4]Laser Research Center, Vilnius University, Lithuania; [5]Centre de Physique Théorique, Ecole Polytechnique, CNRS, Palaiseau, France; [6]La Sapienza University, Rome, Italy; [7]College of Optical Sciences, The University of Arizona, Tucson, USA.

The formation of long plasma channels (filaments) by high-power ultra-short laser pulses has a number of potential applications, in particular, in remote atmospheric sensing [1]. This has triggered extensive studies of possible scenarios of propagation of an intense laser pulse in air. The observed behavior is a result of the competition between different focusing and defocusing mechanisms which limit (or clamp) the laser peak intensity in the filament. However, a direct measurement of the clamped intensity is quite challenging. We investigate the nonlinear propagation of the multi-TW femtosecond laser pulses in air under different focusing conditions applying the ablation-based method [2].

Recently, a novel method to profile the intense laser beams has been suggested. It is based on the angular-dependent single-shot ablation threshold of a target [2]. With a gold mirror, a fluence from 1 J/cm^2 to 10 J/cm^2 can be reliably measured.

Our experiments have been carried out at the Ti:Sapphire laser system JETi-40 (IOQ, Jena), delivering 40 fs-long pulses at 800 nm. The energy in a single pulse was 100-120 mJ. The technique we used is described in detail in [3]. To profile the beam at a certain position of its propagation, single-shot ablation patterns on a 100 nm-thick silicon wafer were evaluated.

To study the influence of the external focusing on the clamped intensity, we have performed two series of experiments. In the first case, we used a very tight focusing (a lens with f = 90 cm). The beam then was focused as a whole, and no distinct individual filaments were observed (Fig. 1 (a)). This interaction regime is similar to the nanosecond optical breakdown. For the loosened focusing the parameters are in the range for formation of a superfilament [4]. However, the multiple filaments were formed in front of the focal plane of the lens (f = 7.5 m) and traveled through the focal region without coalescing together into one or several superfilaments (Fig. 1(b)). Numerical simulations [5] have been performed to reproduce the beam intensity patterns and for the loosened focusing we found a good agreement with the experimental results.

We have profiled the laser beam in the vicinity of the nonlinear focus. In the case of tight focusing, the peak intensity of the beam exceeded 200 TW/cm^2. For the
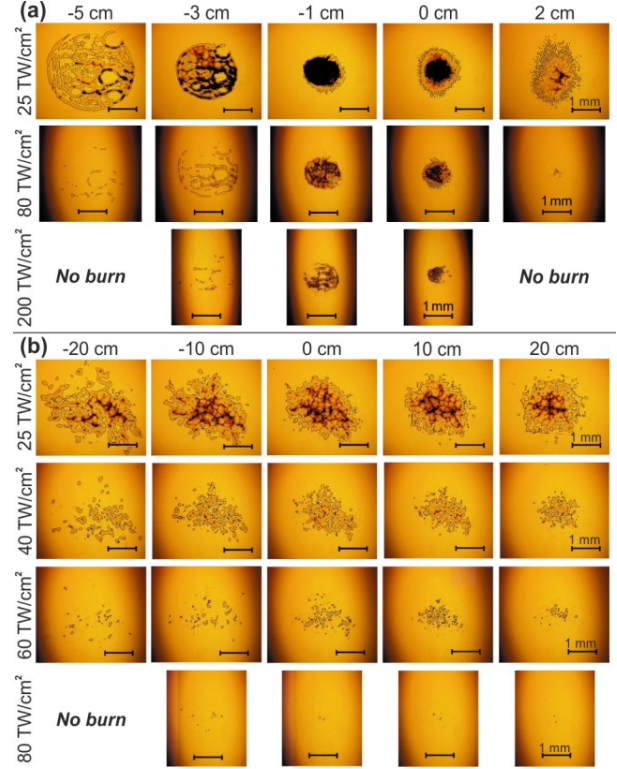
Figure 1: Experimental beam profiles along the propagation path with tight (a) and loosened (b) external beam focusing.

weaker focusing, we observed a formation of individual filaments with an intensity level above 60 TW/cm^2.

References

[1] J. Kasparian and J.-P. Wolf, "Physics and applications of atmospheric nonlinear optics and filamentation", Opt. Express 16, 466 (2008).

[2] Z. Samsonova *et al.*, "Measurements of fluence profiles in femtosecond laser sparks and superfilaments in air", Phys. Rev. A 97, 063841 (2018).

[3] X.-L. Liu *et al.*, "Universal threshold for femtosecond laser ablation with oblique illumination", Appl. Phys. Lett. 109, 161604 (2016).

[4] G. Point *et al.*, "Superfilamentation in air", Phys.Rev. Lett. 112, 223902 (2014).

[5] A. Couairon *et al.*, "Practitioner's guide to laser pulse propagation models and simulation", Eur. Phys. J. Special Topics 199, 5 (2011).

Terahertz generation using two-colour plasma filaments

S. Marathapalli[1], P. Wustelt[1,2], S. Skruszewicz[1,2], G. G. Paulus[1,2], S. Popruzhenkov[3] and A. Gopal[1,2]

[1]Institut für Optik und Quantenelektronik, Friedrich- Schiller Universität, Jena. ; [2]Helmholtz Institut Jena; [3.]National Research Nuclear University MEPhI, 115409, Moscow, Russia

We investigate the generation of broadband terahertz radiation by mixing two-colour femtosecond laser pulses in air. In order to enhance the terahertz energy a new scheme based on circularly polarised mid-infrared pulses has been implemented. Towards this end, a two-colour interferometer setup has been developed.

High-power, broadband terahertz pulses are versatile tools for spectroscopy, imaging and nonlinear studies. Nonlinear wave mixing in gases is a well-established technique to generate broadband THz pulses [1]. Recent works proposed new schemes to increase the THz pulse energy by employing circularly polarised mid infrared pulses [2,3].
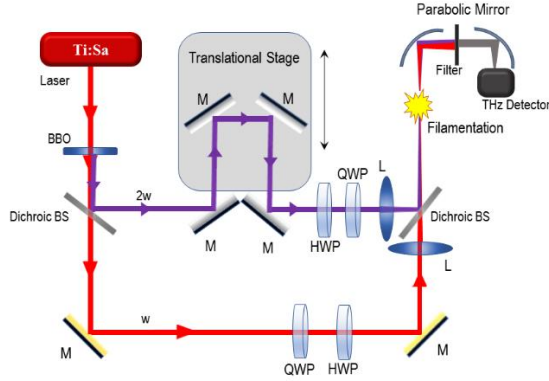
Figure 1: *Experimental setup for THz generation in air*

The experimental setup shown in Figure 1 includes a high accuracy two-colour interferometer for generating temporally delayed laser pulses with frequency ω and 2ω and a terahertz detection system consisting of a calibrated pyrometer. The output from the 1 kHz Ti-Saph laser is fed into the interferometer by high quality reflective optics, where a 200 mm thick BBO crystal is employed to generate the second harmonic (2ω) at 400 nm. Broadband dichroic mirrors are employed to separate the two wavelengths and later recombine them to focus in air to generate plasma via tunnel ionisation. A high precision translational stage with nanometre precision is employed to adjust the temporal overlap between the fundamental and second harmonic pulses. In both arms of the interferometer a half wave and a quarter wave plate are introduced for the polarisation control.

In a single colour field, the photoelectron distribution possesses inversion symmetry while bicolour fields result in the asymmetric distribution of the electrons causing a nonzero time varying photoelectron current which generates terahertz radiation [2,3]. The generated terahertz radiation is collected and relayed onto the pyroelectric detector using two off-axis parabolas. Si wafer was used to filter out laser radiation from the THz.
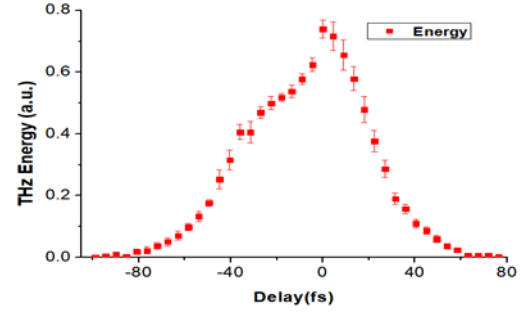
Figure 2: *THz emission as a function of the temporal delay between the* w *and* 2 w *pulses.*

Initially, we investigated THz pulse generation of the fundamental (ω) with energy 2.4 mJ and 30 fs duration and the second harmonic (2ω) with energy 120 μJ and 55 fs duration at the focus. A maximum THz pulse energy of 0.7 μJ is measured. It is observed that when the laser energy drops below $E_\omega = 600$ μJ and $E_{2\omega} = 5$ μJ, no THz emission is detected. THz emission is scanned for circularly polarised fields with same helicity (CP-CP) in temporal steps of 5 fs (see Figure 2). It is observed that THz emission lasts for more than 80 fs.
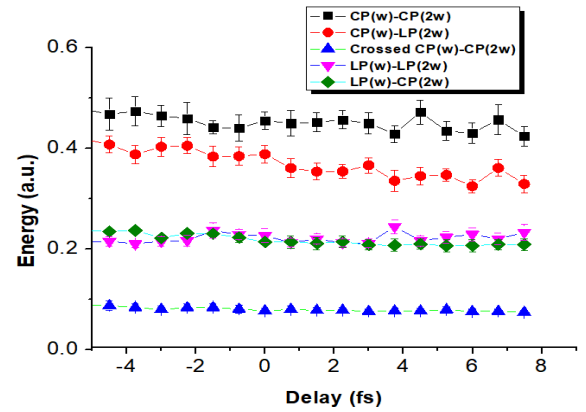
Figure 3: *Terahertz yield for different laser polarisations for different temporal delay between* ω *and* 2ω *pulses.*

The effect of input polarisation on the terahertz generation is shown in Figure 3. It is observed that CP-CP configuration yields the highest THz energy.

References

[1] K. Y. Kim et al. 2008 Nature Photonics. 2 605
[2] Chao Meng et al. 2016 Appl. Phys. Lett. 109, 131105
[3] V. A. Tulsky et al. 2011 Phys. Rev. A 98, 053415

Laser Particle Acceleration

Preplasma study during Ultra-Intense Laser Plasma Interaction Experiments at PHELIX using Optical Diagnostics

J. Hornung[1,2,3], V. Bagnoud[1,2], M. M. Günther[1,2], M. Shi[1], Y. Zobus[4] and M. Zepf[1,3,5]

[1]HI-Jena, Jena, Germany; [2]GSI, Darmstadt, Germany; [3]Friedrich-Schiller-Universität Jena, Jena, Germany; [4]TU-Darmstadt, Darmstadt, Germany; [5]School of Mathematics and Physics, Queens University Belfast, UK

Nowadays research on laser-driven proton acceleration is focusing on the interaction of relativistic-intensity laser pulses with sub-micrometer targets. However, the results obtained experimentally at various laser facilities around the world are not up to the predictions of numerical simulations. Unlike experimental conditions, the simulation expects an initially unperturbated target before the laser plasma interaction. Due to an imperfect temporal contrast, the intensity of the laser is slowly rising, leading to a pre-expansion of the target prior to the arrival of the main pulse. Since this interaction is happening at the ps-time-scale, and on small spatial dimensions, it is difficult to measure the condition of the target. Knowing these conditions, however, is crucial for a direct comparison of the experimental work and the numerical models.

This motivated an experiment at the PHELIX facility to study the preplasma expansion with the help of several optical, time-resolved and time-integrated diagnostics. During the experiment we reached intensities of 10^{19} - 10^{20} W/cm² focused on CH_2 targets with a target thickness ranging from 30 nm to 1 μm. The preplasma conditions were varied by switching from the regular temporal contrast ($\sim 10^{-8}$ @ 100 ps) to an ultra-high contrast (estimated $\sim 10^{-12}$ @ 100 ps) using a double plasma mirror setup, while reducing the laser intensity on target by a factor of two.

This setup, including the beamlines of the optical diagnostics, observing the difference in the laser plasma interactions, can be seen in figure 1.
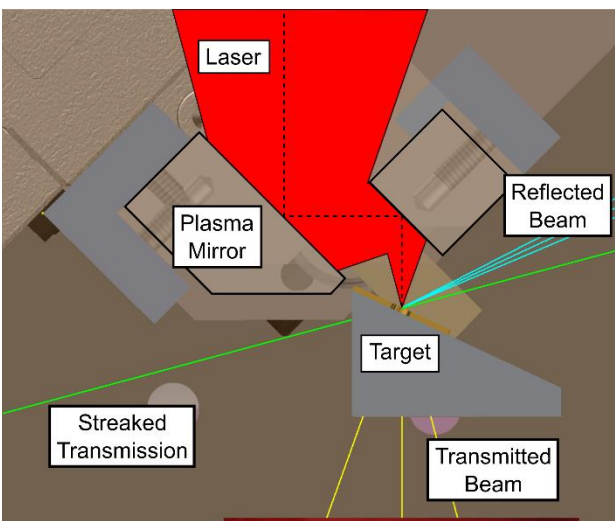
Figure 1: Experimental setup for the ultra-high contrast, using a double plasma mirror. The colored lines show the different preplasma diagnostic beamlines.

The main diagnostics are based on the measurement of the back-reflected and transmitted laser spectrum using integrating spectrometer and a specially designed time resolved diagnostic using the principle of frequency resolved optical gating [1]. These measure the changes of the laser spectrum occurring during the interaction with the plasma. To distinct between different interaction conditions, showing the effect of the improved temporal contrast, the transmitted energy of the pulse was additionally measured.

Another type of diagnostic used, is the time resolved transmission measurement of two off-harmonic probe pulses with a duration of a few nanoseconds and a wavelength of 532 nm and 354 nm respectively. A streak camera measured the transmission through the target on the sub ns-scale.

All of the diagnostics were able observe the strong change in the laser plasma interaction when improving the temporal contrast. The energy measurement showed a fully opaque interaction down to a target thickness of 80 nm, compared to ~900nm without the high contrast, indicating a strong reduction of the pre-expansion of the target.

This was also indicated by the analysis of the spectrum of the back-reflected light, leading to a strong blue shift of the spectrum compared to a stronger red shift with the low contrast option. This effect occurs due to the stronger density gradient of the preplasma, leading to a strong electron pressure, counteracting the laser pressure. This confirms the expected behaviour predicted by particle-in-cell simulations, which were done prior to the experiment. Despite an ongoing analysis of the data, this already indicates a dependency between the preplasma condition and the modulation of the laser spectrum after the interaction.

Additionally we were able to successfully show a proof of principle for the temporal resolved transmission measurement, using an off-harmonic probe beam. It shows the onset of the opacity for the different harmonics and therefore the behavior of different plasma density regions. Using the duration of opacity, one can estimate the plasma expansion of the target.

The diagnostics show promising results, making them suitable for further investigations of the preplasma conditions in upcoming relativistic laser plasma interaction experiments.

References

[1] F. Wagner, J. Hornung, et. al., Rev. Sci. Instr., 88, 023503 (2017)

Transmission light diagnostic for the investigation of relativistic laser plasmas – Preliminary results from experiments at PHELIX

M. Shi[1,3], M. M. Günther [1,2#], V. Bagnaud [2,1], J. Hornung [2,3], M.Zepf [1,3]

[1]Helmholtz-Institut, Jena, Germany; [2]GSI, Darmstadt, Germany; [3]Friedrich-Schiller-Universität, Jena, Germany

With the continuous improvement of laser energy, especially relativistic laser pulses, laser-driven ion acceleration [1] and solid high-order harmonic generation [2] attract more and more attention. These experiments are closely related to laser contrast and pre-plasma density, where the investigation of the plasma density is of great interest. For this purpose, we designed a plasma diagnostic based on transmitted light measurements to scan the laser induced plasma evolution. The plasma diagnostic on which is reported was first used in an experiment at PHELIX to scan the plasma evolution after the laser was interacted with sub-μm targets. Preliminary results show that the diagnostic is promising for the investigation and the control of pre-plasmas.

The experiment was performed using the PHELIX laser system at GSI in Darmstadt. This laser delivers 500 fs pulses at a wavelength of 1053 nm with energies up to 100J. A double plasma mirror immediately before the target was used to increase the contrast. The plasma diagnostics is based on transmitted light energy measurements, as shown in Fig.1. We used a Nd:YAG pulsed laser system (pulse duration: 5 ns) with the 2nd and 3rd harmonic generation (532 nm and 355 nm) as two probe beams. The probe beams are defocused on the target and the transmitted light behind the target was collected. A streak camera is used to record the transmitted light as a function of time.
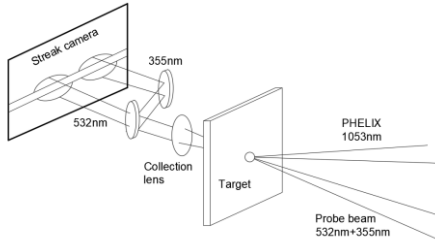
Figure 1: Diagnostic system configuration. 532 nm and 355 nm beams incident target at the same time. A lens collects transmission beam from back side. Streak camera is used to record plasma evolution against time.

The double plasma mirror is used to keep the thin target as its almost solid condition until the main laser pulse arriving, which means the details of plasma evolution can be clearly seen, as shown in Fig.2. In the time scale on Fig.2, the main pulse interacts with the target after 1 ns due to the high-dense plasma created by the pulse, the probe beams were blocked within the further 0.5 ns and 0.3 ns for the 532 nm and the 355 nm beam, respectively. Furthermore, a triangle like shape appeared, which indicates for a gaussian beam. There is an inhomogeneous energy distribution in the area of the laser focus. The most energy was concentrated in the center of the focus. The higher the energy, the faster decreased the plasma density after the main pulse

interaction. The result is that the probe beams passed the plasma for a shorter time. After this triangle like shape, the probe beams shifted a little bit, explained by refraction and plasma moving.
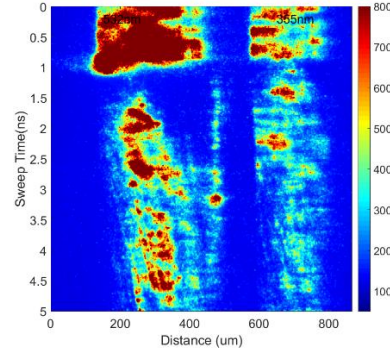
Figure 2: Sweep time is 5 ns. Target, 200 nm thick. The left: 532 nm probe beam. Right: 355 nm probe beam. Main pulse on target at 1ns in the shown time scale.

In order to acquire a more detailed information of the plasma evolution, the sweep time was changed to 2 ns, as shown in Fig.3. Here we have seen a clearly opaque region and a triangle like shape. In other words, the presented plasma diagnostic confirms that the double plasma mirror can increase the laser contrast.
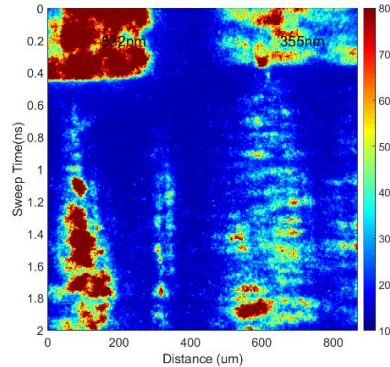
Figure 3: Sweep time was changed to 2 ns. Other parameters are the same as above. Main pulse on target at 0.4 ns in the shown time scale.

The presented preliminary results indicate the capability of the diagnostic to investigate the evolution of laser produced pre-plasmas. In future experiments we will use the improved diagnostic to control the pre-plasma.

References

[2] S. Kahaly, et al. Phys. Rev. Lett., 175001 (2013)
[1] Higginson A, et al. Nature Communications, 2018, 9(1):724.

---

m.guenther@gsi.de

Preplasma Characterisation for Laser-Driven Proton Acceleration

M. Mäusezahl[1, #], S. Keppler[1,2], I. Tamer[1,2], M. Hornung[1,2], M. Hellwing[1], F. Schorcht[2],
and M. C. Kaluza[1,2]

[1]Institute of Optics and Quantum Electronics, Jena, Germany; [2]Helmholtz-Institute Jena, Germany

Recent endeavours in the field of laser-driven ion acceleration from solid targets highlight the importance of the driving laser's temporal intensity contrast. The contrast fundamentally determines the density and geometric shape of the preplasma at which the main laser is absorbed and converted into hot electrons. In the so-called 'Target Normal Sheath Acceleration'-regime (TNSA), these electrons travel through the target and generate a sheath field on the rear side in which protons from contamination layers can be efficiently accelerated [1]. In order to achieve a high conversion efficiency of the laser energy into kinetic energy of the accelerated protons, the absorption of the laser pulse, and thus the preplasma itself, must be precisely tailored. This requires a complete understanding of the generation and spatial expansion of the preplasma. In this context, the plasma excitation with spatio-temporally shaped pre-pulses [2] or the use of specially developed target surfaces [3] are a key technology for optimizing laser-driven proton acceleration.

Current research in this field is carried out at the POLARIS laser system, which is operated at the Helmholtz-Institute Jena. The POLARIS system operates at a wavelength of 1030nm and currently provides up to 17J on target with a pulse duration of 120fs [4]. To investigate the plasma generation especially at this wavelength and pulse duration regime, we have developed an independent pump-probe setup, which allows to precisely characterize the generation and the temporal evolution of the preplasma. The setup is shown schematically in Figure 1 and allows the excitation of a preplasma with a pulse energy of up to 100µJ. With a f/2.5 focusing and a pulse duration of 140fs, intensities of up to 3.5×10^{15}W/cm² can currently be achieved for the plasma excitation. Prepulses with these parameters have been used in various POLARIS experiments in recent years to optimize the laser absorption.
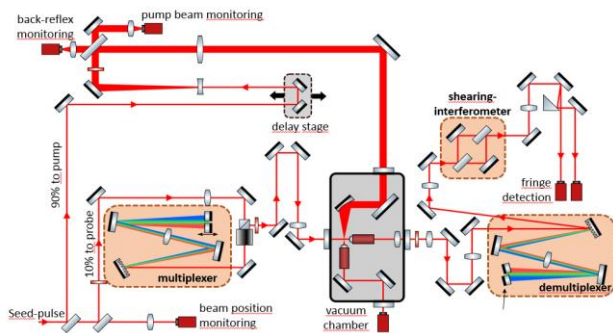
Figure 1: Schematic layout of the developed pump probe setup in the laboratory with the delay stage (top region), the vacuum chamber (center region), the interferometer (upper right region) and a spectral multiplexing and de-multiplexing unit to enable time-resolved measurements.

[#]Max.Maeusezahl@uni-jena.de
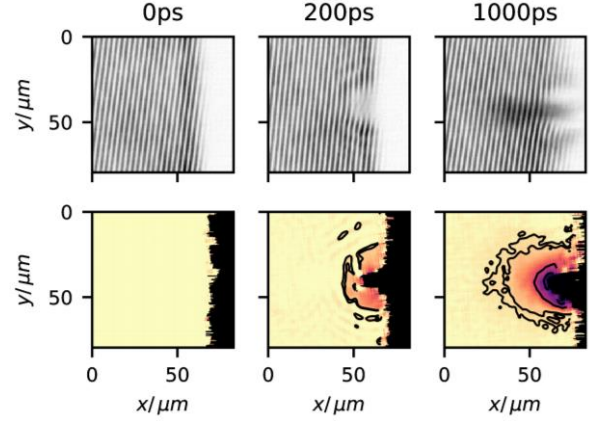
Figure 2: Fringe measurements of the interferometer (top) and the analysed spatial phase of the probe pulse (bottom) at time delays of 0ps, 200ps and 1000ps.

The measuring setup divides an incoming seed pulse into a pump pulse (90%) and a probe pulse (10%) and contains a delay-stage for delays of up to 2ns between both. Furthermore, the setup includes a vacuum chamber for vacuum conditions comparable to that at the POLARIS experiments, as well as an imaging system with 2.5µm resolution and a shearing interferometer for the analysis of the probe-pulse's spatial phase. The setup works by focusing the pump pulse on the front of an aluminium wheel working as a target. The generated plasma is imprinted on the probe pulse's spatial phase at the time when the pulse passes transversally along the target. By analysing the spatial phase and a deconvolution by means of an Abel transformation, the electron density at the time of the probe pulse can be calculated. Figure 2 clearly shows the formation of the plasma and its expansion. At the time t=0ps, i.e. the simultaneous arrival of the probe and the pump pulse, no preplasma is visible. After 200ps and 1ns, however, the spatial expansion is clearly visible.

By means of this measurement setup we were able to perform extensive measurements with two different angles of incidence (0° and 20°), three different polarizations (vertical, parallel and circular) for four different laser energies (and thus intensities). This extensive study allows us to theoretically model the preplasma generation and expansion, as well as benchmark existing numerical plasma simulations, such as MULTI-FS [5], for the experimental conditions of the POLARIS laser system.

References

[1] A. Macchi et al. Rev. Mod. Phys. **85**, 751 (2013).
[2] D. Batani et al. New J. Phys. **12**, 045018 (2010)
[3] D. Khaghani et al. Sci. Rep. **7**,11366 (2017).
[4] M. Hornung et al. Opt. Lett. **41**, 5413 (2016).
[5] R. Ramis et al. Comp. Phys. Comm. **183**, 637 (2012).

Contrast Dependence of Laser-Driven Proton Acceleration

S. Keppler[1,2, #], G. A. Becker[1], N. Elkina[2], I. Tamer[1,2], M. Mäusezahl[1], C. Rödel[1,2], M. Zepf[1,2], M. Hornung[1,2], M. Hellwing[1], F. Schorcht[2], and M. C. Kaluza[1,2]

[1]Institute of Optics and Quantum Electronics, Jena, Germany; [2]Helmholtz-Institute Jena, Germany

Laser-driven proton acceleration to high kinetic energies has a great potential for application in e.g. time-resolved radiography of plasma phenomena or in high-dose radiobiology [1] and translational research in radiation oncology [2], which motivates a continuous improvement of the acceleration process with regard to the maximum energy (E_{Prot}) as well as spatial and spectral properties of the proton beam. During intensive research in recent years, various acceleration regimes have been identified, such as 'Target Normal Sheath Acceleration' (TNSA), 'Radiation Pressure Acceleration' (RPA), and collisionless shock acceleration or different mechanisms in the near-critical density or transparency regime [3]. To date, however, there is a strong discrepancy between theoretical predictions of the maximum E_{Prot} and the experimental results. Furthermore, a tremendous progress in laser development did not lead to a dramatic improvement of the maximum E_{Prot}, which suggests principally limiting physical processes that need to be investigated in detail.

For this reason, we carried out an extensive experimental study during the last year in which we investigated the scaling of the maximum E_{Prot} with the laser intensity (I_L), which was varied by the laser energy (E_L). The study was carried out by varying different parameters, mainly the laser polarization and the temporal intensity contrast. We focused the pulses of the POLARIS laser system, having a duration of 120fs, with an effective f-number of 2.5 under an angle of incidence of 20° onto a 6.5μm thick aluminium foil. The on-target laser energy was varied by more than one order of magnitude between 0.3J and 17J, resulting in intensities between 5×10^{18} W/cm² and 3×10^{20} W/cm².

In order to realize different contrast settings, we have further improved the intrinsic contrast of the Polaris laser pulses by using a plasma mirror, which was equipped with substrates having residual reflectivities of R ≤ 0.1%, R = 4% and R = 30% (see Fig. 1). To extend the contrast range further, we added an artificial prepulse with a relative intensity contrast of 1.5×10^{-5} that reached the target 200ps or 1ns before the main pulse.
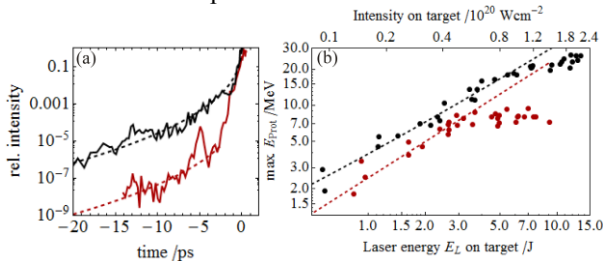
Two exemplary measurements of the E_{Prot}-scaling with the laser energy are shown in Figure 1b), which show clearly that it strongly depends on the different preplasma conditions. To further illustrate this, the preplasma formation was numerically described using the simulation software MULTI-FS [4], taking into account the measured intensity contrast and the semi-spherical expansion of the excited plasma. In Figure 2, the exponent n of the E_{Prot}-scaling ($E_{Prot} \sim E_L^n$) is plotted vs. the resulting scale length L of the corresponding contrast setting. The figure shows a clear increase of the exponent with reduced scale lengths from a root-like up to a linear E_{Prot}-scaling which occurs for $L \leq 2$μm. The square-root-scaling here is likely caused by the ponderomotive laser absorption, which at shorter scale lengths is most likely supported by laterally recirculating hot electrons, which oscillate back and forth through the target, eventually leading to a higher electron density on the rear side and thus to a faster E_{Prot}-scaling.

Furthermore, Figure 1 clearly shows that there is a limitation of the E_{Prot}-scaling depending on the preplasma conditions. In the case of high contrast and thus short scale lengths L (see Fig. 1, red curves), this limitation is already reached at about 9MeV. From here on an increase of the laser energy E_L does not lead to a further increase of the maximum proton energy E_{Prot}. With the intrinsic POLARIS contrast (w/o plasma mirror, see Fig. 1 black curves) the limit is reached at approx. 25MeV, so that the scaling continues here clearly to higher laser energies. Possible reasons are the compression of the preplasma by hole-boring, which strongly influences its electron density and spatial shape during the interaction with the main pulse. This influence is currently investigated using extensive PIC simulations. The systematic study provides an ideal basis for the tailoring of the preplasma and thus an optimization of the maximum E_{Prot}-scaling for future applications.
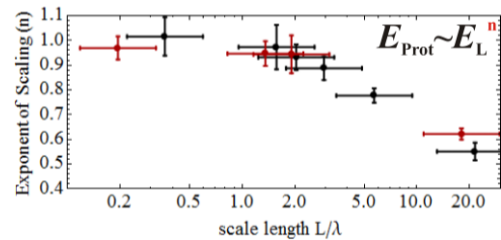
Figure 2: Exponent n of energy scaling $E_{Prot} \sim E_L^n$ of maximum proton energy versus scale length L of preplasma for p- (black) and s-polarization (red).

Figure 1: (a) Temporal intensity contrast of the POLARIS laser without (black) and with plasma mirror and R≤0.1% substrate (red); (b) Double-logarithmic Plot of the corresponding scaling of the maximum proton energy $E_{Prot.}$

#Sebastian.Keppler@uni-jena.de

References

[1] K. Zeil et al. Appl. Phys. B **110**, 437 (2013).
[2] U. Masood et al. Phys. Med. Biol. **62**, 5531 (2017).
[3] A. Macchi et al., Rev. Mod. Phys. **85**, 751 (2013).
[4] R. Ramis et al. Comp. Phys. Comm. **183**, 637 (2012).

Influence of the irradiation geometry on laser-driven proton acceleration with water microdroplets[*]

G. A. Becker[1], M. B. Schwab[1], R.Lötzsch[1], S. Tietze[2], D. Klöpfel[2], M. Rehwald[3], H-P. Schlenvoigt[3], U. Schramm[3,4], A. Sävert[2], and M. C. Kaluza[1,2]

[1]Institut für Optik und Quantenelektronik, Friedrich-Schiller-Universität Jena, Germany; [2]Helmholtz-Institut Jena, Germany; [3]Helmholtz-Zentrum Dresden-Rossendorf, Germany; [4]Technische Universität Dresden, Germany

In most experiments in the field of laser-driven proton acceleration a laser pulse is focussed to intensities $> 10^{18}\,\mathrm{W/cm^2}$ on a micrometer thin foil. The rising edge of the pulse generates a plasma at the front of the foil from which the laser pulse peak accelerates electrons through the foil. Between the electron sheath which is formed on the foil's backside and the positively charged foil an electric field on the order of $\mathrm{MV}/\mu\mathrm{m}$ builds up. It ionizes atoms or molecules from the foil's back side and accelerates them to kinetic energies on the order of $\mathrm{MeV/nucleon}$. However, the lateral extension of such foils allows electrons from the sheath to escape along the foil's surface, which leads to a reduction of the hot electron density and ultimately to a decrease of the electric field responsible for proton acceleration. An approach to avoiding this is to use spherical targets isolated from their environment, such as water droplets [1]. Here, we present results from a laser-driven proton acceleration experiment performed at the JETI 40 laser system using water microdroplets with a diameter of $20\,\mu\mathrm{m}$ as targets. We investigated the influence of the position of the droplets with a steep plasma density gradient along the laser's polarization axis on the maximum kinetic energy of protons emitted in the laser forward direction (figure 1). This steep density gradient was achieved by increasing the temporal intensity contrast of the laser pulses via frequency doubling. The focussed laser pulses had an averaged intensity of $5 \cdot 10^{19}\,\mathrm{W/cm^2}$. A significant minimum of the maximum proton energy is visible when the droplets were centrally illuminated ($x = \pm 1.25\,\mu\mathrm{m}$) because the laser cannot penetrate the steep plasma density gradient and accelerate electrons efficiently, thereby reducing the electric field responsible for proton acceleration. When the droplets were moved in the lateral direction so that the laser hit them on their sides the maximum proton energy increased significantly. Here, a part of the laser's electric field points into the droplets, enabling the laser to directly heat electrons and accelerate them in forward direction. However, a second effect is also responsible for the enhancement of the electric field, which we were able to study with the two-dimensional Particle-in-Cell code EPOCH. When the hot electron current flows outside the droplet's surface, it induces a cold return current at the droplet surface. These currents generate a magnetic field (figure 2 (b)) which pushes electrons in the outward direction [2]. However, the charge separation field (figure 2 (a)) pulls the electrons towards the droplet. In summary, when the laser illuminates a droplet under grazing incidence, a hot electron current is generated which flows around the droplet and induces electromagnetic fields that in turn confine the current near the surface. This confinement, on the other hand, strengthens the charge separation field and improves the proton acceleration.
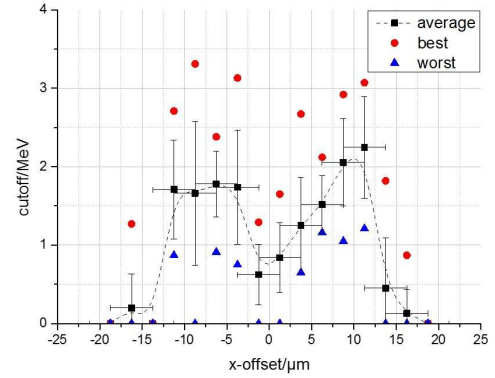
Figure 1: The maximum proton energy as a function of the position of the droplets relative to the laser focus along the laser's polarization axis.
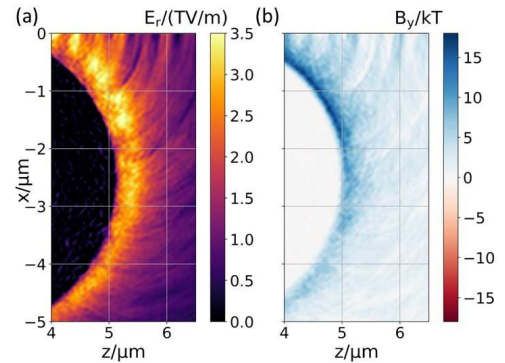
Figure 2: The simulated (a) radial electric and (b) magnetic field in y-direction $29\,\mathrm{fs}$ after the pulse peak has hit a droplet with $5\,\mu\mathrm{m}$ diameter.

References

[1] e.g. Ter-Avetisyan et al., PRL 96, 145006 (2006)

[2] Li et al., PRL 96, 165003 (2006)

Toward high repetition production of thin cryogenic liquid hydrogen targets[*]

M. M. Günther[† 1,2], *D. Klöpfel*[1], *C. V. Stelzig*[1,2], *S. Supp*[1,3], *M. Zepf*[1], *and W. Ziegler*[1]

[1]HI Jena, Jena, Germany; [2]GSI, Darmstadt, Germany; [3]FSU Jena, Jena, Germany

Cryogenic hydrogen targets are interesting in many research fields such as in fundamental nuclear structure physics where exotic, instable nuclei are investigated using protons as probe. Furthermore, in high intense relativistic laser-plasma research, cryogenic hydrogen targets become more and more of interest. Especially in laser driven ion acceleration thin mass limited targets combined with short pulsed, intense and high contrast laser are used to investigate acceleration mechanisms different to the well known target normal sheath acceleration (TNSA) concept. Therefore, freestanding and thin liquid or solid hydrogen targets with high repetition production are of great interest to produce a proton beam via the radiation pressure mechanisms. In addition, cryogenic liquified gasous targets are more suitable in laser experiments compared to standard solid foil targets because there is no debris generation during the laser matter interaction which saves the used optics close to the laser-matter interaction region. There are different methods discused for the generation of thin solidified hydrogen targets, such as: Sputtering onto a cold surface [1]. Thin films can be produced, but there is no freestanding target. High pressure extrusion of solidified gas through a nozzle [2]. Here, no submicron thick targets can be produced. Dropplet targets are possible [3], but the targets are not in the submicron thickness range and there are inhomogeneities in geometry. The method of the condensation onto a cooled frame is discused [4]. But here the repetition rate in the production of the target is low and therefore suitable in single laser shot applications, only. All of these methods are not suitable for the high repetition production of hydrogen freestanding film targets with a few hundrets of nanometer thickness.

We report on a novel method to generate cryogenic hydrogen film targets with variable reptition rates. The main principle of the method is to span a thin foil of liquified hydrogen gas, generated by its surface tension onto a frame. We have performed experiments for wetting tests with different liquids (water, acetone, ethanol, isopropanol, and cryogenic liquid nitrogen) at athmospheric conditions to studie the wetting behavior using different frames with different geometries and several materials. Based on the results from this experiments we performed further studies for the development of a suitable technology and construction of a target generator for the high repetition production of cryogenic thin hydrogen foils within a vacuum chamber. As coolant to liquifie hydrogen we used liquid helium with a cryostate.

The target production with the target generator is based on a frame which is moved through a reservior of liquid hydrogen. At the interaction region, where the target interacts with the laser pulse the hygdrogen foil is locked out to vacuum via a special mechnism. The figure 1 shows the vacuum chamber for our test set-up. First wetting test were successful performed. The next steps are tests, where the target is locked out into the vacuum. Furthermore, we investigate and develop different diagnostics for the target characterization concerning thickness and homogeneity. For our test experiments we used a special set-up with a whitelight interferometry in transmission scheme.

The whole cryogenic hydrogen target project including the optical target characterization is a novel and complex technological development. Therefore, in this report we don't give any more details until a first peer-reviewed research paper concerning the target production technique and characterization is published by us. First laser experiments are planed beginning 2020.
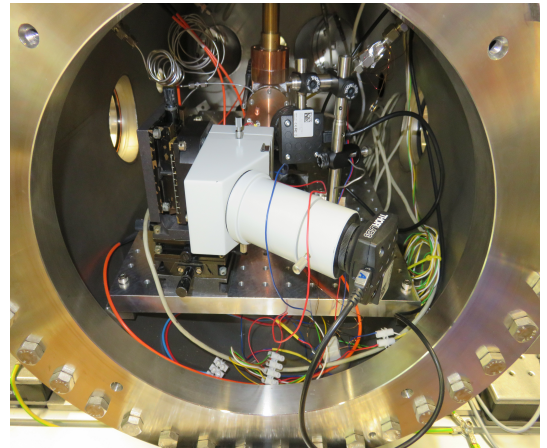
Figure 1: A look inside the test vacuum chamber with diagnostics and target production chamber. No any more details are presented in this report because a peer-reviewed research publication will be published first.

References

[1] Morrison, J. T. et al., Phys. Plasmas, vol. 19, 030707 (2012).

[2] Margone, D. et al., Phys. Rev. X, vol. 6, 041030 (2016).

[3] Gauthier, M. et al., Rev. Sci. Instrum., vol. 87, 11D827 (2016).

[4] Tebartz, A. et al., Rev. Sci. Instrum., vol. 88, 093512 (2017).

Electron bunch profile encoding through a temporal-to-spatial conversion in an orthogonal configuration

M. Almassarani[*1,2], *A. Woldegeorgis*[1,2], *and A. Gopal*[1,2]

[1]Institut für Optik und Quantenelektronik, Physikalisch-Astronomische Fakultät, Friedrich-Schiller-Universität, Max-Wien Platz 1, D-07743 Jena, Germany; [2]Helmholtz Institute Jena, Fröbelstieg 3, 07743 Jena,Germany

Abstract

We report on an accurate measurement of the longitudinal charge distribution of relativistic electron bunches generated from an intense-laser-matter interaction. Electrons in the relativistic regime produce a radially extended Coulomb field orthogonal to the propagation direction. When the electron bunch traverses over an electro-optic crystal, the associated coulomb field induces birefringence in the crystal. Hence the electron bunch length can be measured experimentally by encoding its coulomb field profile on the spatial intensity distribution of an optical femtosecond probe pulse in an orthogonal geometry.

Experiment and results
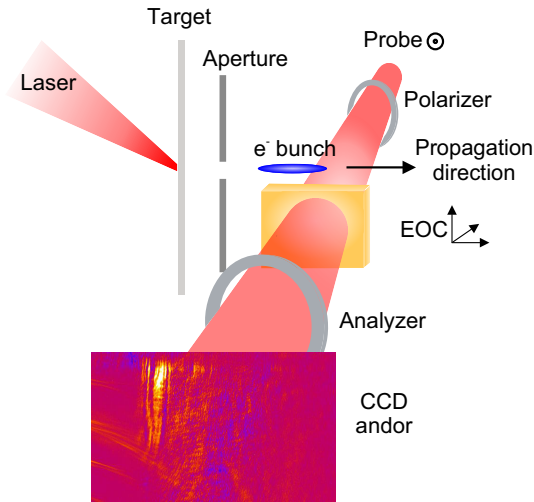
Figure 1: Schematics of the experimental setup to measure the electron bunch duration.

The experimental setup is depicted in Fig.1 where pulses from JETI-laser with Energy = 1 J, λ_c = 800 nm and τ_L = 30 fs are tightly focused onto 5μ m thin metal targets (Al, Ti) reaching intensities $> 10^{19} W/cm^2$. A $1mm$ thick Aluminum plate with a $1mm$ hole aligned to the target normal direction is placed behind the target. Electrons pass through the hole along target normal direction over the upper edge of a $200\mu m$ thick ZnTe EO-crystal. The bunch's Coulomb field creates time dependent changes of the birefringence and the cross-propagating optical probe

pulse experience a phase shift. A $100fs$ optical probe at normal incidence is used with a pair of crossed polarizers so the induced optical phase shift is converted to an intensity modulation which is recorded by the CCD[1]. The re-
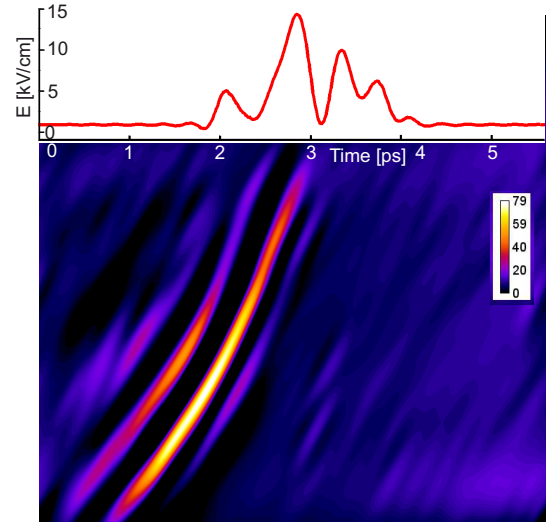
Figure 2: top, the temporal waveform of the electric field of the electron bunch retrieved from the EO- signal. Bottom, signatures of the escaping electrons as seen by the CCD.

trieved temporal waveform of the electric field is shown on top in Fig.2. The studied case shown at the bottom is for electron bunches recorded by the ZnTe crystal placed at $11.5mm$ from the target. A Gaussian fit was used to estimate the width (FWHM) and for the strongest signal the duration is around $230fs$. By varying the time delay between the electron bunch and the optical probe pulse, we observe that the bunch width broadens as it propagates away from the interaction point, thus allowing us to estimate the initial bunch width to be around $170fs$.

References

[1] X. Yang, et al. " Electron bunch length monitors using spatially encoded electro-optical technique in an orthogonal configuration". Appl. Phys. Lett. 95, 231106 (2009).

---

* mohammed.almassarani@uni-jena.de

Radiation Reaction of a Relativistic Electron with a High-Intensity Laser Field

F. C. Salgado[*,1,2], *C. Rödel*[1,2], *and M. Zepf*[1,2]

[1]Helmholtz Institute Jena, Germany; [2]Institute of Optics and Quantum Electronics, Friedrich-Schiller-University Jena, Germany

In the low-intensity limit, the equation of motion of a particle in an electromagnetic field is well approximated by the Lorentz equation. In general, however, called radiation reaction effects must be taken into account especially at high intensities. Radiation reaction describes the recoil force that a moving particle is submitted due to the emission of electromagnetic radiation or processes such as pair production. In this work, we compare the solution of different models of radiation reaction using the Astra-Gemini laser system parameters.

One of the most accepted theories to describe the radiation reaction effect in the classical limit is the Landau-Lifshitz (LL) equation of motion [1]. For ultrarelativistic particles and constant crossed fields, the LL equation reduces to the Lorentz force plus the leading term of the LL radiation force, respectively: $\mathrm{d}u^\mu/\mathrm{d}s = (q/m_q)\, F^{\mu\nu} u_\nu + (2/3)(q^4/m_q^3)(F_{\nu\sigma}u^\sigma)(F^{\nu\alpha}u_\alpha)u^\mu$.

Increasing the field strength or the electron energy, quantum effects cannot be neglected anymore. One approach to include them into the LL equation is by multiplying the radiation force by a quantum correction factor $g(\chi_e)$ which only depends on the electron quantum parameter $\chi_e = (q/m_q^3)\sqrt{-(F^{\mu\nu}u_\nu)^2}$ [2]. This model is known as the semiclassical model of radiation reaction.

The third model to evaluate the radiation reaction problem is based on strong-field quantum electrodynamics (SFQED). In this model, the electron dynamics are solved using the Monte-Carlo method proposed by Ref. [3]. Here, the SFQED solution is composed of the average of one thousand numerical Monte-Carlo evaluations.

Numerical evaluations were performed using the Astra-Gemini laser system parameters [4] and a comparison between the three different models was conducted. The evaluations assume a head-on collision between an electron traveling in $\hat{x}$-direction and initial Lorentz factor of 4000 and an external electromagnetic plane wave with a Gaussian envelope linearly polarized in $\hat{y}$-direction with $a_0 = 20$, $\lambda = 800$ nm.

The comparison between the results is presented in Fig. 1. Using these parameters. the single electron loses energy due to radiation emission as it interacts with the external electromagnetic field. The emission in the quantum picture is stochastic, leading to non-deterministic energy loss and an increased electron energy spread shown by the shaded area. The averaged quantum solution, however, tends towards the classical LL model.
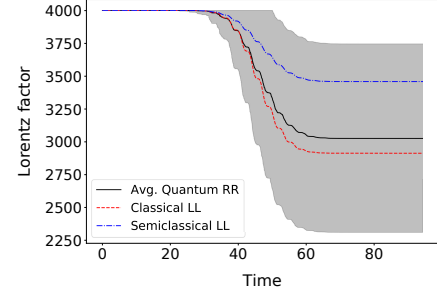
Figure 1: Lorentz factor of the particle during the interaction. Gray area: standard deviation of the averaged quantum radiation reaction solution.

The SFQED Monte-Carlo solution allows estimate the averaged number of photons emitted per electron. As depicted in Fig. 2, it is expected about 5.10 ± 2.25 photons to be emitted per electron in each interaction.
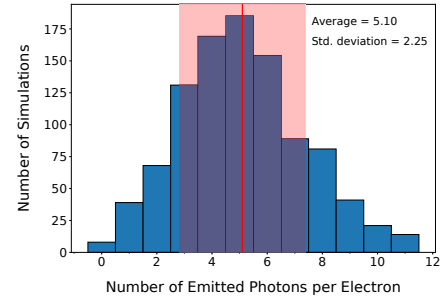
Figure 2: Statistical behavior of the SFQED Monte-Carlo solutions. Expectancy of 5.10 emitted photons per electron.

The significant differences between the models highlight the need for experimental data. Therefore, an experiment to observe the radiation reaction effect was conducted during January and February of 2019 at the Astra-Gemini Laser system and data analysis is currently underway.

References

[1] L. Landau and E. Lifshitz, "Course of Theoretical Physics: The Classical Theory of Fields", Pergamon Press, 1971.

[2] J. G. Kirk *et al.*, Plasma Phys. Control. Fusion, vol. **51**, no. 8, p. 085008, 2009.

[3] N. V. Elkina *et al.*, Phys. Rev. ST Accel. Beams, vol. **14**, no. 5, p. 054401, 2011.

[4] *Central Laser Facility*, https://www.clf.stfc.ac.uk/Pages/The-Astra-Gemini-Facility.aspx. Accessed: 2019-03-15.

[*] felipe.salgado@uni-jena.de

Implementation of a transverse optical probe at FLASHForward at DESY[*]

C. Zepter[1], F. P. G. Stehr[1], A. Sävert[2], M. B. Schwab[1], and M. C. Kaluza[1,2]

[1]Institute of Optics and Quantum Electronics, Jena, Germany; [2]Helmholtz Institute Jena, Germany

We report on the implementation of an all optical transverse probing diagnostic for an on-shot characterisation of FLASHForward (FF▶▶) electron bunches

The Future-ORiented Wakefield Accelerator Research and Developement (FLASHForward, FF▶▶) is a project at the DESY free electron laser facility FLASH aiming to produce GeV electron beams of high quality in a plasma target within a few centimeters. The plasma can be created either by a high voltage discharge mechanism or by a 25 TW Ti:Sapphire laser system. The electron beams extracted from the FLASH2 linear accelerator are the driver for the plasma wakefield accelerator [1].

To be able to advance this particle-driven plasma-based acceleration technology further one needs to gain a deeper understanding of the physics underlying these acceleration processes. Therefore the knowledge of the spatial and temporal profile of the driver bunch for every shot is of great interest. One way of characterising the location, duration and charge of the driver bunch in real-time is by recording its magetic field with a short pulse duration probe beam exploiting the Faraday effect[2].

Faraday effect When propagating in a plasma and crossing a magnetic field oriented parallel to its direction of propagation a probe beam's polarization is rotated by an angle φ_{rot} as shown in the inset of Fig. 1. This angle φ_{rot} is defined as

$$\varphi_{\text{rot}} = \frac{e}{2\,c\,m_e\,n_c} \int_l n_e\,\vec{B}_\varphi\,\mathrm{d}\vec{s}$$

where $\vec{B}_\varphi$ is the azimuthal magnetic field surrounding the electron bunch, c, e, m_e, n_c are the vacuum speed of light, electron charge, electron mass and critical density, respectively, and $\mathrm{d}\vec{s}$ is an infinitesimal path element along the path l of the probe beam through the plasma.

This polarization rotation can be measured by taking a high resolution image of the interaction backlighted by an initially linearly polarized probe pulse using a CCD-camera equipped with a polarizer.

Experimental setup The setup of the experiment is depicted in Fig. 1. As a short probe beam a part of the 25TW laser with a duration of ca. 30 fs is split off and transported to the interaction zone along a separate probe beam line. The probe first passes a polarizer to get a defined polarization of the probe beam. The beam then passes the plasma target, where it interacts with the magnetic fields of the FF▶▶ driver bunch in a discharge-generated plasma, rotating the probe's polarization. After propagating through the interaction the probe is imaged onto two CCD-cameras each equipped with a polarizer with a high resolution imaging system consisting of a microscope objective and a field lens.
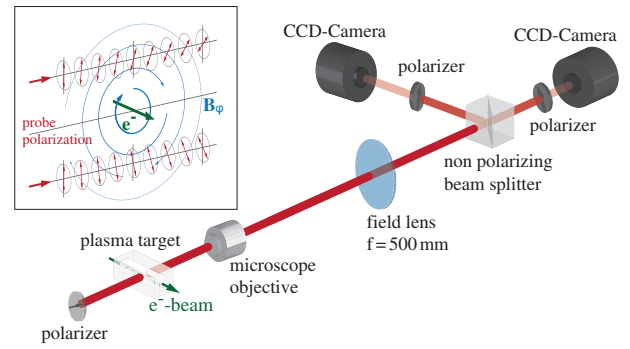
Figure 1: Schematic drawing of the Faraday rotation setup as installed at the FF▶▶ beamline at DESY in Hamburg. Inset: Schematic drawing of the probe's polarization rotation due to the presence of an azimuthal magnetic field.

For a low background measurement of φ_{rot} the polarizers in front of the camera should be rotated away from extinction of the original polarization in opposite directions by an angle Φ_{pol} slightly larger than the expected rotation angle ($\varphi_{\text{rot, exp.}} \approx 0,2\,^\circ$). The intensity $I_{\text{pol},i}$ on the two cameras ($i = 1, 2$) then is proportional to [2]

$$I_{\text{pol},i} \propto I_0 \left[1 - \cos^2(\varphi_{\text{rot}} - \Phi_{\text{pol}}) \right].$$

By a pixel by pixel division of the obtained polarograms, i.e. $\frac{I_{\text{pol},1}}{I_{\text{pol},2}}$ the rotation angle φ_{rot} can be deduced.

Status The Faraday setup was built, tested and characterized in Jena and brought to FF▶▶ in summer 2018.

The modular design of the high resolution imaging system allows different magnification (2,5x, 5x, 7,5x) with a resolution below 3 μm.

References

[1] A. Aschikhin et al., Nucl. Instrum. Methods Phys. Res. A 806 (2016)

[2] A. Buck et al., Nat. Phys. 7 (2011)

Relativistic laser-matter interaction with planar foils at high laser contrast*

Z. Samsonova[1,2, #], O. N. Rosmej[3,4], S. Höfer[1], D. Kartashov[1], C. Arda[3], D. Khaghani[1],
A. Schoenlein[3], S. Zähter[3], A.Hoffmann[1], R. Loetzsch[1,2], A. Saevert[1,2], I. Uschmann[1,2],
M. E. Povarnitsyn[5], N. E. Andreev[5,6], L. P. Pugachev[5,6], M. C.Kaluza[1,2], and C. Spielmann[1,2]

[1]IOQ, Abbe Center of Photonics, Friedrich-Schiller-University Jena, Germany; [2]Helmholtz Institute Jena, Germany; [3]GSI, Darmstadt, Germany; [4]IAP, Goethe University Frankfurt, Germany; [5]Joint Institute for high Temperatures of RAS, Moscow, Russia; [6]Moscow Institute of Physics and Technology, Dolgoprudny, Russia.

A significant improvement of the temporal pulse contrast of high-power laser systems has made a remarkable impact on the field of relativistic laser-matter interaction physics. With a high-contrast laser, the pre-plasma formation is strongly reduced and the pulse peak intensity interacts with a sharp density profile. The electron energy distribution function and the hot electron fraction in this case are expected to be very different in comparison with the low-contrast interaction. The resulting plasma parameters and plasma dynamics are subjects of research crucial for better understanding of particle acceleration via radiation pressure [1] and a new regime of interaction with nanostructures [2].

The experiment has been carried out at the Ti:Sapphire laser system JETi-40 (IOQ, Jena) which has an excellent contrast. To improve the contrast further we frequency doubled (@ 400 nm) the laser pulse before focusing onto a 25 μm-thick Ti foil (this thickness ensures no refluxing effect for electrons with energies up to 100 keV). The resulting laser pulse intensity was ~2×10^{19} W/cm^2 with the picosecond pulse contrast of 10^{-9}. The complex diagnostics provided an opportunity to measure X-ray spectra and infer information about different electron fractions in a wide energy range [3].

The Bremsstrahlung emission from the hot electrons traversing the target was measured with the Timepix detector and the spectrum of the run-away electrons characterized with a magnet spectrometer imply a multi-temperature electron energy distribution function. The 3D Particle-in-Cell (PIC) simulations predict up to 4 effective electron temperatures when the peak intensity reaches the target (t=0 fs) (Fig. 1(a)), which agrees with the experimental results.

The total charge of the run-away electrons is estimated to be only 10 pC, which could result in a heating up to tens of eV. However, keV bulk electron temperature T_e was retrieved from the K-shell emission spectrum using methods of X-ray spectroscopy (Fig. 1(b)). The simulated emission spectra from the highly charged states (Ti^{19+}, Ti^{20+}) obtained with PIC show a good agreement with the experiments for peak values of T_e=1.8 keV and n_e=2×10^{23} cm^{-3}. However, it was measured [3] that this high-temperature and high-density plasma was generated only within a 150 nm-thick top layer of the target, which is supported by the hydrodynamic simulations. Already ~200 fs after the interaction, the deposited energy is dis-
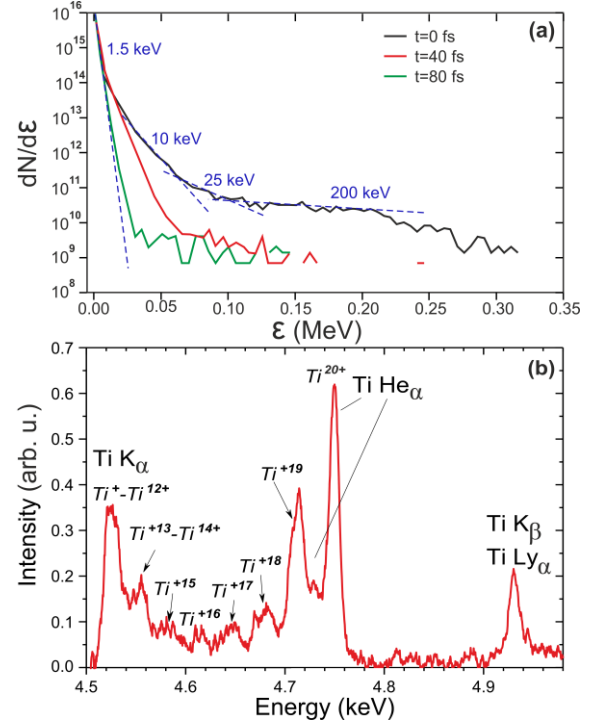
Figure 1: (a) Simulated electron energy spectra at different time steps of the interaction. (b) K-shell emission spectrum from a Ti foil.

tributed by the heat wave over a larger volume where the electron temperature drops below 1 keV.

The generation of keV-hot bulk electrons can be explained by the collisional mechanism of the laser energy absorption in plasmas with a nearly step-like electron density profile. The laser energy is first deposited into the nm-thin skin-layer and then transported deeper via the electron heat transport. This scenario is opposite to the volumetric heating with supra-thermal electrons, which production was strongly suppressed in the high-contrast interaction.

References

[1] M. Kaluza et al., "Influence of the laser prepulse on proton acceleration in thin-foil experiments", Phys. Rev. Lett. 93, 045003 (2004).

[2] Z. Samsonova et al., "X-ray emission generated by laser-produced plasmas from dielectric nanostructured targets", AIP. Conf. Proc. 1811, 180001 (2017).

[3] O. Rosmej et al., "Generation of keV hot near-solid density plasma states at high-contrast laser-matter interaction", Phys. Plasmas 25, 083103 (2018).

Terahertz generation during high-power laser matter interaction:
A different perspective[*]

M. Almassarani[† 1,2]*, A. Woldegeorgis*[1,2]*, S. Herzer*[1]*, S. Marathapalli*[1]*, and A. Gopal*[1,2]

[1]Institut für Optik und Quantenelektronik, Physikalisch-Astronomische Fakultät, Friedrich-Schiller-Universität
Max-Wien Platz 1, D-07743 Jena, Germany; [2]Helmholtz Institute Jena, Fröbelstieg 3, 07743 Jena, Germany

Abstract

We present an insightful study on the spatio-temporal characteristics and the dynamics of terahertz generation process from intense laser-thin foil interaction. This was achieved via recording the 2-D beam profile along with the transient structure of THz pulses.

Results and discussion

The collection geometry of the THz optics is shown in Fig.1 which consists of forward and non collinear emissions. The 2-D beam profile of the terahertz radiation is shown in Fig.2. Our measurements clearly show that the emission is not isotropic with multiple peaks and variable signal amplitudes. This strongly suggest multiple excitation processes of the THz. The emitted THz radiation is mostly dominant near the laser propagation direction at $45\,^\circ$. Several peaks with signal strengths many times higher than the background level clearly indicate the dominant effect of particle dynamics rather than surface currents[1].
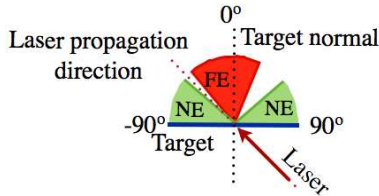
Figure 1: Geometry of the collection angles for the detection of terahertz emission.

To connect the beam profile to the temporal structure of the terahertz pulses we performed time domain measurements using electro-optic (EO) detection scheme[2]. As shown in figure 3, multiple pulses with variable amplitudes are present for both forward (top) and non collinear (bottom) emissions. The integrated signal from the EO detection matches with the corresponding value obtained from the beam profile measurements. The presence of different peaks can be an indication to a highly dynamic emission process that include energetic particles leaving the target rear surface. These correlations will be tested deeply in future experiments.
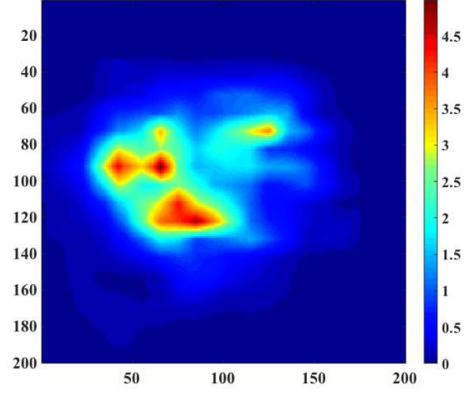
Figure 2: 2D beam profile of the THz radiation emitted from the target rear surface.
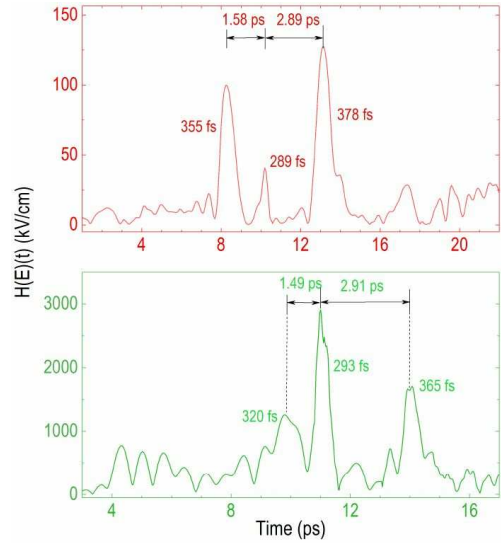
Figure 3: Temporal structure of the terahertz radiation obtained from the electro-optic (EO) measurements for FE and NE emissions.

References

[1] Poyé, A. et al. "Physics of giant electromagnetic pulse generation in short-pulse laser experiments". Phys.Rev.E 91, 043106 (2015).

[2] Woldegeorgis, A. et al. "Multi-MV/cm longitudinally polarized terahertz pulses from laser-thin foil interaction". Optica 38, 1474 (2018).

[†] mohammed.almassarani@uni-jena.de

Surface High Harmonic Generation with using a f/12 OAP

J. Braenzel [1], R. McHugh[1], M. Shi[1], P. Hilz[1], S. Cousens[2], M. Yeung[2], A. Sävert[1], G. Schäfer[1], M. Zepf[1]

[1]Helmholtz Institute Jena, Jena Germany; [2]Queens University Belfast UK

We report about our recent experimental investigation on Surface High Harmonic Generation (SHHG) at the JETI200 laser system by using a f/12 focal length. Next to a wider focal area, a long focal length promises a lower HHG divergence – making SHHG radiation more application-oriented for future experiments.

Emitted from relativistic oscillating electrons at the plasma boundary, SHHG generation via the Relativistic Mirror Model (ROM) highly depends on the scale length of the plasma density gradient (L_p). It has been shown [1, 2] that ROM harmonics are efficiently generated for $L_p > \lambda_L/10$ and vanish for too long ones, e.g. $L_p \sim 5\lambda_L$ [3]. The ROM harmonic divergence follows the divergence of the driving laser [4]:

$$\theta_N \sim \frac{\theta_L C}{N}$$

where C is a constant and N the harmonic order. Usually SHHG are created using short f numbers, e.g. f/2, in consequence the SHHG beam is highly divergent and needs to be refocused closely to its emission point. This results in highly complex setups, especially if one thinks about using the harmonics to drive other processes. This constraint motivated our experimental campaign in which we investigated SHHG using a f/12 length. The recently updated JETI200 laser system provided the following parameters: beamline transmission 60%, single plasma mirror transmission 70%, <2.5 J on target, 20-30 fs pulse duration. With a 12µm FWHM focal diameter and 40% energy content in FWHM we reached an avg a0 = 3.5 and intensity of about 4×10^{19} W/cm^2. As target served fused silica. The XUV spectrometer used consisted of a 200 nm Al filter, a Shimadzu SVLS grating 1200 l/mm and an Andor XUV cam. The spectrometer provided a 1:1 imaging, preserving one spatial dimension. We detected the XUV signal in reflection direction (42° geometry). The strongest signal we observed, when the laser was defocused of about +2400 µm, which is < 5x the laser's Rayleigh length. Moreover, we found an optimized range when we enlarged the laser pulse duration, by changing the group velocity dispersion (GVD) of about + 900 fs^2. Fig.2 shows significant higher cutoff frequencies for

longer GVD values. This introduces a positive chirp on the laser pulse. Our experiments did not found a similar effect at a negatively chirped pulse. We observed on our 2ω scatter diagnostic (84 cm from target), that defocusing of the
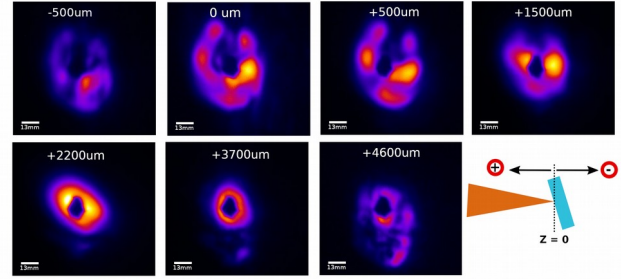
Figure 1: 2ω beam profile at different foci positions

la
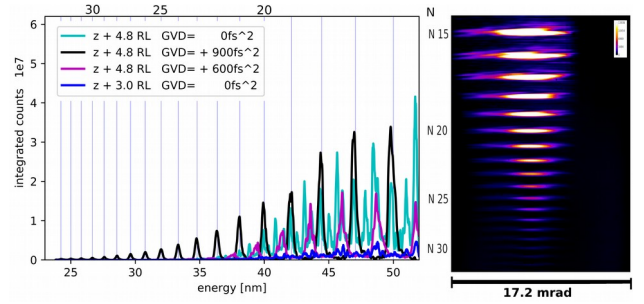
Figure 2: SHHG signal at different GVD values and corresponding optimum detector image

laser on the target in the range of +/-4 mm, strongly manipulated the divergence of the emitted 2ω and SHHG beam (cf. Fig.1). According to Eq. 1, with C = 1, the diffraction limited divergence of our SHHG beam at N25 calculates to 3.2 mrad. The raw sprectrum in Fig.2, recorded at optimal parameters in defocusing and GVD, exhibits for N25 a divergence of 3.1 mrad.

The experimental data and its interpretation is still under investigation.

References

[1] C. Rödel et al., PRL 109, (2012) , p. 125002

[2] I. J. Kim et al., Nat. Comm., 2245, (2012)

[3] C. Thaury and F. Quere, J. Phys. B: At. Mol. Opt. Phys. 43, 213001 , (2010)

[4] B. Dromey et al., Nat. Phys., 1158, (2009)

Photon and Particle Spectroscopy

Experimental Preparations at CRYRING@ESR[*][†]

M. Lestinsky[‡][1], F. Herfurth[1], S. Schippers[2], Th. Stöhlker[1,3,4], and the APPA collaborations[1]

[1]GSI, Darmstadt, Germany; [2]JLU Gießen, Gießen, Germany; [3]HI Jena, Germany; [4]IOQ, FSU Jena, Germany

CRYRING@ESR is a low-energy heavy ion storage ring facility and the first new ion beam installation within the FAIR project [1-3]. The former Swedish CRYRING was modernized and adapted to its new location and integrated into the existing ion beam topology behind ESR. Presently, the ring is undergoing commissioning with ions from a small local source but its full potential will become available once it receives ions transfered from ESR in all ion species and charge states that the GSI accelerator complex is capable to produce, from protons to bare uranium.

Already now, with the local injector, first tests of the facility have been performed and general operation of the ring was established. Foremost, ion beam storage has been achieved, and ion beam lifetimes were defined largely by the prevailing vacuum conditions. Since CRYRING@ESR is a synchrotron, the energy ramping of stored beams from the lowest energy limit to the maximum allowed by the bending power of the magnets was demonstrated and Figure 1 shows a Schottky spectrum of circulating H_2^+ ions in CRYRING, ramped from injection energy to the maximum. Further, first attempts on recommissioning the electron cooling facility have already shown signs of electron cooling. Alongside, a new FAIR-type control system has been installed as a prototype for the remaining and coming installations and important experience has been gained by its operation in a running facility. Almost all of the beam diagnostics instrumentation is ready for basic operation. Establishing the particle transfer from ESR is foreseen for late 2019.

With the machine gradually progressing into regular operation, many experimental systems are presently also being prepared for their deployment to experiment beamtimes, and CRYRING@ESR in fact offers exciting opportunities for research on slow, highly charged ions for a large range of scientific fields. The low energy conditions will allow for precision spectroscopy and thus, e.g., to test QED in a non-perturbative strong field regime, or to study transient quasi-molecular systems. Further, at the border between atomic and nuclear physics, nuclear size effects, hyperfine interactions or exotic couplings between the electronic shell and the nucleus of an ion may be explored. In nuclear physics, storage of bare nuclei at low energies permits to determine fragment distributions unmasked by atomic physics. Under these conditions, e.g., nuclear re-
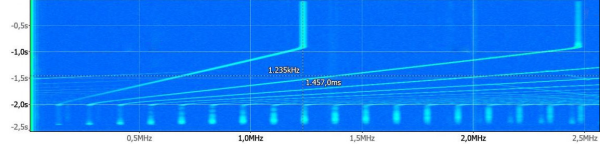
Figure 1: Schottky noise spectrum of H_2^+ ions circulating in CRYRING, injected at 300 keV/u and accelerated to 24 MeV/u. The fundamental revolution frequency is seen leftmost with several adjacent higher harmonics.

actions at the Coulomb barrier or nucleosynthesis of heavy elements in the Gamow window of the p-process may be analyzed. While the Physics book lays out a long-term program for future experiments at CRYRING@ESR [4], three first experiment proposals described therein were approved by the GSI program advisory committee (GPAC) which has reviewed them with highest rating. Their preparations are of highest importance for the coming beamtime campaigns and cover photoionization of stored ions, dielectronic recombination, and $1s$ Lambshift measurements in bare, highly charged ions. In cooperation between GSI, JLU Giessen, KIP Heidelberg, and HI Jena the necessary setups are being prepared: for particle detectors [5], for laser systems, for controlling the electron-ion collision spectroscopy at the electron cooler, and for the data acquisition setups.

Moreover, for an open call for letters of intent so far 17 such letters were submitted by various experiment collaborations, which sketch out the general ideas for planned future measurements. These are a valuable guide for directing further machine development to the needs of future science.

References

[1] http://www.gsi.de/cryring/

[2] M. Lestinsky, et al., "CRYRING@ESR: A study group report", 2012, GSI Tech. Design Rep.

[3] F. Herfurth, et al., "Commissioning of the low energy storage ring facility CRYRING@ESSR" 2017, in proc. COOL'17, THM13.

[4] M. Lestinsky, et al., "Physics book: CRYRING@ESR", 2016, Eur. Phys. J. Spec. Top. 225, p. 797

[5] E. Menz, et al., "Commissioning of a Single Particle Detector for Recombination Experiments at CRYRING@ESR", this volume.

Commissioning of a Single Particle Detector for Recombination Experiments at CRYRING@ESR*

E. B. Menz[1,2,3], C. Hahn[1,2,3], P. Pfäfflein[1,2,3], M. Lestinsky[1], F. M. Kröger[2,3], U. Spillmann[1], A. Kalinin[1,4], J. Glorius[1], and Th. Stöhlker[1,2,3]

[1]GSI, Darmstadt, Germany; [2]Helmholtz Institute Jena, Germany; [3]Friedrich-Schiller-Universität, Jena, Germany; [4]Goethe-Universtität, Frankfurt am Main, Germany

A detector based on the scintillator material YAP:Ce and capable of counting single ions has been installed and tested at the CRYRING@ESR storage ring at GSI.

Detector Design

The commissioning of the CRYRING@ESR heavy ion storage and the research opportunities thus made accessible have made the availability of robust and reliable ion detectors a fundamental requirement [1]. These detectors will need to provide single-hit detection efficiency at MHz count rates of ions with energies ranging from sub-MeV/u to 15 MeV/u, while withstanding the radiation damage imparted by the energetic ions. Given these restrictions, a detector system based on the YAP:Ce crystal scintillator provides an attractive approach, utilizing a material that is endowed with a significant degree of radiation hardness while remaining comparatively affordable [2].
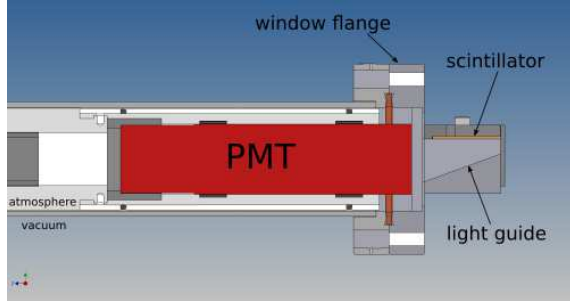
Figure 1: Schematic design of the setup: half-section with detector head (consisting of the scintillator crystal and a light guide) at vacuum and PMT at atmospheric pressure.

The realized design features a detector head which is exposed to the ring vacuum and consists of the scintillator crystal and a light guide. A photomultiplier tube (PMT) is pressed against the atmospheric side of the window flange on which the detector head is mounted. Incoming ions impinging on the scintillator crystal produce light that is transported around a 90° bend by the light guide and reaches the PMT through the window flange where the scintillation flash is converted to an electronic signal. This setup facilitates both the efficient detection without the need for a window in front of the scintillator and the removal of the PMT before baking of the vacuum components.
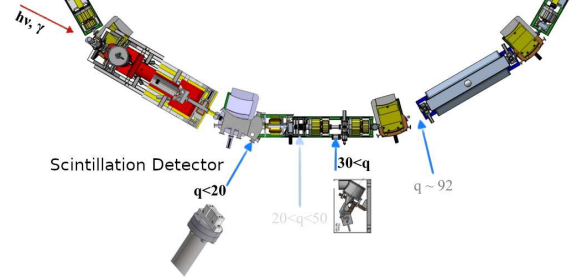
Figure 2: Schematic location of the detector positions downstream from the electron cooler.

The detector system is intended for the observation of electron-ion recombination products in the electron cooler section of CRYRING@ESR. The scintillator can be moved into the path of the respective product beam for the given initial-to-final charge-state ratio and register charge-exchanged ions with an efficiency of nearly 100% in single-particle counting mode. The current positioning of the detector directly behind the magnetic dipole downstream from the electron cooler (see Fig. 2) allows for the detection of reaction products from parent ions in low charge states (q < 20).

Tests and Commissioning

The setup has been tested with H_2^+ and D^+ beams from the local source during two commissioning beamtimes at CRYRING in 2018. Even at these low energies a satisfactory detection efficiency was achieved. A basic data acquisition system was set up and the count rate over the beam process duration observed. The data shows the initial injection flash and a further count rate peak that is due to narrowing of the beam when electron cooling is applied leading to a higher beam intensity on the scintillator crystal. Towards the end of the 30 s process the beam is gradually lost. Due to the high dark count rate of ∼2 kHz observation of this part of the beam process was not easily possible [3]. The source of the high dark count has since been identified as light pollution from a hot-cathode vacuum gauge.

References

[1] M. Lestinsky, Y.Litvinov and T. Stöhlker, *Eur. Phys. J. Special Topics* **225** (2016) 5.

[2] P. Pfäfflein, *master thesis*, (2017).

[3] E. B. Menz, *master thesis*, (2018).

Development of a SiPM-based ion detector for CRYRING@ESR

G. Weber[1], A. Borovik Jr.[2], V. Hilbert[1,3], H. Lin[4], P. Pfäfflein[1,5], B. Zhu[1,5], C. Hahn[1,5], M. Lestinsky[4], S. Schippers[2], J. Rothhardt[1,3], and Th. Stöhlker[1,4,5]

[1]HI Jena, Germany; [2]Institute of Physics, Justus Liebig University Gießen, Germany; [3]Institute of Applied Physics, Friedrich Schiller University Jena, Germany; [4]GSI, Darmstadt, Germany; [5]Institute for Optics and Quantum Electronics, Friedrich Schiller University Jena, Germany

Combining novel laser-driven high-flux XUV sources with storage rings will open new possibilities for precision spectroscopy as well as pump-probe measurements of highly-charged ions. In an upcoming proof-of-principle experiment at the recently commissioned CRYRING@ESR stored C^+ ions will be excited and subsequently photoionized by XUV laser pulses. Both the photon beam and the stored ion beam will be merged in the experimental section YR09 of the CRYRING. The product ions will be separated from the primary ions by a dipole magnet located downstream to the interaction zone. The trajectory of the product C^{2+} ions, according to ion-tracking simulations, enables their detection exclusively inside the dipole-magnet chamber. This requires the detector to be positioned and operated in a strong magnetic field, which takes well-established detectors based on secondary-electron emission (see, e.g., [1]) out of consideration. Thus, a novel detector system has been developed that is based on a YAP:Ce (yttrium aluminium perovskite, YAlO3:Ce) scintillator connected to an array of silicon photomultipliers (SiPM). While YAP:Ce is well-known as a radiation-hard and UHV-compatible scintillator material [2,3,4,5], the readout by SiPM provides the advantage that this type of photodetector is not sensitive to strong magnetic fields.

pulses which will be registered by a 3 x 3 SiPM, array with an active area of 6.07 x 6.07 mm^2 each, placed on a custom-made interface board in a pocket tube outside of the vacuum. Due to the orientation of the available ports in the magnet dipole chamber, the photomultiplier cannot be mounted directly behind the scintillator. The produced photons must therefore be guided by a specially-shaped quartz crystal. To avoid unnecessary irradiation during the ion-beam preparation procedure, the entire construction can be swiftly retracted from the product-ion trajectory area and "hidden" behind a dedicated shielding. The whole construction can be fine-positioned along the pocket axis to account for possible displacements of the product-ion trajectory.
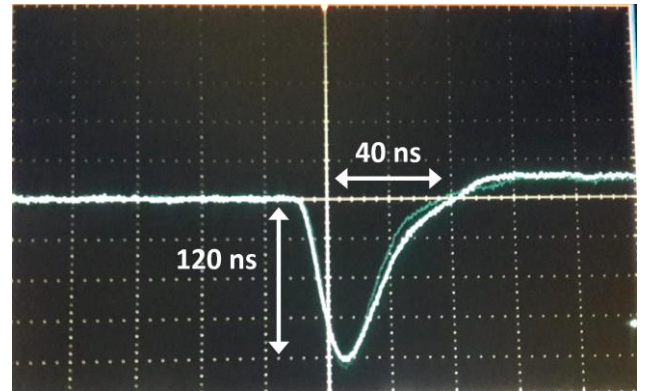
Figure 2: Test of the detector system with a Na-21 source in front of the scintillator crystal.

In Fig. 2 we present a first test of the detector system using a Na-21 source in front of the scintillator crystal. As a next step we will perform a detailed study of the detector performance using C^{2+} and other ion species in the few MeV energy range at the JULIA accelerator of Friedrich Schiller University Jena.

Figure 1: A cut view of the CAD model of the present detector setup. The solid (green) line represents the simulated C^{2+} trajectory.

The CAD model of the detector setup is shown in Fig. 1. Product ions will hit the scintillator plate producing light

References

[1] K. Spruck et al., *Rev. Sci. Instrum.* **86**, 023303 (2015)
[2] G. Miersch et al., *NIM A* 369, 277 (1996)
[3] W. Klamra et al., *NIM A* 444, 626 (2000)
[4] S. Westman et al., *NIM A* 481, 655 (2002)
[5] W. Q. Wen et al., *NIM B* **317**, 731 (2013)

Deceleration and storage of highly charged ions at the HILITE Penning trap experiment

N. Stallkamp[1,2,3], S. Ringleb[3], B. Arndt[6], M. Kiffer[3], S. Kumar[4], G. Paulus[2,3], W. Quint[1,5], Th. Stöhlker[1,2,3] and M. Vogel[1]

[1]GSI, Darmstadt, Germany; [2]Helmholtz-Institut Jena; [3]Friedrich Schiller Universität Jena; [4]Inter-University Accelerator Centre, New Delhi, [5]Ruprecht Karls-Universität Heidelberg, [6]Goethe Universität Frankfurt

We have conceived, designed and built the HILITE Penning trap experiment which aims at the study of matter in the presence of extreme laser fields, both in the high-energy and in the high-intensity regime. It employs ion-cloud formation techniques as well as destructive and non-destructive detection techniques to analyse the trap content [1]. A key element of this is the study of ionisation starting from any specific charge state.

Since the setup is meant to be operated at different laser facilities, it includes a dedicated source of highly charged ions that keeps it easily transportable. For that purpose, a compact electron-beam ion source (EBIT) is used.
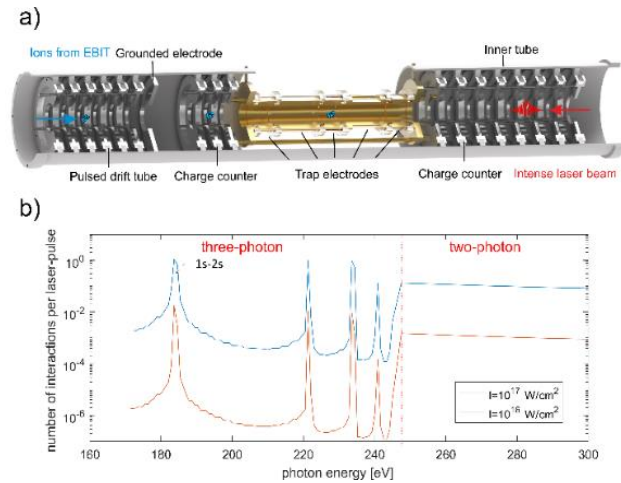
We are operating this source in a pulsed mode to create ion bunches and have optimized the parameters to maximize the number of extracted ions. A velocity filter is used to select the ion species of interest (for example Ar^{13+}) and an Einzel lens focuses the beam towards the trap. Inside the magnet bore (see the schematic in picture 1a) a stack of electrodes works as a deceleration stage in a pulsed drift tube mode. By fast switching of the applied voltage, a deceleration of the ions from about 1 keV/q extraction energy to 200 eV/q is achieved, which has been verified by a single-pass non-destructive charge counter placed on either side of the trap. This detection technique is based on the pick-up and amplification of induced image charges in the electrode and can be used to determine the ion number, energy and bunch structure. A schematic of the principle and results are shown in figure 2. A calibration with a destructive detector was performed, indicating a current lower detection limit of 800 Ar^{13+} ions.

This is a low-energy, single-pass detection similar to the one performed at the SpecTrap experiment [3].

After deceleration, a capture sequence (subsequent switching of trap electrodes) is applied in order to store the ions. So far, storage times of the order of several tens of minutes have been achieved. This has been verified by ion extraction onto a multichannel plate detector (MCP) outside of the magnet bore.
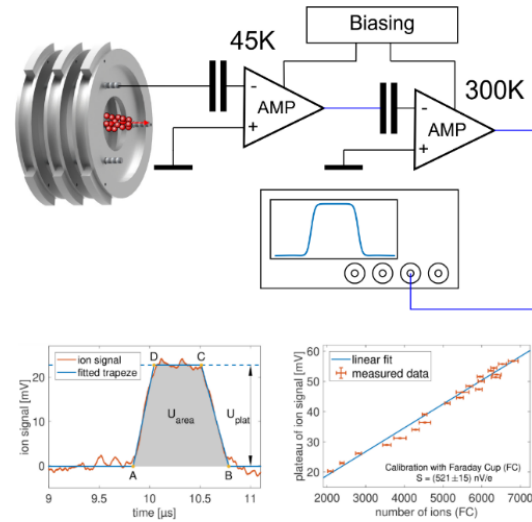
Figure 2: Single-pass non-destructive detection scheme by induced image charges (top). Acquired signal and calibration measurement with a Faraday cup (bottom).

The experiment has been granted beamtime at the FLASH laser facility at DESY in Hamburg to study excitation and ionization processes in the XUV and soft X-ray photon energy regime. Theoretical predictions are provided by our colleagues from Helmholtz Institute Jena, shown in figure 1b [2].

References

[1] S. Ringleb et al. Journal of Physics Conference Series 635 (2015) 092124

[2] J. Hofbrucker, A. Volotka (HI Jena); private communication

[3] S. Schmidt et al. Rev. Sci. Inst. 86, 113302 (2015)

Figure 1: (a) Schematic of the Penning trap setup including deceleration and single-pass non-destructive ion detection devices. (b) Expected ion yield for hydrogen-like carbon in the X-ray photon energy regime based on theoretical predictions [2].

A comparative measurement and characterisation of three Cryogenic Current Comparators (CCCs) based on low-temperature superconductors*

V. Tympel[1,#], Th. Stoehlker[1,6,10], M. Fernandes[2,3], C.P. Welsch[2,3,4], H. De Gersem[5], N. Marsic[5], W. Müller[5], D. Haider[6], F. Kurian[6], M. Schwickert[6], T. Sieber[6], J. Golm[7], R. Neubert[7,11], F. Schmidl[7], P. Seidel[7], M. Schmelz[8], R. Stolz[8], V. Zakosarenko[8,9]

[1]Helmholtz Institute Jena, 07743 Jena, Germany; [2]CERN, 1211, Geneva 23, Switzerland; [3]Cockcroft Institute, Sci-Tech Daresbury, WA4 4AD, Daresbury, Warrington, UK; [4]Department of Physics, The University of Liverpool, Liverpool, L69 7ZE, UK; [5]Department of Electrical Engineering and Information Technology, TU Darmstadt, 64283 Darmstadt, Germany; [6]GSI Helmholtzzentrum für Schwerionenforschung, 64291 Darmstadt, Germany; [7]Institute of Solid State Physics, 07743 Jena, Germany; [8]Leibniz Institute of Photonic Technology, 07745 Jena, Germany; [9]Supracon AG, 07751 Jena, Germany; [10]Institute for Optics and Quantum Electronics, 07743 Jena, Germany; [11]Thuringia Observatory Tautenburg, 07778 Tautenburg, Germany

Abstract

A Cryogenic Current Comparator (CCC) is a non-destructive, metrological-traceable charged particle beam intensity measurement system for the nano-ampere range. Using superconducting shielding and coils, low temperature Superconducting Quantum Interference Devices (SQUIDs) and highly permeable flux-concentrators, the CCC can operate in the frequency range from DC to several kHz or hundreds of kHz depending on the requirement of the application. This work compares the noise measurements of three different Pb- and Nb-based CCC-sensors done 2015 (CERN-Nb-CCC [1]) and 2018 (GSI-Pb-CCC, GSI-Nb-CCC-XD) in the Cryo-Detector Lab at the University of Jena.

Noise Measurements

The graph of the input current noise density in Fig. 1 can be divided in three frequency regions. The 1/f-region below roughly 2 kHz indicates the differences between the amorphous Vitrovac (GSI-Pb-CCC) and the nano-crystalline Nanoperm (GSI-Nb-CCC-XD) core material. Vitrovac shows up to four times higher noise values, but has a lower acoustic sensibility between 5 Hz and 50 Hz and less spontaneous current jumps (noise below 100 mHz). The next region up to 100 kHz or 500 kHz is characterized by an almost constant level of white noise below 5 pA/√Hz. The last region starts with small resonance peaks and a falling low-pass edge. The smaller bandwidth of the GSI-Nb-CCC-XD is a result of the balanced SQUID coupling.

The original CERN-Nb-CCC also shows also typical nano-crystalline core behaviour (see Fig. 2, blue line). For the application in the CERN AD ring a 1 kHz RC-low-pass was added in front of the SQUID to realise integration (see Fig. 2, green dots). Unfortunately the noise is therefore dominated by a thermal resistor noise.
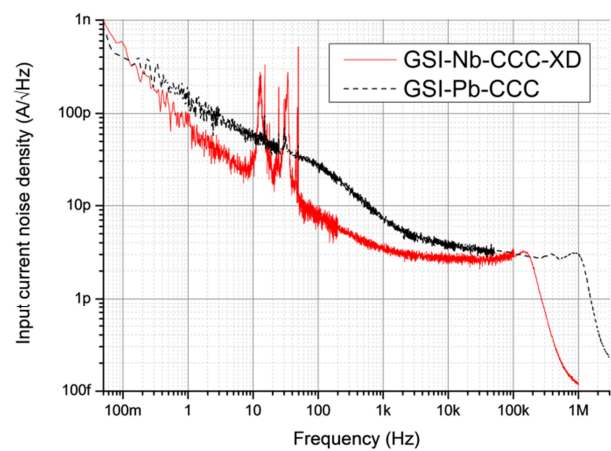
Figure 1: Current noise of the GSI-CCCs @ 4.2 K.
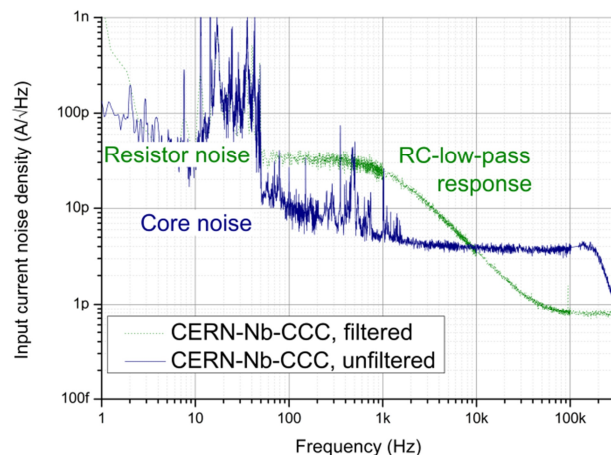
Figure 2: Current noise of the CERN-CCC before (blue line) and after optimization with a RC-low-pass (green dots) of the SQUID coupling.

References

[1] R. Geithner, "Optimierung eines kryogenen Stromkomparators für den Einsatz als Strahlmonitor", Ph.D. thesis, Dept. Phys., F. Schiller University Jena, Jena, Germany, 2013.

High-Precision X-ray Spectroscopy of Fe Ions in an EBIT using a maXs Detector*

M. O. Herdrich[† 1,2,3], *A. Fleischmann*[4], *D. Hengstler*[4], *S. Allgeier*[4], *C. Enss*[4], *S. Trotsenko*[3], *T. Morgenroth*[3], *R. Schuch*[5], *G. Weber*[2,3], *and Th. Stöhlker*[1,2,3]

[1]IOQ, University Jena, Germany; [2]HI-Jena, Germany; [3]GSI, Darmstadt, Germany; [4]KIP, University Heidelberg, Germany; [5]MSI, University Stockholm, Sweden

Introduction Recent developments in the field of cryogenic micro-calorimeter detectors during the past years, in particular the MMC (metallic-magnetic micro-calorimeter) type, are promising for the usage in x-ray spectroscopy experiments. MMCs are typically operated at temperatures below $50 \, \mathrm{mK}$ and use a paramagnetic temperature sensor to convert the rise in temperature upon the absorption of a single x-ray photon into a change of magnetic flux in a SQUID sensor [1]. Within the SPARC collaboration the maXs (micro-calorimeter array for X-ray spectroscopy) detector series is developed by the Heidelberg group of C. Enss in cooperation with Helmholtz Institute Jena and the atomic physics division of GSI. The maXs-30 detector features 64 pixels and has a theoretical energy resolution of $5 \, \mathrm{eV}$ FWHM at $6 \, \mathrm{keV}$ photon energy with an accessible energy range from several $100 \, \mathrm{eV}$ up to a few $100 \, \mathrm{keV}$ [2], thus combining the benefits of high spectral resolution typical for crystal spectrometers with a broad bandwidth acceptance comparable to conventional semiconductor detectors. Due to these outstanding characteristics, micro-calorimeter detectors are expected to play a key role for precision x-ray spectroscopy at GSI and the future FAIR facility. We report on first tests of maXs detectors on the GSI campus.

Preliminary Results After proof-of-principle measurements performed over the recent years at the gas target of the ESR, in July of 2018 a maXs-30 detector array was set up at the S-EBIT-I located on the GSI campus [3]. The EBIT (electron beam ion trap) uses a focused electron beam ($10 \, \mathrm{kV}$ energy, $25 \, \mathrm{mA}$) to excite and ionize Fe ions. The ion cloud is confined by a potential well created by the electron beam, three drift tubes, and a superconducting Helmholtz-coil pair. Due to the continuous interaction between the ion cloud and the electron beam, characteristic x-rays are emitted through excitation and recombination processes. Figure 1 shows a preliminary spectrum consisting of L- to K-shell transitions in multiple charge-states of Fe-ions. Because of temperature fluctuations of the detector during the measurement, the spectral resolution is slightly broadened to $\approx 23 \, \mathrm{eV}$ FWHM.

Conclusion and Outlook The experimental findings proof that calorimeters are indeed promising detectors for x-ray
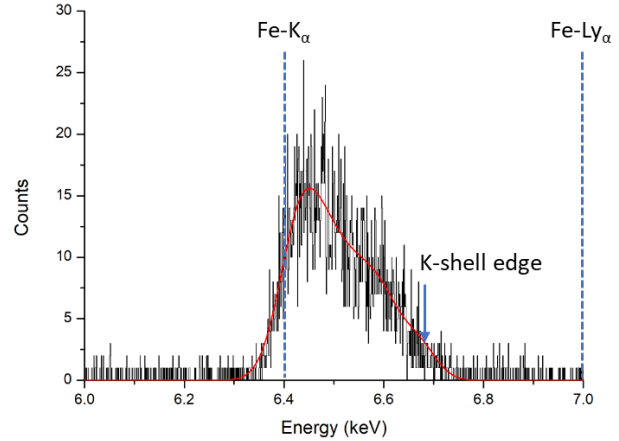
Figure 1: The graph is showing the X-ray spectrum of Fe ions in the S-EBIT-I ($10 \, \mathrm{kV}$ electron beam, $25 \, \mathrm{mA}$) recorded by the maXs-30 micro-calorimeter (black line). Visible are the Lyman (K- to L-shell) transitions of multiple charge states of iron. The blue dashed lines indicate the K_α transition line of neutral iron atoms as well as the Ly_α line of hydrogen-like iron for reference. The highest Lyman transition energy of Fe^{24+} is marked as well to indicate the spectral edge between the fully ionized L-shell and the K-shell. The red curve represents a least-squares fit including the most prominent lines.

spectroscopy applications in realistic experiment scenarios. Several improvements were proposed to increase the reliability and controllability of the maXs detector series. An improved temperature control and correction procedure has been developed for a second experiment campaign at the S-EBIT-I with the maXs-30 or a comparable MMC detector that will be conducted in April 2019. Overall, the experiment serves as a crucial step in the preparation for the 1s-Lamb-shift measurement using an MMC at CRYRING in spring 2020.

References

[1] D Hengstler, M Keller et al., Physica Scripta T166 (2015) DOI:10.1088/0031-8949/2015/T166/014054

[2] S Kempf, A Ferring et al., Superconductor Science and Technology, vol. 28 (2015) DOI:10.1088/0953-2048/28/4/045008

[3] R Schuch, S Tashenov et al., Journal of Instrumentation, vol. 5 (2010) DOI:10.1088/1748-0221/5/12/C12018

S-EBIT Facility: Status Report*

S. Trotsenko[1,2], T. Morgenroth,[1,2,3], M. O. Herdrich[1,2,3], G. Vorobjev[2], D. Racano[2], F. Herfurth[2], R. Schuch[4] and Th. Stöhlker[1,2,3]

[1]Helmholz Institute Jena, Jena, Germany; [2]GSI Helmholtzzentrum für Schwerionenforschung, Darmstadt, Germany; [3]Friedrich-Schiller-Universität Jena, Jena, Germany; [4]University of Stockholm, Stockholm, Sweden.

One of the recent efforts of the Helmholtz Institute Jena program focus on providing the FAIR related instrumentation with highly charged ions, which is of particular importance in the FAIR construction period, were little to no beamtime is available on the GSI/FAIR accelerator complex. Here, two cryogenic electron beam ion traps (S-EBIT-I and S-EBIT-II), that we built up based on the Stockholm EBIT facility [1], become handy and play a crucial role realizing the institutes scientific program.
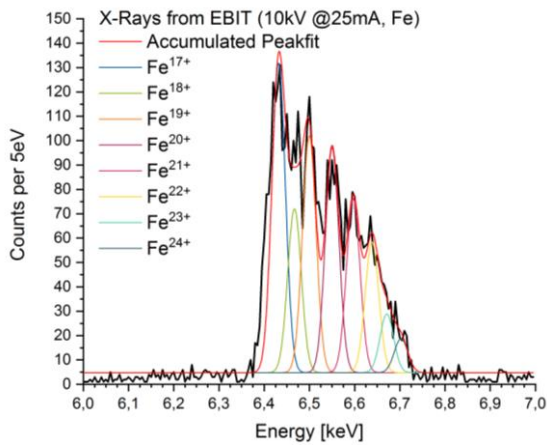
Figure 1: X-ray spectrum from S-EBIT-I recorded using a maXs-30 MMC.

The S-EBIT-II apart from the stand alone operation should serve as an R&D source of highly charged mid- to high-Z ions for the HITRAP experiments. The machine is undergoing its final stage in terms of mechanical construction. The high temperature superconducting leads have been upgraded with a pair of Bi-2223 current leads, encased in G-10 copper and NbTi extension, which allowed to ramp the main superconducting Helmholtz coils up to the 4 Tesla field. The first 10kV commissioning tests are currently being prepared. A new prototype electron gun, based on a IrCe-cathode has been designed and the very first test are being carried out. This type of e-gun is particularly suited for the commissioning phase of the EBIT as the cathode is very robust with respect to the experimental environment, where during the tests multiple ventilation of the EBIT chamber may take place as well as possible poisoning of the original Ba-cathode is highly probable. Relatively limited emission current of the IrCe-based electron gun, on the order of 20mA is still high enough to carry out the first commissioning test and a further upgrade to a larger diameter (up to 2mm) cathode should be possible.

The S-EBIT-I is currently serving as an R&D platform for the FAIR developments, e.g. x-ray crystal optics, magnetic micro-calorimeters (MMC), electronics and data acquisition systems etc. That of particular importance with respect to the first upcoming experiments on the FAIR facility such as CRYRING. The recently developed by the University of Heidelberg MMC are set up at the S-EBIT-I in the X4 experimental cave. In this combination, the electronics, data acquisition system is being built up and tested as well as the data processing algorithms are being benchmarked.
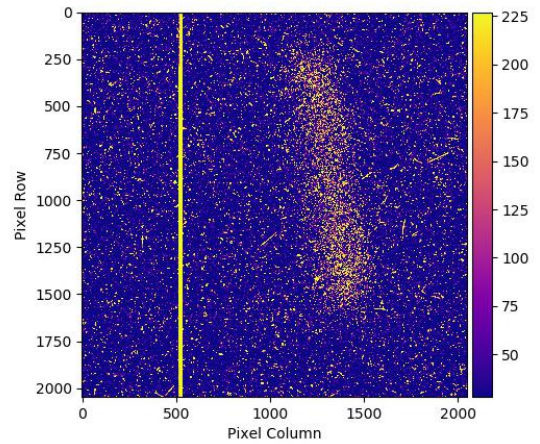
Figure 2: Iron Kα from the EBIT reflected by the x-ray optics onto a CCD detector.

Besides analysis of the x rays produced in the EBIT, these activities serve as the first proof of concept for the application of a maXs-30 micro-calorimeter as a dedicated spectrometer in a typical experimental environment [2]. Figure 1 shows a preliminary analysed x-ray spectrum as taken by the MMC at the S-EBIT-I (10keV, 25mA). The Kα lines of highly charged iron is represented and in order to guide the eyes, different charge states of iron are marked. Figure 2 shows the Kα radiation reflected by the crystal optics (HAPG) onto a position sensitive CCD detector [3]. The spot is a reflection of the ion cloud and its dimensions represents the sources size, whose radius is on the order of 1mm corresponding to the reduced (~1 Tesla) field of the SC-magnet. The data analysis and further tests are in progress.

In summary, the science program is on a good track and everything is prepared for the long term campaign (see a contribution by M. O. Herdrich et al.).

References

[1] R. Schuch et al., JINST5, C12018 (2010)
[2] M. O. Herdrich et al., subm. to X-ray spectroscopy
[3] S. Wipf et al., HI Jena Scientific Report (2018)

*Also a part of the GSI Scientific Report 2018

Update: The XUV-comb project at HI Jena/DESY

J. Prannay Balla[1,2], Sarper Salman[1,2], Ammar Bin Wahid[1,2], Arthur Schönberg[1,2], Philip Pfäfflein[1,2], Chen Li[2], Lutz Winkelmann[2], Tino Lang[2], I. Hartl[2], C. M. Heyl[1,2] and collaborators at DESY / Vienna University / University of Neuchâtel / Ecole Politechnique / Lund University

[1]HI Jena, Germany; [2]DESY, Germany

This progress report provides a brief update of the ongoing activities towards frequency comb-based precision spectroscopy in the extreme ultraviolet (XUV), a collaborative effort between HI Jena/GSI and DESY. The hart of this project is a high-power XUV frequency comb, which is currently under development in our laboratory at DESY. Our development efforts target a multi-stage system for XUV frequency comb generation employing established schemes [1] as well as new technological concepts. The multi-stage system starts with an infrared (IR) laser frequency comb oscillator, followed by a chain of amplifiers, frequency conversion and/or temporal pulse-post compression stages and finally, by a passive power enhancement stage including an IR-to-XUV conversion setup inside a vacuum system. Our ongoing developments approach simultaneously different units of this multi-stages system. Within 2018, our main efforts have been devoted to setting up a stable IR-comb oscillator which will be complemented now by amplifier development. For the oscillator, we have chosen to employ Yb fiber-based nonlinear loop-mirror technology, an oscillator architecture, which is attracting attention as low-noise environmentally stable frequency-comb platform [2,3]. In parallel to frequency-comb laser development, a vacuum setup, which will host the passive power enhancement and IR-to-XUV conversion stage, has been prepared (Figure 1), waiting to see first in-coupled laser light. The vacuum setup will be able to host two parallel frequency conversion stages optimized for different spectroscopy demands.

Figure 1: Vacuum chamber setup, which will host a femtosecond enhancement cavity for converting the infrared frequency comb into the XUV.

Besides to our setup development in the laboratory, we are pursuing numerical code development and simulations supporting our experiments. These efforts have so far mainly been targeting a challenge reported for XUV comb systems: the efficient, high beam quality preserving post-compression of femtosecond laser pulses. While laser pulses with durations around 150 fs can be produced at sufficiently high average power to drive an XUV comb system, the efficient production of much shorter pulses with high beam quality, required for efficient intra-cavity XUV conversion, remains a challenge. Encouraged by novel post-compression schemes demonstrating efficiencies >90% and very high beam quality [4], we started a project targeting the adaption of multi-pass post-compression to the demands set by our XUV comb system. Our 3D nonlinear pulse propagation simulations (Figure 2(a)) suggest the applicability of this method for our XUV comb system, showing highly efficient post-compression options providing 25 fs pulses. Meanwhile, the method is attracting attention for other applications at DESY [5] including particle acceleration and pump-probe laser pulse production.
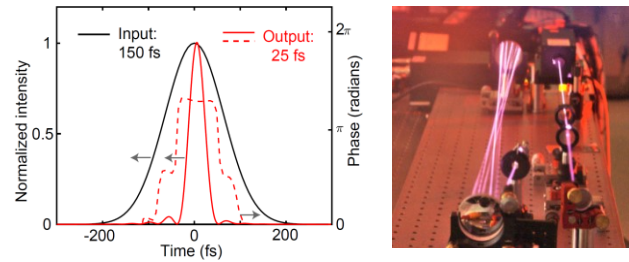
Figure 2: Multi-pass cell based spectral broadening for laser pulse-post compression prior to conversion into the XUV. 150 fs, 1 µJ input pulses cantered at 1030 nm are spectrally broadened and afterwards recompressed, reaching durations around 25 fs. (a) Simulation, (b) experimental test setup.

References

[1] G. Porat, C.M. Heyl, S.B. Schoun, C. Benko, N. Dörre, K.L. Corvin, J. Ye, "Phase-matched extreme-ultraviolet frequency-comb generation", Nature Photonics 12, 387 (2018).

[2] Lezius et al., "Space-borne frequency comb metrology", Optica 3, 1381 (2016).

[3] J. Fellinger, A.S. Mayer, G. Winkler, S. Droste, C. Li, C.M. Heyl, I. Hartl, O.H. Heckl "All-Polarization-Maintaining Dual-Color/Dual-Comb Yb:Fiber Laser", CLEO Europe CF-3.3 (2019).

[4] J. Schulte, T. Sartorius, J. Weitenberg, A. Vernaleken, and P. Russbueldt, "Nonlinear pulse compression in a multi-pass cell," Opt. Lett. 41 (2016).

[5] https://www.pier-hamburg.de/funding/pier_seed_projects/funded_projects_2018

High Resolution Ptychographic Coherent Diffractive Imaging using High-harmonic XUV Sources

Getnet K. Tadesse[1,2]*, Wilhelm Eschen[1,2], Robert Klas[1,2], Maxim Tschernajew[1,2], Frederik Tuitje[1,3], Christian Spielmann[1,3], Jens Limpert[1,2,4], Jan Rothhardt[1,2,4]

[1]Helmholtz-Institute Jena, Fröbelstieg 3, 07743 Jena, Germany
[2]Institute of Applied Physics, Friedrich-Schiller-University Jena, Albert-Einstein-Straße 15, 07745 Jena, Germany
[3]Institute of Optics and Quantum Electronics, Friedrich-Schiller-University Jena, Max-Wien-Platz 1, 07743 Jena, Germany
[4]Fraunhofer Institute for Applied Optics and Precision Engineering, Albert-Einstein-Str. 7, 07745 Jena, Germany

Introduction

Coherent diffractive imaging (CDI) is an imaging modality that avoids the use of imaging optics to enable aberration-free image reconstruction [1]. A particularly powerful variant of CDI is ptychography where an extended sample is imaged from multiple diffraction patterns taken by scanning across the sample. Although ptychography is an established technique at synchrotron facilities [2], it is only recently that more accessible setups based on high-order harmonic generation (HHG) demonstrated high photon flux ($> 10^{14}$ photons/sec) for CDI and related imaging techniques [3]. Here we present an experiment that resolved the smallest features in any table-top ptychographic setup with sizes below 50 nm (just 2.5λ) using a fiber laser driven HHG source [4].

Experimental Setup

A high average power femtosecond fiber laser system [5] was used to drive the HHG process that generated harmonics with record-high photon flux of 10^{11} photons/s at 68.6 eV [5]. For a reliable resolution characterization, a standard Siemens star sample together with a Rayleigh-type criteria was used in the experiment. The sample is raster-scanned across the XUV focus and a diffraction pattern is recorded at each point to collect a series of diffraction patterns as shown in Fig. 1.
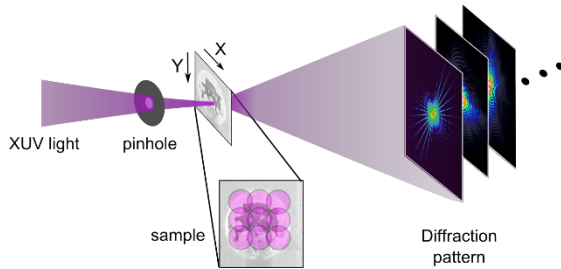
Figure 1: Schematic diagram of a ptychographic CDI setup. A pinhole with 6 µm diameter is placed ~ 400 µm upstream of the sample to have a well-defined illumination.

Iterative ptychographic algorithms [6] use the diffraction data and the redundant information from the overlapping scans to reconstruct the object as is shown in Fig. 2. Multiple rings of the Siemens star pattern are cleanly reconstructed over a field of view larger than 10 µm × 10 µm. Features with 45 nm size are resolved in the reconstruction which are the smallest features resolved in a table-top ptychographic setup.
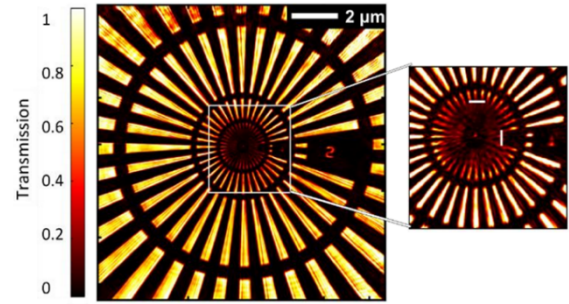
Figure 2: Ptychographic reconstruction of a Siemens star pattern [5].

Previously reported ptychographic results [7] focused on imaging large periodic objects and used the knife-edge test for resolution estimation. We found that the requirements on the experimental conditions like sample positioning accuracy and quality of the diffraction data are dramatically increased in imaging of non-periodic samples with wavelength-scale features. Propagation of the XUV beam in an optically thick (~ 100 nm) sample, such as waveguiding effects, limited the resolution of the setup in addition to minor fluctuations/drifts in the XUV beam. Applications in inspection of semiconductor masks and integrated circuits directly benefit from these results since the wavelength used is within the silicon transparency window. The rising average power of driving lasers [8] for HHG will enable improved resolution and further reduced integration times in the near future.

References

[1] Miao, J., et al. IEEE J. Sel. Topics Quantum Electron.18,399-410 (2012).
[2] Shapiro,D.,et al. Nature Photonics 8.10 (2014):765-769
[3] Klas, R., et al. Optica, 3.11 (2016), 1167-1170.
[4] Tadesse, G.K., et al. Scientific Reports 9.1(2019): 1735
[5] Rothhardt, J, et al. Optics express 24.16 (2016): 18133-18147.
[6] Enders, B., and P. Thibault. Proc. R. Soc. A. Vol. 472. No. 2196. The Royal Society, 2016.
[7] Gardner, D. F., et al. Nature Photonics 11.4 (2017): 259-263.
[8] Müller, M. et al. Optics Letters 43, 6037-6040 (2018)

Development of a heavy metal γ-ray refractive lens system for focusing beams up-to 2 MeV energies[*]

M. M. Günther[†][1,2]*, N. Sahraei*[4]*, M. Jentschel*[3]*, M. Steglich*[4]*, A. Bund*[6]*, P. G. Thirolf*[5]*, and U. Zeitner*[4]

[1]HI Jena, Jena, Germany; [2]GSI, Darmstadt, Germany; [3]ILL, Grenoble, France; [4]IAP, FSU Jena, Jena, Germany;
[5]LMU, Garching, Germany; [6]TU-Ilmenau, Ilmenau, Germany

The design and fabrication of a refractive lens system consisting of a heavy metal material for applications at MeV γ-ray energies was performed [1]. The goal is the development of a novel, nuclear based imaging method which is of potential interest in many fields of applications. The project is worked within the collaboration between the GSI/HIJ, ILL Grenoble, LMU Munich, TU-Ilmenau and the IAP Jena.

The investigation of basic optical properties of matter irradiated with visible light is of crucial importance for the development of optics in industrial as well as scientific applications. The discovery of X-ray radiation by Wilhelm Conrad Röntgen and the subsequent development of X-ray radiation sources during the last century, opened a new field in optics and optical applications. The evolution towards modern brilliant X-ray sources such as synchrotrons made the investigation of the optical properties of materials up to about 100 keV possible. This allowed for the development of novel diffractive as well as refractive optics.

Especially for the γ-ray energy range (several 100 keV to MeV) it is important to know the optical behavior of materials for refractive optics. To date, the theoretical description of the optical behaviour of materials has been validated experimentally in the X-ray energy regime from several hundreds of eV up to tens of keV. For γ-ray energies up to several MeV first experiments were performed in the last two years to verify the theory of the refractive index of several pure as well as compound materials [2]. The results were important for the development of γ-ray refractive optics.

Via optical and atomic scattering calculations and simulations we designed first heavy metal refractive lens systems for energies from 500 keV up to 2 MeV. The fabrication of a prototype 2D compound refractive lens (CRL) systems was made by different methods: laser ablation, tungsten etching and LIGA (german acronym for "Lithographie, Galvanik und Abformung"). The latter was of great sucsess with a good quality. Figure 1a) shows the lenssystem. The CRL is consisted of 100 planar parabolic biconcave lenses of gold for 1 MeV photon energy. The focal length is of 6 m. At 1 MeV photon energy the achieved simulated intensity gain of the lens system is of the factor >120, where the transmission over an effective CRL length of 110 μm is about 79% (fig. 1).

Currently first optical performance experiments of the heavy metal lenses are in work at ILL. A preliminary data analysis shows promising results in beam focusing. Further improvements and novel lens designs for γ-ray applications as well as experiments are in progress.
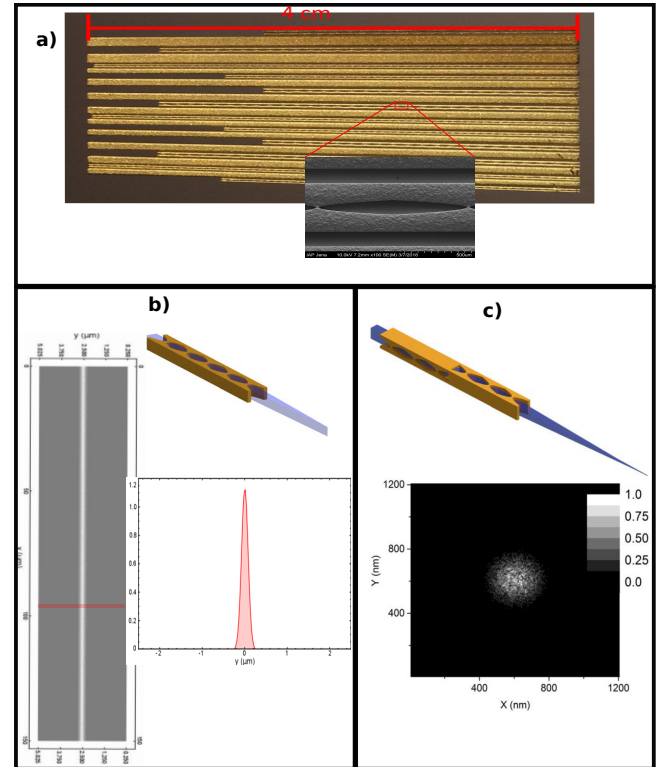
Figure 1: a) Prototype of planar parabolic and elliptic gold lens arrays with differnt sizes and alignment channels between each lens array. Below a SEM overview of one parabolic lens part. The length of The CRL is 4 cm where the effective length is 110 μm and the aperture is 150 μm. b) Line focus from optical and atomic scattering simulations of the CRL. The RMS focal size is <10 nm. c) Spot focus from optical and atomic scattering simulations usin two crossed planaar CRLs. The intensity gain at 1 MeV is more than a factor 120.

References

[1] Günther, M. M. et al. (publication in preperation).

[2] Günther, M. M. et al. "Dispersive refraction of different light-to-heavy materials at MeV γ-ray energies", Phys. Rev. A, vol. 97, 063843 (2018)

---

[*] This report is also published in the GSI Scientivic Report 2018
[†] E-mail: m.guenther@gsi.de

Forschergruppe 2015FGR0094: XUV technology and methods for imaging with nanoscale resolution [*]

S. Fuchs[† 1,2], *G. G. Paulus*[1,2], *F. Tuitje*[1,2], *M. Zürch*[2], *C. Spielmann*[1,2], *M. Tschernajew*[1,3], *J. Rothhardt*[1,3], *J. Limpert*[1,3], *M. O. Herdrich*[1], *G. Weber*[1], *and T. Stöhlker*[1,2]

[1]Helmholtz Institute Jena; [2]Institute of Optics and Quantum Electronics, Friedrich Schiller University Jena; [3]Institute of Applied Physics, Friedrich Schiller University Jena

At the Helmholtz Institute Jena, the research collaboration "Forschergruppe: XUV imaging", funded by the Thüringer Aufbaubank (TAB), combines various expertise in different fields of XUV technology inside the institute to enable nanoscale three-dimensional imaging on a lab scale. In the following, we summarize the most important results of the third-party funded project which will end after three years in April 2019.

Source Development

Laser-like and thus coherent radiation in the extreme ultraviolet regime (XUV) can be generated by using high harmonics from near-infrared ultrashort laser pulses (HHG). Although the efficiency of this process is notoriously low in the order of 10^{-6} we were able to implement HHG sources which are among the brightest in the world and perfectly suited for imaging applications by using top class ultra high average power fiber lasers [1].

Coherent Imaging

The high-flux HHG radiation was used for numerous successful coherent imaging experiments. For example, we implemented a setup for transmissive Coherent Diffraction Imaging (CDI) and thus were able to demonstrate a 10/90 resolution of 13 nm. However, in CDI the phase information needs to be retrieved using highly sophisticated iterative algorithms. To relax some of the limitation in CDI regarding the extension of the sample, Ptychography can be utilized. Here, many similar diffraction patterns from partly overlapping but different sample positions are recorded by moving the sample. The redundancy of the data enables a reliable way to retrieve the phase information and thus the structure of the sample. We could demonstrate Ptychography at laser based sources with an half-pitch resolution of 46 nm, which is a record [2]. An elegant way to circumvent the retrieval process is the Fourier transform holography imaging approach. In comparison to CDI, the phase information of the incoming beam is maintained in the diffraction pattern, due to reference holes in the sample. Using a wavelength of 18 nm, the physically possible resolution of 34 nm, given by the size of the reference holes, was reached. This is the highest resolution so far at any light source, using the Fourier transform holography method [3].

Coherence Tomography

We report on major advances of XUV Coherence Tomography (XCT), which enable artifact-free three-dimensional imaging of nanoscale objects. By using the broad bandwidth of high harmonics the axial resolution of XCT can reach a few nanometers. We could solve numerous technical hurdles and were able to implement a laser-based XCT setup. A newly developed one-dimensional phase retrieval algorithm has ultimately led to an artifact-free reconstruction of three-dimensional samples [4]. Besides the structural information we can extract the complex reflectivity from every layer in the sample from the measured spectral reflectivity and the retrieved phase and thus enable material resolution.

Detector development

Cryogenic micro-calorimeters enable photon energy resolved recording of images like diffraction patterns. Whereas monochromatic radiation is usually necessary for coherent imaging methods, those kind of detectors could record the diffraction pattern for all wavelength from a intrinsically broadband HHG source at the same time. Such a detector would be a game-changer in the field of lab-based XUV imaging since it would naturally combine monochromatic CDI with its nanoscale lateral resolution with broadband XCT with its nanoscale axial resolution. We report on first test measurements of a newly developed detector for harder x-rays demonstrating the capabilities of those detectors and paving the way for future XUV-graded versions.

The Forschergruppe has been evaluated positively and we are delighted that the Thüringer Aufbaubank finances a subsequent project for additional three years, which allows us to continue our research.

References

[1] J. Rothhardt et al., Laser Photon. Rev. **11**, 1700043 (2017).

[2] G. K. Tadesse et al., Sci. Rep. 8, 8677 (2018).

[3] G. K. Tadesse et al., Sci. Rep. 9, 1–7 (2019).

[4] S. Fuchs et al., Optica **4**, 903–906 (2017).

Forschungsgruppe: Advanced Methods for High-Resolution X-Ray Imaging[*]

M. Zepf[1,2,3], *M. Kaluza*[2,3], *A. Klenke*[2,3], *G. G. Paulus*[2,3], *Th. Stöhlker*[2,3], *I. Uschmann*[2,3], *C. Hahn*[1,2,3], *E. Liakhov*[2,3], *A. Schmitt*[2,3], *A. Kirsche*[1,2,3], *and F. Wiesner*[1,2,3]

[1]GSI, Darmstadt, Germany; [2]Helmholtz Institute Jena, Germany; [3]Friedrich-Schiller-Universität, Jena, Germany

A new *Forschungsgruppe* has been established at HI Jena, consolidating the institute's efforts in the development of laser-based X-ray sources.

X-ray imaging and diagnostics have been widely adopted for both industrial and medical applications, among other fields. However, novel high-precision imaging methods that have been developed at large-scale research facilities are difficult to implement for such applications, mainly due to the lack of suitable table top-scale high-quality X-ray sources. Laser-based sources promise to bridge this gap between recent innovations and the applications landscape. At the Helmholtz Institute Jena, a new research collaboration (*Forschungsgruppe*) was started in May 2018 and will consolidate the corresponding efforts of different groups inside the institute, and has been awarded funding by the Thüringer Aufbaubank (TAB) and the European Social Fund (ESF). Its primary goal is to prepare access to novel advances in the interlocking fields of X-ray generation and detection for potential users in industry and medicine by realizing demonstrator experiments featuring high-resolution polarimetric and imaging measurements in the X-ray spectral range.

The new research collaboration builds on expertise in the fields of laser development, X-ray optics and detector technology already existing at the Institute, as well as the results of the existing collaboration *XUV Technology and Methods for Imaging with Nanoscale Resolution*, described elsewhere in this issue of the Annual Scientific Report.

The necessary high-flux X-ray sources are realized through compact intense laser sources that use a combination of femtosecond pulse lengths and small focal diameters to achieve extremely high energy densities on target, accelerating electrons which in turn emit X-ray pulses (e.g. through betatron and bremsstrahlung radiation) whose spatial and temporal characteristics mirror those of the original laser pulse citecipiccia2011,schnell2013. This affords a spatial resolution of some $10\,\mu$m, while the pulsed emission of the source offers to extend the imaging beyond that of static objects, to dynamic processes and moving specimens [3].

Although the development of these sources will initially rely on existing research laser infrastructures, parallel efforts will strive to advance fiber laser technologies to higher pulse energies and average powers. These activities will be complemented by research into novel cryogenic detector systems which unite unprecedented spatial and energy

resolution, and the development of X-ray optics and polarizers that offer world-leading accuracy [4]. Fig. 1 outlines the structure of the collaboration, which is subdivided into three work packages, each dealing with a specific aspect of the project.

The Helmholtz Institute Jena pursues its research agenda in close interconnectedness with the Friedrich Schiller University of Jena. Accordingly, the research collaboration unites project leads from various institutes, with some primarily employed at the University. Furthermore, a tight cooperation with the Fraunhofer Institute for Applied Optics and Precision Engineering (IOF) and the Leibniz Institute of Photonic Technology (IPHT) is envisioned.
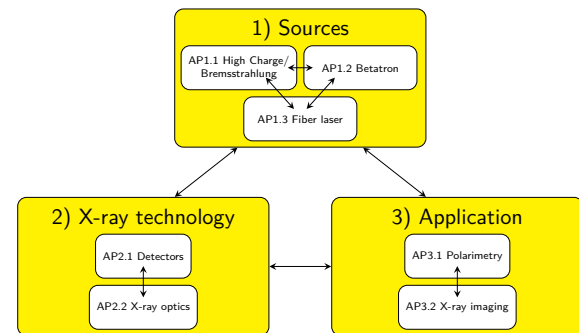
Figure 1: Schematic struture of the *Forschungsgruppe*. Novel X-ray imaging methods are investigated by tailoring X-ray source to applications, maintaining a close cooperation with laser development groups at the Helmholtz Institute. Similarly, X-ray detector and optics innovations are closely aligned to the requirements of future applications in metrology.

References

[1] S. Cipiccia, M. R. Islam, B. Ersfeld, R. P. Shanks et al., *Nat. Phys.* **7** (2011) 867.

[2] M. Schnell, A. Sävert, I. Uschmann, M. Reuter et al., *Nat. Comm.* **4** (2013) 2421.

[3] R. D. Edwards, M. A. Sinclair, T. J. Goldsack, K. Krushelnick et al., *Appl. Phys. Lett.* **80** (2002) 2129

[4] H. Bernhardt, B. Marx-Glowna, K. S. Schulze, B. Grabiger et al., *Appl. Phys. Lett.* **109** (2016) 121106

Label-free quantitative material sensitive XUV coherence tomography *

F. Wiesner[† 1,2], *S. Fuchs*[1,2], *M. Wünsche*[1,2], *J. J. Abel*[2], *J. Reinhard*[1,2], *J. Nathanael*[1,2], *S. Skruszewicz*[2], *C. Rödel*[1], *and G. G Paulus*[1,2]

[1]Helmholtz Institute Jena; [2]Institute of Optics and Quantum Electronics, Friedrich Schiller University Jena

XUV Coherence Tomography (XCT) is a derivative of Optical Coherence Tomography (OCT) for the extreme ultraviolet (XUV) spectral range. The depth structure of a sample is obtained by measuring the spectrum of the light backscattered from the sample superimposed with light reflected at the surface (common-path interferometric design) and a subsequent Fourier transform [1]. By using the broadband radiation of a high-harmonic source XCT can achieve nanoscale axial resolution.

However, the common-path interferometric XCT setup without a distinct reference wave has a characteristic disadvantage: The reconstruction only yields the autocorrelation of the sample's depth structure rather than the actual structure and, accordingly, the phase information is lost. One way to mitigate this problem is the digital recovery of the unknown phase. We successfully developed a stable one-dimensional phase retrieval algorithm (PR-XCT) which reconstructs the actual sample structure from its autocorrelation and enables artifact-free XCT [2]. Furthermore, detailed and accurate phase information strongly enhances the spectroscopic potential provided by the atomics inner-shell resonances in the XUV spectral region. With its inherently broadband spectroscopic approach and together with the recovered spectral phase, PR-XCT is a well suited tool to exploit material contrast. Therefore, depth-resolved material information in XCT can be accessed if the signal is regarded in the spatial and energy domain simultaneously. While depth information is obtained via Fourier transform, material information is encoded directly in the spectral domain.

Experiments were performed using a high-harmonic XUV source [3]. The reflected modulated spectrum was measured with a modular reflective-grating XUV spectrometer. Figure 1(a) shows the depth structure obtained for a sample consisting of a thin titanium layer and a naturally grown silicon oxide layer buried between silicon spacers on a titanium oxide substrate. The autocorrelation (blue line) is shown as well as the artifact-free structure (red line) after one-dimensional phase retrieval. This phase-retrieved signal was used to obtain the reflectivities of single layers additionally to the depth structure. The measured reflectivities were compared to a model based on the matrix formalism for the reflectivity of multi-layer interfaces. The results are shown in figure 1(b)-(e). The energy dependence of the
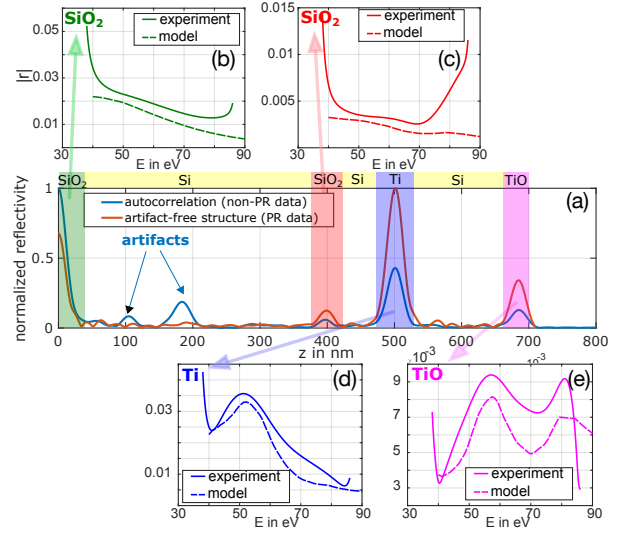
Figure 1: Experimental XCT results: (a) The Fourier transform of the measured intensity spectrum (blue) contains autocorrelation artifacts. The artifact-free structure (red) is obtained through phase retrieval. The peak amplitudes now contain the information of single layer reflectivities. (b)-(e) The effective reflectivity of single layers is obtained through a Fourier transform of the corresponding depth region. The spectral behavior enables the identification of e.g. titanium.

titanium reflectivity in the spectral window under consideration is influenced by the titanium M-edge. This behavior is clearly reproduced in the experiment and allows the distinction of titanium in comparison to other materials with similar mean reflectivity in the silicon transmission window. Due to power fluctuation of the driving laser, there is a small constant offset in absolute reflectivity. However, since material information is encoded in the gradient rather than the absolute offset, label-free element specific-identification of buried structures within a nanometer depth resolution is possible. Through algorithmic optimization of the model parameters even insights on surface roughness and layer thicknesses below the conventional XCT resolution become feasible.

References

[1] S. Fuchs, et al., Scientific Reports **6**, 20658 (2016).

[2] S. Fuchs et al., Optica **4**, 903–906 (2017).

[3] M. Wünsche et al., Optics Express **25**, 6936–6944 (2017).

Radiative electron capture as a tunable source of highly linear polarized x-rays[*]

*M. Vockert[1,2], G. Weber[1,3], H. Bräuning[3], A. Surzhykov[4,5], C. Brandau[3,6], S. Fritzsche[1,7], S. Geyer[8],
S. Hagmann[3], S. Hess[3], C. Kozhuharov[3], R. Märtin[1], N. Petridis[3], R. Hess[3], S. Trotsenko[3],
Yu. A. Litvinov[3], J. Glorius[3], A. Gumberidze[3], M. Steck[3], S. Litvinov[3], T. Gaßner[3],
P.-M. Hillenbrand[3], M. Lestinsky[3], F. Nolden[3], M. S. Sanjari[3], U. Popp[3], C. Trageser[3,6],
D. F. A. Winters[3], U. Spillmann[3], T. Krings[9], and Th. Stöhlker[1,2,3]*

[1]Helmholtz-Institut Jena; [2]Institut für Optik und Quantenelektronik, Friedrich-Schiller-Universität Jena;
[3]GSI Helmholtzzentrum für Schwerionenforschung GmbH, Darmstadt; [4]Physikalisch-Technische Bundesanstalt,
Braunschweig; [5]Fakultät für Elektrotechnik, Informationstechnik, Physik, Technische Universität Braunschweig;
[6]I. Physikalisches Institut, Justus-Liebig-Universität Gießen; [7]Theoretisch-Physikalisches Institut,
Friedrich-Schiller-Universität Jena; [8]Institut für Angewandte Physik, Goethe-Universität Frankfurt am Main;
[9]Forschungszentrum Jülich

The degree of linear polarization of K-REC radiation was measured with high precision and is compared to theory and previously published results.

Radiative electron capture (REC) is one of the most significant interactions of high energetic, highly-charged ions with matter. As REC can be approximated as the time inversed process of photoionization, it was extensively investigated both from experiment and theory during the recent decades [1]. In this work linear polarization of radiative electron capture (REC) in to the K shell has been investigated in collisions of bare xenon ions with a hydrogen gas target. The experiment was conducted at the internal gas jet target of the ESR storage ring of GSI, Darmstadt using ion beam energies of 31 MeV/u and 150 MeV/u. In this study, the degree of linear polarization of the emitted K-REC radiation was measured with dedicated Compton polarimeters [2, 3] developed by the SPARC collaboration. These detectors consist of a single planar lithium-doped silicon crystal with a thickness of about 1 cm, which is segmented into 32 horizontal strips on the front and 32 vertical strips on the back. Combining the information obtained on both sides results in a structure of 1024 quasi-pixels with the necessary position resolution for the Compton polarimetry.

Figure 1 shows a comparison of the obtained polarization data with rigorous relativistic calculations as well as with the previously published results recorded for REC into U^{92+} from [4]. Owing to the improved detector technology a significant gain in precision of the present polarization measurement (red dots) is achieved compared to the previously published results (blue and green dots) [5]. While K-REC into xenon exhibits an almost complete linear polarization, a significant depolarization due to relativistic effects is found for uranium. The experimental findings displayed are in good agreement with state-of-the-art theory

and prove that the REC process yields x-rays with a degree of linear polarization of up to nearly 100%. Furthermore, the photon energy and degree of linear polarization can be easily tuned over a broad range by varying the projectile ion species, beam energy and observation angle.
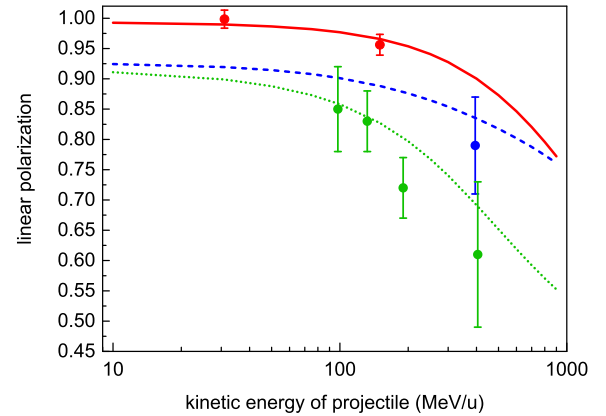
Figure 1: K-REC Polarization as a function of the collision energy for xenon and uranium projectiles in the laboratory frame. Red line: theory values for Xe^{54+} on H_2 under $90°$; Blue dashed line: theory values for U^{92+} on N_2 under $90°$; Green dotted line: theory values for U^{92+} on N_2 under $60°$; Filled dots: experimentally obtained values from [4] (blue and green) and present work [5] (red)

References

[1] J. Eichler and Th. Stöhlker, Physics Reports 439, 1 (2007)

[2] G. Weber et al., J. Instrum. 5, C07010 (2010)

[3] M. Vockert et al., Nucl. Instrum. Meth. B 408, 313 (2017)

[4] S. Tashenov et al., Phys. Rev. Lett 97, 223202 (2006)

[5] M. Vockert et al., accepted for publication, Phys. Rev. A (2019)

There is no infinitely pure linear polarization of x-rays

K.S. Schulze[1,2], H. Bernhardt[1,2], B. Grabiger[1,2], R. Loetzsch[1,2], B. Marx-Glowna[1], A.T. Schmitt[1,2], I. Uschmann[1,2], T. Stöhlker[1,2], G.G. Paulus[,2]

[1]Helmholtz Institute Jena, Germany; [2]Friedrich Schiller University Jena, Germany.

High-purity polarimetry in the x-ray range is a promising method for various scientific applications with novel x-ray sources. One of these challenging experiments is the detection of vacuum birefringence in an all-optical setup [1]. The investigation of huge magnetic fields in solid density plasma via the Faraday effect [2] as well as quantum optics with nuclei [3] are examples for the necessity of high sensitive polarimeters working in the x-ray range, too.

It is been a decade since we started working on high-purity x-ray polarimeters for these experimental needs. Although, we realized the extreme high polarization purity of $2.4 \cdot 10^{-10}$ already in 2010 [4], further attempts could not beat that value. With an improved crystal treatment and with other crystals, we were able to reproduce this purity, but could not improve it. The reasons where already known and verified by experience. But a quantitative description was still pending. Because of the theoretical work in our group [5], we can now simulate the limitations of the polarization purity, which are in accordance with experimental findings.

One important effect is multiple-wave diffraction. It arises from the three dimensional structure of the crystal. Diffraction does not only occur at the desired lattice planes. All other possible planes inside the crystal lead to diffraction, too. These modes interact with each other and lead to intensity in an otherwise polarization forbidden state. Of course, the diffracted intensity is very small far from the position where the diffraction condition is exactly fulfilled. But with regard to the high sensitivity of our polarimeters, even small intensities matter. By solving the fundamental equations of x-ray diffraction numerically, we could now simulate the influence of multiple-wave diffraction and its dependence on the azimuthal orientation of the crystal. Such simulations allow the optimal orientation of the crystal for highest polarization purities.

The second important effect is the divergence of the incoming beam. On the on hand, it leads to small deviations from the perfect Bragg angle of 45°, which can be neglected for a large number of consecutive reflections. On the other hand, the polarization vectors of beams that have the same angle to the surface but with a distinct angle to each other are not equal. That means that even if every sub-beam is perfectly linearly polarized, the total beam is a slight polarization mixture. For x-rays with a Gaussian distribution of the divergence, the polarization purity is, therefore, limited to the variance of this distribution. In a recent measurement campaign at the ESRF, we verified this behaviour experimentally. At Petra III and the old ESRF storage ring with a horizontal divergence of about 10 μrad, the polarization purity is limited to about 10^{-10}, in accordance with our measurements. The new Extreme Brilliant Source (EBS) of the ESRF as well as the European XFEL will be able to deliver beams with a divergence of about 1 μrad. Due to our preliminary work, we are confident that polarization purities reaching the extreme value of 10^{-12} are possible in the near future. The use of nearly perfect diamond crystals instead of silicon will enable such extreme purities because of its low distortion of the polarization by multiple-wave diffraction and because of its unique thermal properties with regard to the high intensity of XFEL pulses. Such an improvement of the polarization purity by two orders of magnitude will be an important cornerstone for ambitious projects like the detection of vacuum birefringence.
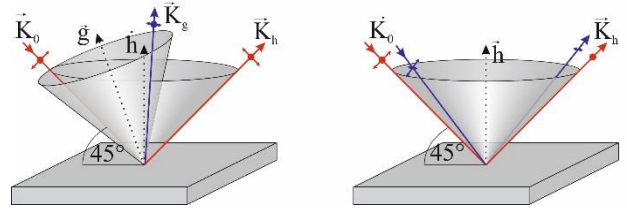
Figure 1: An artist's view of the two effects that limit the polarization purity of x-rays fundamentally. Left: Other lattice planes and, thus, other Bragg reflections change the polarization due to multiple-wave diffraction. Right: The divergence of the incoming beam leads to a limited polarization, which can be explained by separated beams, which differ from each other by their polarization vector.

References

[1] T. Heinzl, B. Liesfeld, K.-U. Amthor, H. Schwoere, R. Sauerbrey, and A. Wipf, "On the observation of vacuum birefringence", Optics Communications 267: 318, 2006.

[2] L. Huang, H.-P. Schlenvoigt, H. Takabe, and T. Cowan, "Ionization and reflux dependence of magnetic instability generation and probing inside laser-irradiated solid thin foils", Physics of Plasmas 24, 103115, 2017.

[3] J. Haber, K. S. Schulze, K. Schlage, R. Loetzsch, L. Bocklage, T. Guryeva, H. Bernhardt, H.-C. Wille, R. Rüffer, I. Uschmann, G. G. Paulus and R. Röhlsberger, "Collective strong coupling of X-rays and nuclei," Nature Photonics, 2016.

[4] B. Marx, K. S. Schulze, I. Uschmann, T. Kämpfer, R. Lötzsch, O. Wehrhan, W. Wagner, C. Detlefs, T. Roth, J. Härtwig, E. Förster, T. Stöhlker, G. G. Paulus: "High-precision x-ray polarimetry", Physical Review Letters 110, 254801, 2013.

[5] K.S. Schulze, "Fundamental limitations of the polarization purity of x rays", APL Photonics 3, 126106, 2018.

Microscopic Ghost Imaging with Different Speckle Sizes from Pseudothermal Light*

Z. Sun[1,2†], F.Tuitje[1,3], T. Helk[1,3], and C. Spielmann[1,3,]

[1]Helmholtz Institute Jena, Fröbelstieg 3, 07743 Jena
[2]Xi'an Institute of Optics and Precision Mechanics, Chinese Academy of Sciences, Xi'an 710119, China
[3]Institute of Optics and Quantum Electronics, Friedrich-Schiller-University, Max Wien Platz 1, 07743 Jena, Germany

Ghost imaging is a method to nonlocally image an object through spatial intensity correlation measurements. One of the main limitations of the resolution in pseudothermal ghost imaging is the contrast-to-noise ratio (CNR), which takes into account the level of image noise. A significant method of improving the CNR is to manipulate the speckle size by verifying aperture size. Studies [1-3] have shown that the CNR can be significantly improved by increasing the speckle size for a given object. In this report, we demonstrate a different relationship between CNR and speckle size in microscopic ghost imaging, which is significantly different from the previous results.

In order to get speckles with different sizes and increase the CNR of ghost image, we implement the experiment shown in Fig. 1. A He-Ne laser and a rotating diffuser constituted a pseudo-thermal light source. The different size of speckles is obtained by changing the incoming beam waist ω_0 which is achieved by controlling the diameter of an aperture. With the formula $\delta x_0 = \pi \lambda f / \omega_0$, we can get the desired average speckle size δx_0 by changing ω_0. The speckle beam is divided by a beam splitter into two spatially correlated beams, the transmitted and the reflected beam. The object beam hits the object "μ" and the so called bucket signal is collected with a photodiode. The reference beam never interacts with the object and is detected by the photodiode at the same distance with a CCD camera. The calculated transparent area of object 1, 2 and 3 is modulated to 0.180144 mm², 0.0776333 mm², and 0.022027 mm², respectively.
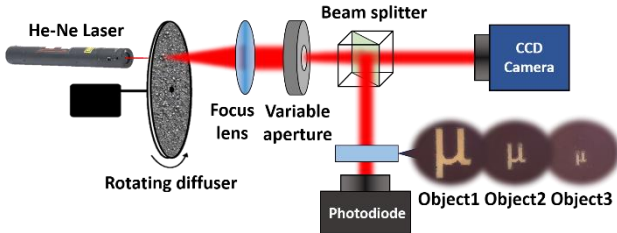
Figure 1: The schematic of the microscopic ghost imaging experimental setup.

We measured the relationships between the CNR of the ghost image of three objects and the speckle size. The results are reported in Fig. 2 where curves show different profile distributions of CNR versus speckle size. In Fig. 2(a), the CNR of object 1 increases with the speckle size almost completely in accordance to the $\sqrt{\delta x_0}$. This result is in good agreement with the theory in ref. [1-3] that the CNR is proportional to the speckle size δx_0, Then, we further explore the CNR by using object 2 as an object. It

is impressive to find that the CNR shows a quasi-Gaussian profile from the fitting curve of the experimental data in Fig. 2(b). This result indicates that the CNR of microscopic ghost imaging doesn't always increase with the speckle size. Moreover, we try to demonstrate the CNR limitation of microscopic ghost imaging by using object 3. As we can see in Fig. 2(c), for the object with the smallest transparent area, the CNR has its maximum for the smallest speckle size followed by a linear decrease with increasing speckle size.
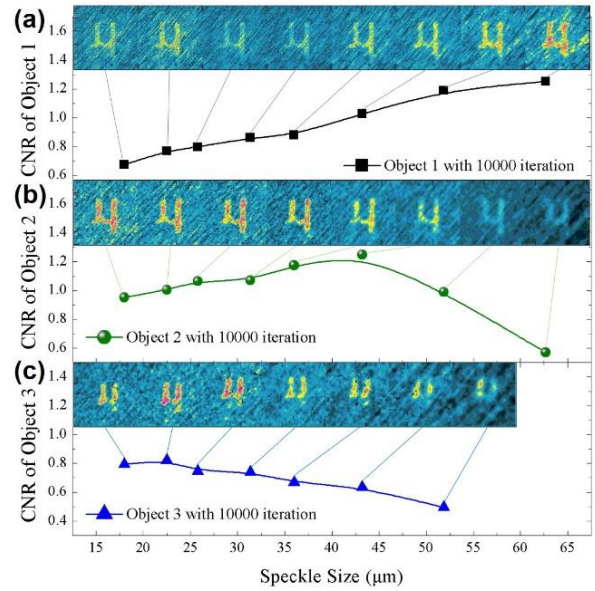
Figure 2: Speckle size versus CNR of object 1 (a), object 2 (b) and object 3 (c) with different speckle size.

To the best of our knowledge, the results in Fig.2 (b) and (c) are observed for the first time in microscopic ghost imaging. It is obvious that there is an optimal speckle size to achieve a higher CNR for a given object in microscopic ghost imaging. In order to explain this behaviour of CNR, we developed a numerical model and simulated the experiment results in Ref. [4]. It is helpful that obtaining a ghost image with higher CNR by manipulating the speckle size for a given object in microscopic ghost imaging.

References

[1] F. Ferri, D. Magatti, V. G. Sala, and A. Gatti, Appl. Phys. Lett. 92, 261109 (2008).

[2] K. W. Chan, M. N. O'Sullivan, and R. W. Boyd, Opt. Lett. 34(21), 3343-3345 (2009).

[3] F. Ferri, D. Magatti, L. A. Lugiato, and A. Gatti, Phys. Rev. Lett. 104, 253603 (2010).

[4] F. Tuitje et al., HI Jena Annual Report 2018 in preparation.

†zhe.sun@uni-jena.de

Detector noise limited visibility in microscopic ghost imaging*

F. TUITJE[1,2†], Z. SUN[1,3], T. HELK[1,2], AND C. SPIELMANN[1,2]

[1]Helmholtz Institute Jena, Fröbelstieg 3, 07743 Jena
[2]Institute of Optics and Quantum Electronics, Friedrich Schiller University, Max Wien Platz 1, 07743 Jena, Germany
[3]Xi'an Institute of Optics and Precision Mechanics, Chinese Academy of Sciences, Xi'an 710119, China

Introduction

Ghost imaging (GI) is based on the correlation of measured 2D intensity speckle pattern with the total transmitted intensity through an object illuminated with the same speckle pattern. The obtained visibility or contrast-to-noise ratio (CNR) increases with the number of measurements with different speckle patterns and the speckle sizes [1]. So far, GI is mainly tested with macroscopic objects, where the visibility increases with the square root of the speckle sizes [2]. Recent experiments [3] show a different scaling by using microscopic objects, resulting in a sudden drop of the CNR above a certain speckle size. We developed a numerical model to explain this behaviour and obtain an upper limit for speckle sizes without impairing the visibility.

Numerical model

To retrieve the important parameters, responsible for the drop in the visibility, the experiment was numerical reproduced considering free-space propagation by the angular-spectrum method. By creating randomized speckle fields with increasing speckle sizes using Fourier filtering, the experimental diffusor was copied. First, a complex-valued speckle field is produced, and multiplied with the transmission function of the object. Afterwards this product is free-space propagated to the detector under conservation of the field-of-view. The numerical detector sum up over all field elements and add noise. Here, the noise level is defined relative to the maximum and minimum intensity of the transmitted speckle field: The lowest speckle size leads to the highest intensity on the detector and vice versa. We defined the relative noise level (RNL) as

$$RNL = \frac{n - s_{min}}{s_{max} - s_{min}}$$

where s_{max} is the highest detector value at the smallest speckle size, s_{min} the lowest value at the largest speckle size and n the absolute noise. A negative RNL therefore does not affect the signal and CNR. Using 5000 iterations and a true to original scaled microscopic image of the object, the detector back-end of the experiment [3] was mimicked.

Results

After reconstruction of ghost images for 10 different RNL and 25 speckle diameters from 1 to 100 μm, the calculated CNR shows the theoretically expected behaviour for negative RNL (no noise). With increasing noise, the CNR
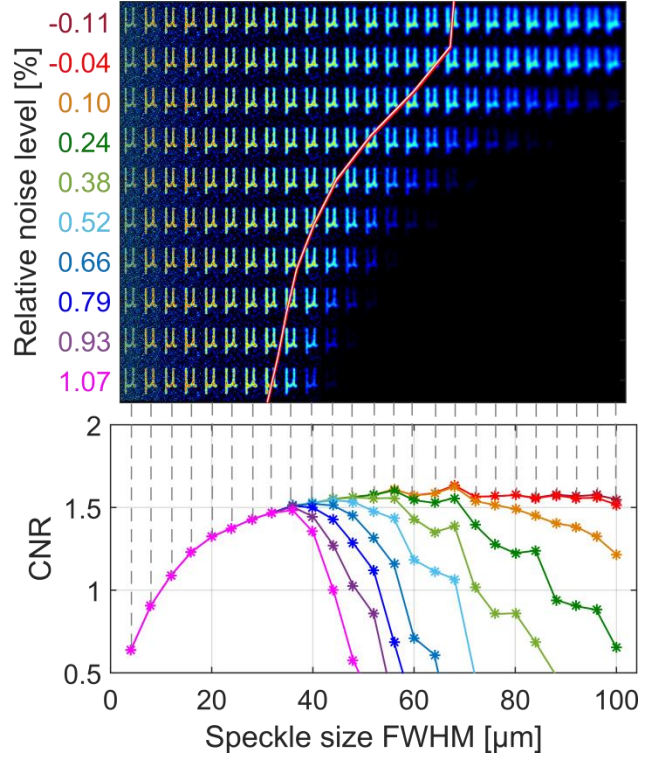
Fig. 1: Results of simulated experiment. The CNR (bottom) calculated from the ghost images (top) starts to drop with increasing RNL. The position of maximum of CNR (red-white line, top) functions were shifted to smaller speckle size

starts to drop off linearly at larger speckle sizes together with a shift of the maximum to smaller speckles. The scaling of CNR shown in Fig. 1 demonstrates the importance of adapting the speckle sizes to the noise level of the used detector and to the extent of microscopic objects to enhance the visibility of the reconstructed object. Imaging with low intensity light sources or objects susceptible to radiation damage requiring low photon flux also compete with noisy detection and therefore call out for an optimal parameter set.

References

[1] W. Jue et al., *J. Opt. Soc. Korea, JOSK*, vol. 20, no. 1, pp. 8–12, Feb. 2016.
[2] H. Li et al., *J. Opt. Soc. Am. A, JOSAA*, vol. 30, no. 9, pp. 1854–1861, Sep. 2013.
[3] Z. Sun et al., HI Jena Annual Report 2018 *in preparation*

Coherent phonon dynamics traced by high harmonic generation in ZnO

R. Hollinger[1,2,3], V. Shumakova[4], A. Pugzlys[4], A. Baltuska[4], D. Kartashov[1,2], Ch. Spielmann[1,2,3]

[1]Institute of Optics and Quantum Electronics, Friedrich-Schiller-University, Jena, Germany
[2]Abbe Center of Photonics, Friedrich Schiller University, Jena, Germany
[3]Helmholtz Institute Jena, Jena, Germany
[4] Photonics Institute, TU Wien, Vienna, Austria

High-order harmonic generation (HHG) in solids is a rapidly growing field of research in strong field laser physics [1]. The capability of using HHG for time-resolved studies of ultrafast carrier dynamics in solids has been experimentally demonstrated using strong-field THz sources [2]. Here we report for the very first time on experimental results for using HHG to trace ultrafast phonon dynamics in bulk solids.

The pump-probe experiments are carried out with 100 fs duration, 60 µJ engery laser pulses at 3.9 µm central wavelength generated by a KTA-crystal based optical parametric amplification (OPA) system pumped by a high energy Yb:CaF$_2$ laser. The output of the OPA was splitted in a pump and probe beam using a 45:55 beamsplitter. The energy and the polarization of the pump and the probe beams was adjusted independently. The pump and probe beams are seperatly focused under an angel of 10° using f = 10 cm CaF$_2$ lenses to a spot size radius of 65 µm on the surface of a c-plane oriented, 100 µm thick single crystalline ZnO slab (Crystec GmbH). The temporal delay between pump and probe pulses was set by a motorized delay line with a minimum step size of 3 nm. The spectral intensities of harmonics up to 21st order, generated in bulk ZnO by the probe pulse, were measured as a function of the pump-probe delay, intensity and polarization of the pump beam using a UV-visible spectrometer (Ocean Optics, USB 4000). All experiments were carried out at room temperature and ambient atmosphere.

| a) | b) | c) |
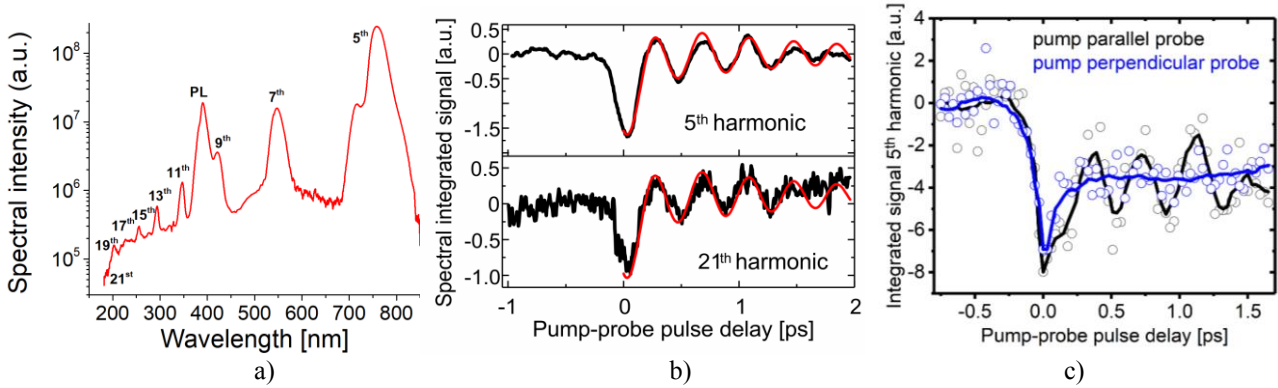
Figure 1: a) Spectrum of high-order harmonics generated by the probe pulse in unperturbed ZnO crystal; b) spectrally integrated yield of the 5th and 21st harmonics as a function of the delay relative to the pump pulse. The pump and probe have the same polarization c) spectrally integrated yield of the 5th harmonic as a function of the delay for pump and probe beam with the same (black curve) and orthogonal polarizations (blue curve), respectively;

Figure 1a) shows a typical measured high harmonic spectrum generated by the probe pulse. Figure 1b) shows the spectrally integrated signal of the 5th and 21st harmonics as a function of the pump-probe delay for a moderate pump intensity 0.57 TW/cm^2 and parallel polarized pump and probe beams. For negative delays the probe pulse arrives before the pump pulse, so the harmonic signal is generated from unexcited bulk ZnO. When both pulses are temporally overlapped, a strong damping of the yield is detected for all harmonics. When the probe pulse arrives after the pump pulse the harmonic signal is generated from the excited semiconductor, and oscillations in the harmonic yield are clearly observed (Fig.1b). Note, these oscillations are present for all measured harmonics. Fourier analysis of the data reveal an oscillation frequency of 2.8±0.2 THz corresponding to the transversal optical E_2^{low} phonon mode in ZnO [3]. The oscillations are only visible in the pump-probe traces, when the pump and probe pulse have parallel polarizations (Fig. 1c).

To conclude, for the first time we demonstrated that high harmonic generation can be used to trace lattice oscillations in semiconductors.

References

[1] S. Ghimire, D. A. Reis, "High harmonic generation from solids", Nature Physics **15**, 10–16 (2019).
[2] B. Zaks, R. B. Liu, M. S. Sherwin, "Experimental observation of electron–hole recollisions", Nature 483, 580 (2012).
[3] I. H. Lee, K. J. Yee, K. G. Lee, E. Oh, D. S. Kim and Y. S. Lim, "Coherent optical phonon mode oscillations in wurtzite ZnO excited by femtosecond pulses", Journ. Appl. Phys. 93, 4939 (2003).

Strong-field ionization of atomic and molecular systems with two-color ($\omega/2\omega$) laser pulses

S. Skruszewicz[*1,2], D. Würzler[1,2], D. Zille[1], A. M. Sayler[1,2], P. Wustelt[1,2], Y. Zhang [1], and G. G Paulus[1,2]

[1]Helmholtz Institute Jena; [2]Institute of Optics and Quantum Electronics, Friedrich Schiller University Jena

Momentum resolved photoelectron spectra from strong-field ionization of atomic and molecular systems provide wealth of information about the ionizing laser field, the target and ultrafast phenomena involved in the interaction. Disentangling these information is possible by applying controlable perturbation to the ionization process and mesuring the changes in the photoelectron spectrum. A simple scheme is provided by generating sculpted two-color laser waveforms ($\omega/2\omega$) by coherent overlap of the fundamental ionizing laser field (ω) with its weak second harmonic (2ω) and controlling their relative phase (φ_{rel}). In the strong-field ionization experiment, the 2ω field perturbs the tunneling probability and propagation of trajectories in the laser-dressed continuum. In result, the pronounced modulations in the momentum-resolved photoelectron spectrum (MRPES) can be detected. We quantify these modulations by recently introduced "phase-of-the-phase" spectroscopy [1, 2] which provide information hardly accessible with conventional photoelectron spectroscopy.

In the experiment, we ionize Xe atoms by two-color laser pulses in the sw-IR range (1800/900 nm) generated by the interferometer synthesizing $\omega/2\omega$ waveforms for wavelenghts in the range $1200 - 3500\,\mathrm{nm}$. The momentum-resolved photoelectron spectra are recorded by the velocity-map imaging spectrometer (VMI) capable of resolving the photoelectrons emitted with kinetic energy up to $400\,\mathrm{eV}$. The detection scheme has been optimized to detect single electron events and discriminate statistical noise.

To analyze changes in the MRPES with respect to the φ_{rel}, we Fourier-analyze the φ_{rel}-dependent photoelectron yield and consider only term $Y_1(\mathbf{p}, \varphi_{rel}) = Y(\mathbf{p})\cos[\varphi_{rel} + \Phi(\mathbf{p})]$ for each final momentum (p_x, p_z). This is permissible for weak perturbations because the signal oscillates predominantly with 2ω field periodicity. The phase dependencies in the photoelectron yield can be represented by two functions: the relative phase contrast (RPC,Y) encoding the amplitude of the signal modulation and the phase-of-the-phase (PP,Φ) encoding the phase of the periodic photoelectron signal modulation with respect to the relative phase φ_{rel} of the $\omega/2\omega$ laser pulse. Fig.1 shows the MRPES (a) and PP spectrum (b) resulting from the Fourier analysis. By comparing the experimental PP spectrum with the results of three-dimmensional semi-
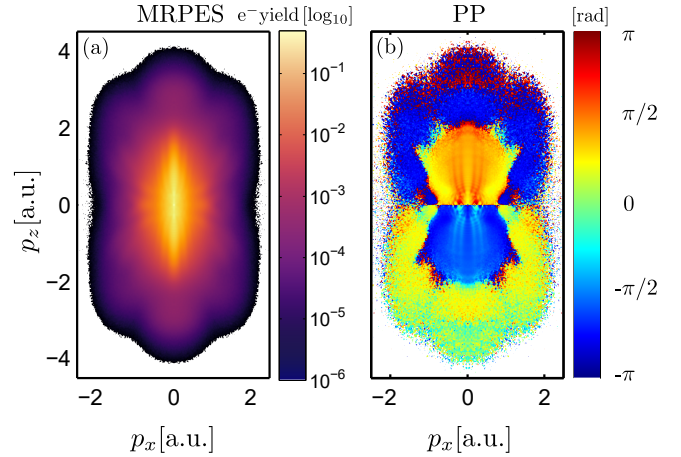
Figure 1: Left: The momentum-resolved photoelectron spectrum (MRPES) from Xe atoms ionized with 40 fs $\omega/2\omega$ laser pulses (($1800/900\,nm$) with intensity $I_{omega} = 4 \cdot 10^{13}\,\mathrm{W/cm^2}$ and $I_{omega} = 2 \cdot 10^{11}\,\mathrm{W/cm^2}$. Right: the phase-of-the-phase (PP) spectrum encoding the phase of the periodic photoelectron signal modulation with respect to the relative phase φ_{rel} of $\omega/2\omega$ laser pulses.

classical trajectory calculations we found, that the information on the ionization time of electrons can be retrieved from PP spectrum with precision of 80 as. Our analysis shows, that the upper limit for exact determination of the ionization time is independent on intensity of the perturbative 2ω field and is due to modulations of the electron trajectories in the laser-dressed continuum.

Our ongoing efforts concentrates on extending the "phase-of-the-phase" spectroscopy towards the experiments in the mid-IR range (3200/1800 nm) and apply to investigate photoionization and molecular dynamics in neutrals and ions generated by the ion-beam apparatus. The experiments on the C_{60} fullerene will provide an unique benchmark for testing the rescattering dynamics from extended multielectron molecular systems of size comparable with the width of the recolliding wavepacket.

References

[1] S. Skruszewicz, et al., Phys. Rev. Lett **115**, 043001 (2015).

[2] D. Würzler et al., J. Phys. B **51**, 015001 (2017).

*slawomir.skruszewicz@uni-jena.de

Isotope Effect in laser induced fragmentation of HeH+

P. Wustelt[1,2], F. Oppermann[3], L. Yue[4], A.M. Sayler[1,2], T.Stöhlker[1,2], S.Gräfe[4], M. Lein[3] and G.G. Paulus[1,2]

[1]Helmholtz Institut Jena, Germany; [2]Institute for Optics and Quantum Electronics, Friedrich-Schiller-University Jena, Germany; [3]Institut für Theoretische Physik, Leibniz Universität Hannover, [4]Institute for Physical Chemistry, Friedrich-Schiller-University Jena, Germany

In this project, we experimentally study the laser-induced fragmentation of the HeH+ molecular ion and its isotopologues. The extreme asymmetric nature of HeH+, which is manifested in a strong permanent dipole, results in fundamentally different fragmentation dynamics than those seen in homonuclear molecules, giving a valuable new insight in heteronuclear systems.

In contrast to the prevailing interpretation of strong-field fragmentation, in which stretching of the molecule results primarily from laser-induced electronic excitation, experiment and theory for non-ionizing dissociation, single ionization and double ionization both show that the direct vibrational excitation plays the decisive role for the asymmetric HeH+ [1,2].

We are further able to understand and manipulate the dynamics by using ^{4}HeD+, which effectively slows down the fragmentation process by increasing the reduced mass, $\mu = m_1 m_2/(m_1 + m_2)$ by 67 %.

In the measurement the ion must be synthesized and prepared in an ion beam apparatus. For these measurements presented here, a HeH+ (HeD+) ion beam is created in a duoplasmatron ion source using a mixture of helium and hydrogen (deuterium) gas. Intensive laser pulses are then focused into the interaction region of the ion beam coincidence 3D momentum imaging setup, which is regularly operated at the HI Jena [3]. Three-dimensional momentum distributions of the nuclear fragments of all fragmentation pathways of HeH+ and HeD+ were measured for different laser intensities [2,4].
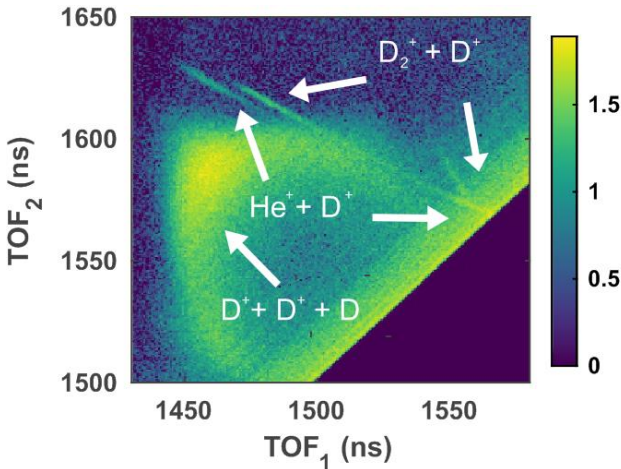
Unfortunately, measurements with ^{4}HeD+ are very challenging because the synthesis of ^{4}HeD+ inevitably produces a large fraction of D_3^+, which has virtually the same molecular mass [2]. A pure ^{4}HeD+ ion beam can therefore not be realized. Nevertheless, by taking advantage of coincidence detection and the high precision of our apparatus, we were able to distinguish the single ionization channels of HeD+→ He+ + D+ + e- and D_3^+→ D_2^+ + D+ + e- by applying an electrostatic field in the interaction region and relying on the extremely small, 6:1000, mass defect. Discriminating the fragments of D_3^+ in the measured coincidence time-of-flight distributions (see Fig. 1) allows to compare the KER spectra of the ^{4}HeH+ and its isotopologue ^{4}HeD+, where we find higher KERs in ^{4}HeD+ as compared to ^{4}HeH+.

In addition to its larger reduced mass, ^{4}HeD+ has a smaller dipole moment compared to ^{4}HeH+. Both aspects slow down stretching, as can be seen in the reduced population of higher vibrational states for ^{4}HeD+, see Fig.2(b), with the consequence that higher intensities are required for ionization as the ionization potential increases with decreasing internuclear distance. As a result the ionization of ^{4}HeD+ occurs at smaller distances and produces higher KERs as compared to ^{4}HeH+, see Fig. 2(a).
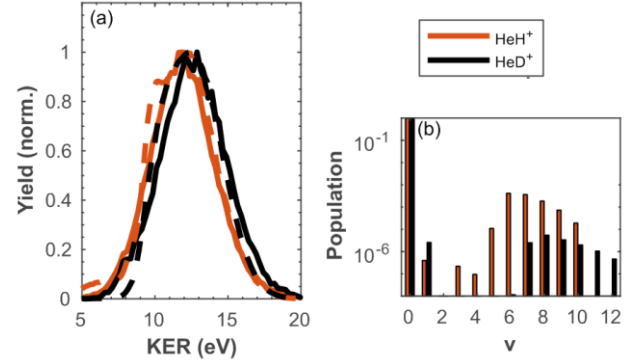
Figure 2: Single ionization of ^{4}HeH+ and ^{4}HeD+: (a) Measured KER spectra for 800 nm are displayed at a peak intensity of $\approx 10^{17}$ W/cm² (solid curves). The corresponding spectra obtained by TDSE-simulations are represented by dashed curves. (b) The larger mass of HeD+ inhibits stretching, which results in less population of the excited vibrational states as compared to HeH+.

Figure 1: The time-of-flight coincidence map for a ^{4}HeD+ measurement. The diagonal for the fragments ^{4}He+ + D+ is separated from the one for D_2^+ + D+ by approximately 5 ns. The large structure originates from the D+ + D+ + D channel.

References

[1] D. Ursreyet al., *Phys. Rev. A* **85**, 023429 (2012).
[2] P. Wustelt et al., *Phys. Rev. Lett.* **121**, 073203 (2018)
[3] T. Rathje, et al., *Phys. Rev. Lett.* **111**, 093002 (2013)
[4] L. Yue, *Phys. Rev. A* **98**, 043418 (2018)

Charge State Tailoring of highly relativistic heavy ion beams - Comparison of Theory and Experiment

F. M. Kröger[1,2 *], G. Weber[2,3], V. P. Shevelko[4], S. Hirlander[5], R. Alemany-Fernández[5], K. Cornelis[5], B. Goddard[5], F. M. Velotti[5], M. W. Krasny[5,6], and Th. Stöhlker[1,2,3] on behalf of the Gamma Factory study group

[1]FSU Jena, IOQ, Jena, 07743, Germany, [2]HI Jena, Jena, 07743, Germany, [3]GSI Helmholtzzentrum für Schwerionenforschung GmbH, Darmstadt, 64291, Germany, [4]LPI RUS, Moscow, 119333, Russia, [5]CERN, Geneva, 1211, Switzerland, [6]LPNHE, University Paris Sorbonne, CNRS-IN2P3, Paris, 75252, France

To find the optimal target material and thickness for the efficient production of Pb^{80+} and Pb^{81+} out of Pb^{54+} ions at 5.9 GeV/u charge state evolution calculations have been performed using the BREIT code [1], which was recently developed within the SPARC collaboration. This study was conducted within the Gamma Factory [2] study group of CERN, however stripping scenarios at such high energies are also highly relevant for the upcoming FAIR facility.

In contrast to the GSI and to the future FAIR facility, usually only fully stripped ions were produced at CERN for the use in particle physics studies. The production of ions having charge states which differ from the equilibrium charge state, which corresponds at high energies to the bare ion species, is more challenging since it requires the design of non-equilibrium stripper foils, taking into account the stripper foils material and thickness. In contrast to commonly used codes, this algorithm has no built-in cross-sections, so it can be used for arbitrary beam energies and charge states as long as the relevant cross-sections are provided by the user.

Due to these preparatory studies an Al stripper foil was chosen for the first proof-of-principle experiment performed in 2018 at CERN, where Pb^{80+} and Pb^{81+} ions were successfully produced and stored in the SPS. The preliminary experimental data (red and black cross in Fig.1) allowed to benchmark continuative BREIT calculations which followed a subsequent investigation concerning ion beam lifetimes that identified Pb^{79+} as appropriate candidate, because its transitions can be efficiently driven by available optical lasers by taking into account the Doppler blue shift. The quite large uncertainty of the L-shell ionization cross-sections and the rare experimental data lead to two different benchmarking methods (dash-dotted and dashed lines in Fig.1) which, nevertheless, allowed to confine the thickness area where the maximum yield of Pb^{79+} is expected (orange bar). Experimental CERN data from 1996 [3] (green crosses in Fig.1) confirms the reliability of the prediction results, and of the benchmarking methods. The comparison with the data, measured at 4.2 GeV/u, is justified since at such energies the cross-sections of the by far dominating ionization process are approximatively constant. The production of Pb^{79+} will be subjet to a further proof-of-principle experiment at CERN, scheduled in the near future.
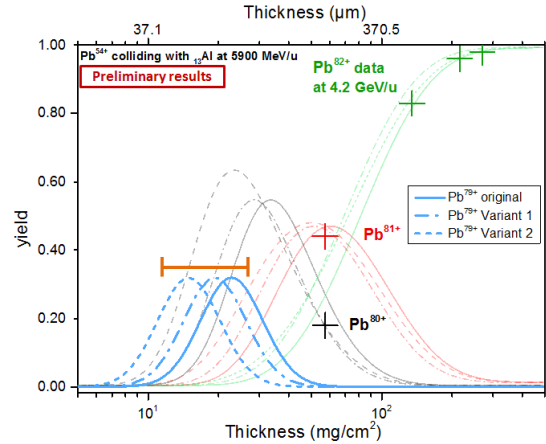
Fig.1: Comparison of theory results before (full lines) and after benchmarking (dash-dotted and dashed lines) with preliminary experimental data (red and black crosses), as well as with experimental CERN data from 1996 (green crosses).

References

[1] Winckler N. *et al*, 2017, *NIM B* **392** 67
[2] Krasny M. W., 2015, arXiv:1511.07794
[3] Arduini G. *et al*, 1996, *Proceedings of the 5th European Particle Accelerator Conference*

---

*E-mail: felix.kroeger@uni-jena.de

Theory

Photon Scattering at the High-Intensity Frontier

H. Gies[1,2], F. Karbstein[1,2], C. Kohlfürst[1,2], and N. Seegert[1,2]

[1]Helmholtz-Institut Jena, Germany; [2]Theoretisch-Physikalisches Institut, FSU Jena, Germany

The tremendous progress in high-intensity laser technology and the establishment of dedicated high-field laboratories in recent years have paved the way towards a first observation of quantum vacuum nonlinearities at the high-intensity frontier. We advocate a particularly prospective scenario, where three synchronized high-intensity laser pulses are brought into collision, giving rise to signal photons, whose frequency and propagation direction differ from the driving laser pulses, thus providing various means to achieve an excellent signal to background separation. Our study is the first to predict the precise angular spread of the signal photons, and paves the way for a first verification of quantum vacuum nonlinearity in a well-controlled laboratory experiment at one of the many high-intensity laser facilities currently coming online.

The vacuum of quantum electrodynamics (QED) is characterized by the omnipresence of fluctuations of electrons, positrons and photons. These fluctuations mediate effective interactions among electromagnetic fields [1], thereby invalidating one of the cornerstones of Maxwell's classical theory of electrodynamics, namely the celebrated superposition principle for electromagnetic fields in vacuum. However, having no classical analogue, such *vacuum nonlinearities* are typically rather elusive in experiment. Our work builds on the recent observation that optical signatures of quantum vacuum nonlinearities in inhomogeneous electromagnetic fields can be efficiently analyzed by reformulating them as *vacuum emission* processes [2]. In this picture, signatures of vacuum nonlinearities are encoded in *signal photons* induced in the interaction volume of the high-intensity laser pulses driving the effect. The latter are formally described as classical background fields, which is well-justified, because laser beams propagating in vacuum are optimal examples for coherent macroscopic fields.

In Ref. [3], we investigate photon-photon scattering in the collision of three synchronized high-intensity laser pulses modeled as pulsed paraxial Gaussian beams [4]. More specifically, we focus on two different experimental scenarios, both of which will become possible in the near future at various high-intensity facilities. In contrast to previous studies, our formalism does not require any additional *ad hoc* approximations: upon specification of the macroscopic electromagnetic fields of the high-intensity laser beams, the signal photons and their polarization and propagation properties are unambiguously predicted. We obtain $N \approx 2.42$ signal photons per shot for a collision scenario based on the availability of two 1 PW lasers. For the design parameters of ELI-NP [5] envisaging two 10 PW lasers, this number would even increase by a fac-
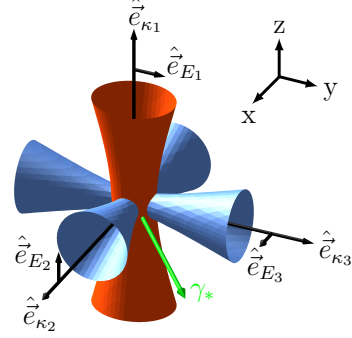
Figure 1: Illustration of a three dimensional collision geometry, displaying the propagation directions $\hat{\mathbf{e}}_{\kappa_b}$ and polarization vectors $\hat{\mathbf{e}}_{E_b}$ of the high-intensity laser beams. The dominant emission direction (φ_*, ϑ_*) of the signal photons γ_* is highlighted by an arrow.

tor of 1000. As the dominant scattering process is characterized by the absorption of two frequency-doubled laser photons and the emission of one low-energy fundamental-frequency laser photon, the signal photons exhibit a distinct frequency $\omega_* \approx 3\omega$, different from the frequencies $\omega_1 = \omega$ and $\omega_{\{2,3\}} = 2\omega$ of the driving high-intensity lasers. Moreover, they are emitted into a specific direction outside the forward cones of the laser beams driving the effect. Both properties should allow for an excellent signal to background separation in experiment.

Our results substantiate previous estimates suggesting the possibility of measuring signatures of QED vacuum nonlinearity with state-of-the-art technology [6]. They suggest that a first discovery experiment of nonlinear interactions of macroscopically controllable electromagnetic fields is in reach with the present generation of high-intensity lasers coming online just now in many laser labs worldwide – decades after the seminal work of Ref. [1].

References

[1] W. Heisenberg and H. Euler, Z. Phys. **98**, 714 (1936).

[2] F. Karbstein and R. Shaisultanov, Phys. Rev. D **91**, 113002 (2015).

[3] H. Gies, F. Karbstein, C. Kohlfürst and N. Seegert, Phys. Rev. D **97**, 076002 (2018).

[4] H. Gies, F. Karbstein and C. Kohlfürst, Phys. Rev. D **97**, 036022 (2018).

[5] ELI, https://eli-laser.eu/ .

[6] E. Lundström, *al.*, Phys. Rev. Lett. **96**, 083602 (2006).

All-optical signatures of quantum vacuum nonlinearities in generic laser fields

A. Blinne[1,3], H. Gies[1,2], F. Karbstein[1,2], C. Kohlfürst[1,2], and M. Zepf[1,3]

[1]Helmholtz-Institut Jena, Germany; [2]Theoretisch-Physikalisches Institut, FSU Jena, Germany; [3]Institut für Optik und Quantenelektronik, FSU Jena, Germany

All-optical experiments at the high-intensity frontier offer a promising route to unprecedented precision tests of quantum electrodynamics in strong macroscopic electromagnetic fields. So far, most theoretical studies of all-optical signatures of quantum vacuum nonlinearity are based on simplifying approximations of the beam profiles and pulse shapes of the driving laser fields. Since precision tests require accurate quantitative theoretical predictions, we introduce an efficient numerical tool facilitating the quantitative theoretical study of all-optical signatures of quantum vacuum nonlinearity in generic laser fields.

Up to now, theoretical studies of all-optical signatures of quantum vacuum nonlinearity [1] have typically involved various simplifying approximations of the beam profiles and pulse shapes of the driving laser fields, such as plane-wave based models, constant crossed fields amended with a pulse shape envelope, or more realistic laser pulses in the paraxial approximation. However, any such approximation inherently limits the accuracy of predictions for experiments, and thus the precision with which theory can be tested.

In Ref. [3], we substantially advance the theoretical modeling of all-optical signatures of QED vacuum nonlinearities in experimentally realistic field configurations by evaluating the effect in generic laser fields, manifestly fulfilling Maxwell's equations in vacuum. To this end, we rely on a few well-justified and parametrically controlled fundamental approximations detailed below, and employ a Maxwell solver, recently put forward in Ref. [2], to numerically solve the dynamics of the macroscopic electromagnetic fields driving the vacuum emission effect self-consistently. This facilitates the study of all-optical signatures of QED vacuum nonlinearities in very generic, experimentally relevant electromagnetic fields in full 3+1 space-time dimensions. Most importantly, our approach allows us to easily overcome the limitations of any approximation for the laser beams. No ad-hoc ansatz for the temporal pulse profile is required, allowing for the study of all-optical signatures of QED vacuum nonlinearities in arbitrary, experimentally determined 'real world' laser fields.

Our approach resolves the obvious mismatch of analytical approaches studying signatures of quantum vacuum nonlinearities in electromagnetic fields which solve the wave equation only approximately, such as, e.g., plane-wave based models, crossed-field models with pulse-shape envelopes or pulsed paraxial beams. This is of particular importance as the deviations of results derived from approximate vs. exact solutions of the wave-equation are typically hard to assess quantitatively. They, however, amount
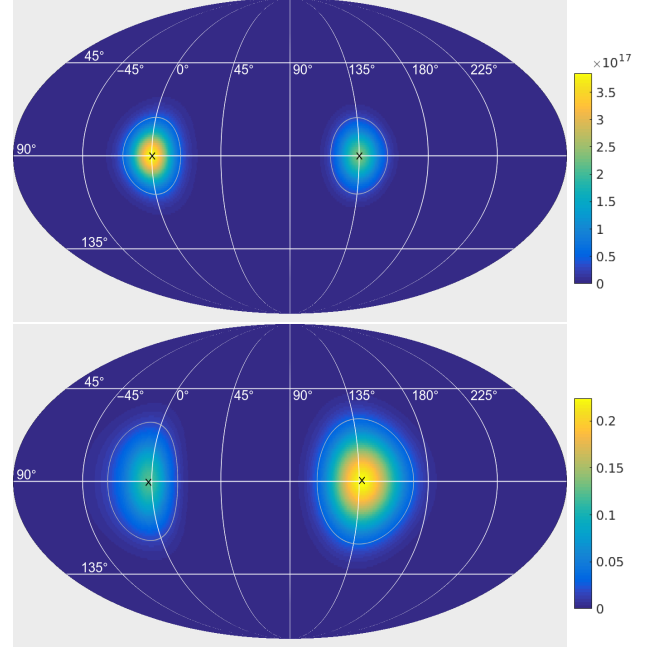
Figure 1: Differential numbers $\frac{\mathrm{d}\mathcal{N}}{\mathrm{d}\varphi\,\mathrm{d}\cos\vartheta}$ and $\frac{\mathrm{d}N_{\mathrm{tot}}}{\mathrm{d}\varphi\,\mathrm{d}\cos\vartheta}$ of laser photons $\mathcal{N}$ (top) and signal photons N_{tot} (bottom) plotted for the full solid angle; longitude φ, latitude ϑ. We consider the collision of two high-intensity laser pulses of the same wavelength ($\lambda = 800\,\mathrm{nm}$) with beam axes in the xy-plane under $\varphi_{\mathrm{coll}} = 135°$; the directions of the beam axes are marked by black crosses in the top figure. Both pulses are focused to $w_0 = \lambda$ and polarized along $\mathbf{e}_{\mathrm{z}}$ in the focus. The pulse propagating along the positive x-axis ($\varphi = 0°, \vartheta = 90°$) has an energy of $W_{0°} = 50\,\mathrm{J}$ and a duration of $\tau_{0°} = 5\,\mathrm{fs}$. The energy and duration of the other pulse are $W_{135°} = 30\,\mathrm{J}$ and $\tau_{135°} = 30\,\mathrm{fs}$, respectively. As to be expected, the signal photons are predominantly emitted in the forward directions of the driving laser beams.

to a critical unknown, limiting the achievable accuracy of predictions for experiments based on approximations of the driving laser fields.

References

[1] W. Heisenberg and H. Euler, Z. Phys. **98**, 714 (1936).

[2] A. Blinne, S. Kuschel, S. Tietze and M. Zepf, [arXiv:1801.04812 [physics.plasm-ph]].

[3] A. Blinne, H. Gies, F. Karbstein, C. Kohlfürst and M. Zepf, Phys. Rev. D **99**, 016006 (2019).

Efficient retrieval of phase information from real-valued electromagnetic field data

A. Blinne[1], S. Kuschel[1,2], S. Tietze[1], and M. Zepf[1,2]

[1]Helmholtz-Institut Jena, Germany; [2]IOQ, ACP, FSU Jena, Germany

While analytic calculations may give access to complex-valued electromagnetic field data which allow trivial access to envelope and phase information, the majority of numeric codes uses a real-valued representation. We show that by combining the real-valued electric and magnetic field at a single point in time, we can directly reconstruct the full information of the electromagnetic fields in the form of complex-valued spectral coefficients ($\vec{k}$-space) at a low computational cost of only three Fourier transforms. The method allows for counter propagating plane waves to be accurately distinguished as well as their complex spectral coefficients, i. e. spectral amplitudes and spectral phase to be calculated. An implementation of the new method is available as part of PostPic[1], a data analysis toolkit written in the Python programming language.

The method presented in this work has the advantage that it can reconstruct the full complex $\vec{k}$-space from the information contained in a single standard data dump which contains only the real-valued electric and magnetic fields. As this method is based upon a spectral representation, the heavy lifting of the computation is done by a single discrete fourier transform for each input field component. Afterwards the reconstructed fields can be directly calculated, without the need to solve equations numerically or using an iterative method. Additionally, very fast implementations are readily available for discrete fourier transforms. Apart from the high computational efficiency, we managed to adapt this method to some of the specific characteristics of finite difference time domain solvers which greatly improves the accuracy as compared to a naïve approach that is based solely on Maxwell theory.

In the one-dimensional case it is well known, that the waves propagating in either direction can be separated using information from only a single simulation dump by the linear combinations

$$E_y^+ = \frac{1}{2}\left(E_y + cB_z\right), \quad E_y^- = \frac{1}{2}\left(E_y - cB_z\right), \quad (1)$$

which is true in both, spatial domain and frequency domain. We extend this method to three dimensional data.

The reconstruction of the complex amplitudes of the E_y component from a single data dump from EPOCH follows a number of steps. The first step is to extract the real-valued fields $E_y(\vec{r})$, $B_x(\vec{r})$ and $B_z(\vec{r})$ from the dump, noting the positions $\vec{r}_0^{E_y}$, $\vec{r}_0^{B_x}$ and $\vec{r}_0^{B_z}$ of the origins of their respective spatially staggered grids. After a Fourier transform is applied to each, obtaining $E_y^F(\vec{k})$, $B_x^F(\vec{k})$ and $B_z^F(\vec{k})$, a linear
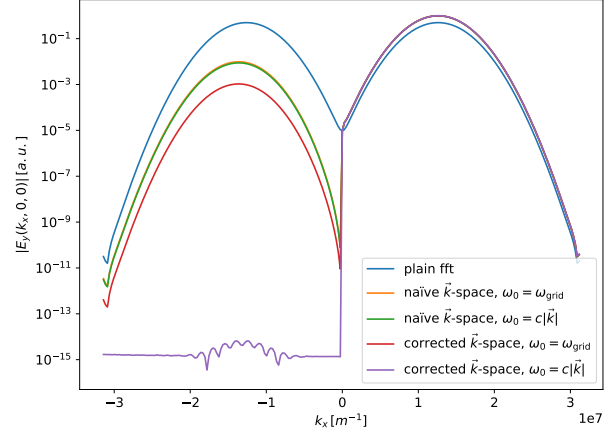
Figure 1: Comparison between the spectra given by a simple fft, reconstructed $\vec{k}$-space with ("corrected") or without correction ("naïve") for the response function of the linear interpolation, both combined with both options for $\omega(\vec{k})$ in Eq. (4) each.

phase is multiplicatively applied to two of the three fields, in order to align the grid origin points

$$B_{x/z}^F(\vec{k}) \rightarrow e^{i\vec{k}\cdot\left(\vec{r}_0^{E_y} - \vec{r}_0^{B_{x/z}}\right)} B_{x/z}^F(\vec{k}). \quad (2)$$

As both the electric and the magnetic field are given at the same time, one of the fields has completed a full update step, while the other is only updated half-way. In this example, the magnetic field needed to be corrected for the frequency response of the half-step update according to

$$B_{x/z}^F(\vec{k}) \rightarrow \frac{1}{\cos\left(\frac{1}{2}\omega_{\text{grid}}(\vec{k})\,\Delta t\right)} B_{x/z}^F(\vec{k}). \quad (3)$$

After applying these two corrections, the complex amplitudes of E_y can be reconstructed following

$$\mathbf{E}_{y,\vec{k}} = \vec{E}_y^F(\vec{k}) - \frac{\omega(\vec{k})}{k^2}\left(k_x B_z^F(\vec{k}) - k_z B_x^F(\vec{k})\right). \quad (4)$$

References

[1] A. Blinne, S. Kuschel, S. Tietze, M. Zepf, "Efficient retrieval of phase information from real-valued electromagnetic field data", J. Comp. Phys: X 1, 100019 (2019)

[2] A. Blinne, D. Schinkel, S. Kuschel et al., "A systematic approach to numerical dispersion in Maxwell solvers", Comput. Phys. Commun. 224, 273 (2018)

---

[1]See https://github.com/skuschel/postpic

Boosting all-optical signatures of quantum vacuum nonlinearities by coherent harmonic focusing[*]

A. Blinne[1], H. Gies[1,2], F. Karbstein[1,2], and M. Zepf[1,3]

[1]Helmholtz-Institut Jena, Germany; [2]TPI, ACP, FSU Jena, Germany; [3]IOQ, ACP, FSU Jena, Germany

We show that coherent harmonic focusing provides an efficient mechanism to boost all-optical signatures of quantum vacuum nonlinearity in the collision of high-intensity laser pulses. Assuming two laser pulses of given parameters at our disposal, we demonstrate a substantial increase of the number of signal photons measurable in experiment when one of the pulses undergoes coherent harmonic focusing before it is collided with the fundamental-frequency pulse. Our results suggest that coherent harmonic focusing may pave the way towards a first detection of signatures of quantum vacuum nonlinearities at the high-intensity frontier in the laboratory.

The quantum vacuum is not empty and inert, but amounts to a highly non-trivial quantum state. In order to obtain a measurable response, the quantum vacuum fluctuations have to be excited by some external stimulus. A convenient means is provided by strong macroscopic electromagnetic fields coupling directly to the electrically charged particle sector. The leading effect then amounts to the effective coupling of the prescribed electric $\vec{E}$ and magnetic $\vec{B}$ fields via a virtual electron-positron pair. This process is governed by quantum electrodynamics (QED) and supplements Maxwell's classical equations in vacuum with effective nonlinear couplings of the electromagnetic fields [1]. The vacuum emission approach to the phenomenon of light-by-light scattering lead to the development of a numerical code to calculate the all-optical signal in the form of signal photons detailed in [3].

Reference [2] demonstrated that coherent harmonic focussing (CHF) can pave the way towards extreme intensities in the laboratory. They showed that the reflection of a relativistically intense few-femtosecond laser pulse from the oscillating boundary of a overdense plasma produces a harmonic spectrum with the spectrum intensity scaling as $I_n \sim n^{-5/2}$, where $1 \leq n \leq n_{\max}$ labels the nth harmonic. Using a concave plasma surface of the adequate curvature, these harmonics can be focused coherently down to a spot size of about λ/n, with the wavelength of the initial laser pulse given by λ [2]. In the setup studied here, this coherently focused "$-$" pulse travels along the negative x axis and is collided with a fundamental mode monochromatic Gaussian "$+$" laser pulse of the same total energy traveling along the positive x axis.

Assuming the effective waist and pulse duration and Rayleigh range of the CHF pulse made up of $n_{\max}$ harmon-
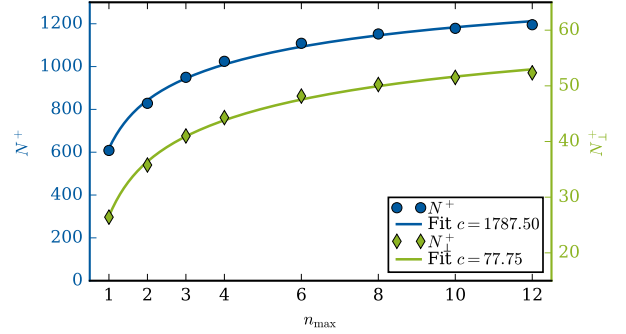
Figure 1: Scaling of the total numbers of signal photons N^+ (blue dots; left scale) and $N_\perp^+$ (green diamonds; right scale) emitted in + direction with the harmonic cutoff $n_{\max}$. The solid lines are least squares fits to Eq. (1).

ics to scale as $w_{\mathrm{CHF}} = w_0/n_{\max}$ and $\tau_{\mathrm{CHF}} \sim z_{R,\mathrm{CHF}} \sim 1/n_{\max}$, the results for the attainable numbers of signal photons emitted in forward direction are remarkably well described by

$$N_{(p)}^+(n_{\max}) = c_{(p)}^+ \, \frac{1/n_{\max}}{1 + 2/n_{\max}^2} \frac{(\sum_{n=1}^{n_{\max}} n^{-\frac{1}{4}})^4}{(\sum_{m=1}^{n_{\max}} m^{-\frac{5}{2}})^2} \,, \quad (1)$$

as visualised in Fig. 1.

The accurate description of $N_{(p)}^+$ by Eq. (1) suggests that the angular decay of $N_{(p)}^+$ should be well-described by Eq. (4) of Ref. [4], which has been confirmed by our numerical findings. A comparison of the angular decay in that equation with the angular decay of the incident beam shows that the radial divergence of the signal photons emitted into the + half-space

$$\theta_{\mathrm{sig}}^+(n_{\max}) \simeq \theta \sqrt{\frac{1 + 8n_{\max}^2}{1 + 2n_{\max}^2}} \,, \quad (2)$$

is much larger than the radial divergence θ of the driving laser beam, suggesting the possibility of detection in experiment.

References

[1] H. Euler and B. Kockel, Naturwiss. **23**, 246 (1935).

[2] S. Gordienko, A. Pukhov, O. Shorokhov and T. Baeva, Phys. Rev. Lett. **94**, 103903 (2005).

[3] A. Blinne, H. Gies, F. Karbstein, C. Kohlfürst and M. Zepf, Phys. Rev. D **99**, 016006 (2019) [arXiv:1811.08895].

[4] F. Karbstein, Phys. Rev. D **98**, 056010 (2018) [arXiv:1807.03302].

BRST invariant RG flows

S. Asnafi[1,2,3]*, H. Gies*[2,3]*, and L. Zambelli*[3]

[1]Sharif U. & IPM, Tehran, Iran; [2]Helmholtz Institute Jena, Germany; [3]TPI, FSU Jena, Germany

Figure 1: Simplified diagrammatic representation of the flow equation truncated to linear source terms.

A mass parameter for the gauge bosons in gauge-fixed four-dimensional gauge theory can be accommodated in a local and manifestly BRST-invariant action. The construction is based on the Faddeev-Popov method involving a nonlinear gauge-fixing and a background Nakanishi-Lautrup field. When applied to momentum-dependent deformations, this formalism leads to a full regularization of the theory which explicitly preserves BRST symmetry. We deduce a functional renormalization group equation for the one-particle-irreducible effective action, which has a one-loop form. The master equation is compatible with it, i.e. BRST symmetry is preserved along the flow, and it has a standard regulator-independent Zinn-Justin form.

Gauge theories form the cornerstone of quantum interactions of all constituents of matter, with light-matter interactions representing the simplest and most directly accessible example. An adequate continuum description of such theories requires a careful treatment of local gauge symmetries, as a symmetry transformation can arbitrarily mix modes in momentum space. This seems naturally in conflict with regularizations that operate locally in momentum space. A elementary example is given by a mass term for the gauge boson which would provide for an IR regularization, but breaks gauge invariance.

In standard continuum formulations, quantization of gauge theories involves a gauge-fixing procedure in order to remove the large redundancy in the space of field configurations to be integrated over. This goes along with explicit symmetry-breaking terms. A major simplification arises from BRST symmetry, a remnant global supersymmetry that nonlinearly mixes gauge, Faddeev-Popov ghost and further auxiliary fields. BRST symmetry not only helps identifying the physical Hilbert space of states but also simplifies the constraint equation for correlation functions in the form of the Zinn-Justin master equation [1],

$$\Sigma \equiv \frac{\delta\Gamma}{\delta A_a^\mu}\frac{\delta\Gamma}{\delta K_\mu^a} + \frac{\delta\Gamma}{\delta c^a}\frac{\delta\Gamma}{\delta L^a} + v^a\frac{\delta\Gamma}{\delta\bar{c}^a} = 0. \quad (1)$$

At the expense of auxiliary sources, the Zinn-Justin equation relates correlation functions algebraically. Its resolution can be approached by algebraic cohomology methods and does not require the computation of loop terms.

For a scale-dependent RG description built on generic momentum-space regularization, the elegance (and practicality) of the master equation is no longer present, even though a high-energy constructions of complete models in a weak-coupling spirit are still possible [2]. In a recent work [3], we have suggested a novel approach for the construction of RG flows for gauge systems that relies on Faddeev-Popov quantization and aims at preserving exact BRST symmetry. The key idea is to treat the regularization as a contribution to the gauge fixing. As this is not possible within linear gauges, we consider a special choice of a nonlinear (quadratic) gauge condition. BRST symmetry in the standard fashion remains manifest at all stages of the construction. In order to obtain a conventional regulator term for the gauge field, we use a Fourier noise field for the Nakanishi-Lautrup auxiliary field. As a new ingredient, this gives rise to a background Nakanishi-Lautrup field.
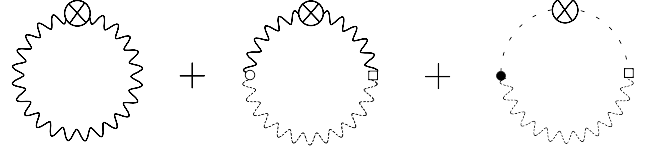
Also the ghost sector is at variance with that of standard linear gauges while preserving exact BRST invariance. In particular, new regulator-dependent vertices appear. Nevertheless, gauge invariance gives rise to a master equation for the effective action which can be brought to standard form with the aid of two additional source fields. This facilitates the resolution of the symmetry constraints by conventional algebraic cohomology methods. Most importantly, the resulting functional nonperturbative flow equation derived from the flow of the partition function $\partial_t Z = \mathcal{G}_t Z$ implies a flow for the effective action which has a one-loop structure, cf. Fig. 1. This is structurally analogous to the Wetterich equation [4], and thus our equation is amenable to widely used nonperturbative approximation schemes. Most importantly, the resulting Zinn-Justin equation, while receiving addition source terms, maintains the same algebraic structure as (1), and is consistent and preserved under the flow, $\partial_t \Sigma = \mathcal{G}_t \Sigma$. These results enable the construction of BRST invariant RG flows.

References

[1] J. Zinn-Justin, Lect. Notes Phys. **37**, 1 (1975).

[2] H. Gies, R. Sondenheimer, A. Ugolotti and L. Zambelli, Eur. Phys. J. C **79**, no. 2, 101 (2019).

[3] S. Asnafi, H. Gies and L. Zambelli, "BRST invariant RG flows," arXiv:1811.03615 [hep-th].

[4] C. Wetterich, Phys. Lett. B **301**, 90 (1993).

Trident pair production in plane waves:
Coherence, exchange, and spacetime inhomogeneity [*]

Victor Dinu[1] *and Greger Torgrimsson*[†2,3]

[1]Department of Physics, University of Bucharest; [2]Helmholtz Institute Jena, Germany; [3]TPI, FSU Jena, Germany

We have studied the trident process in inhomogeneous plane wave background fields [1]. We have obtained compact analytical expressions for all terms in the probability, including the exchange part, for an arbitrarily shaped plane wave. We have evaluated the probability numerically using complex deformation of lightfront time integrals and derived various analytical approximations. Our results provide insights into the importance of the one-step and exchange parts of the probability relative to the two-step process, and into the convergence to the locally constant field (LCF) approximation.

The trident process in electromagnetic background fields, $e^- \to 2e^- + e^+$, is a basic process in electron-laser collisions. It was first studied in detail in the 70's for constant crossed fields in [2, 3] before the advent of high-intensity lasers. Trident, or at least part of it, was explored in a famous experiment at SLAC [4] in the late 90's, with a laser of still modest intensity. At that time, complete theoretical predictions for trident were still lacking. Since then, the available laser intensities have increased by a couple of orders of magnitude, but on the theory side the situation has been improved thanks to only a few publications. The importance of trident in high-intensity laser processes therefore motivates further investigations.

One part of trident is a two-step process where the initial electron emits a real photon that subsequently decays into an electron-positron pair, i.e. nonlinear Compton scattering followed by nonlinear Breit-Wheeler pair production, and its contribution is given by incoherently gluing together the two corresponding rates, see e.g. [3, 5]. One of the main questions for trident is under what conditions this two-step process is a good approximation for the total trident process. The two-step process is expected to dominate for sufficiently large $a_0 = eE/(m\omega)$, where E is the field strength and ω the frequency of the field. This is important for particle-in-cell codes where higher-order processes, e.g. cascades, are described as a sequence of first-order processes. We have studied in more detail when corrections to the two-step process can be important.

The trident amplitude has two terms due to the exchange between the identical particles in the final state, and the absolute square of the amplitude gives a cross term which is referred to as the exchange part of the probability. The direct part is expected to dominate, e.g. for $\chi = a_0 b_0 \gg 1$, where $b_0 = kp/m^2$ is the product of a characteristic wave
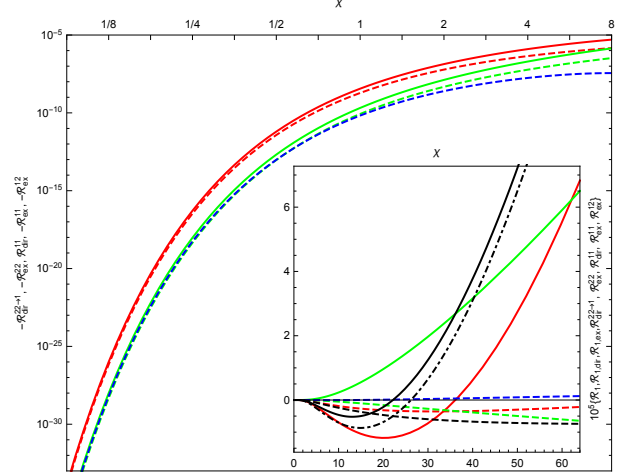
Figure 1: This figure shows the different terms contributing to the total one-step $\mathcal{R}_1$. The black solid curve shows the direct part $\mathcal{R}_{1,\mathrm{dir}}$, the black dashed curve shows the exchange term $\mathcal{R}_{1,\mathrm{ex}}$, and the black dot-dashed curve shows the total one-step $\mathcal{R}_1 = \mathcal{R}_{1,\mathrm{dir}} + \mathcal{R}_{1,\mathrm{ex}}$. Note that the exchange term is on the same order of magnitude as the direct part, even for quite large χ.

vector of the laser, k_μ, and the initial momentum of the incoming electron, p_μ. The exchange term can be difficult to calculate and it had not been obtained in the important LCF regime before. In [1] we calculated both the direct and the exchange parts in order to investigate in more detail when the latter can be important.

We have calculated the exchange term both analytically and numerically and found that it is in general as important as the direct part of the one-step term, as long as χ is not too large, see Fig. 1. We have also obtained simple analytical approximations that go beyond the LCF regime, i.e. for $a_0 \gtrsim 1$, and studied analytically and numerically the convergence to the LCF approximation as a_0 increases.

References

[1] V. Dinu and G. Torgrimsson, Phys. Rev. D **97**, no. 3, 036021 (2018)

[2] V. N. Baier, V. M. Katkov, and V. M. Strakhovenko, Sov. J. Nucl. Phys 14, 572 (1972).

[3] V. I. Ritus, Nucl. Phys. B **44** (1972) 236.

[4] C. Bamber *et al.*, Phys. Rev. D **60** (1999) 092004.

[5] B. King and H. Ruhl, Phys. Rev. D **88** (2013) 1, 013005

Spin-states in multiphoton pair production for circularly polarized light [*]

C. Kohlfürst[†][1,2]

[1]HI-Jena, Germany; [2]University of Jena, Germany

Electron-positron pair production through high-energy photons holds as one of the most promising effects in order to study quantum vacuum nonlinearities. In a proof-of-concept-experiment multiphoton pair creation has already been proven under laboratory conditions [1]. However, only due to the increased beam intensities upcoming laser facilities will provide, see ELI and XFEL, we will finally be able to answer the most burning questions regarding the vacuum itself.

We have devoted a recent work [2] to study the photo-electron angular distributions with respect to angular momentum transfer [3]. As it is the angular particle distribution that carries the information regarding the dynamics of the creation process, we could identify the individual contribution of each spin state.

In this work, we have investigated pair production within circularly polarized light. To mimic a standing wave formed by two counterpropagating laser beams we use a model of the form of

$$\mathbf{A}(t) = -\frac{\varepsilon m^2}{2e\omega} \exp\left(-\frac{t^2}{\tau^2}\right) \begin{pmatrix} \sin(\omega t) \\ \cos(\omega t) \\ 0 \end{pmatrix}, \qquad (1)$$

where ε is the peak field strength and ω determines the photon energy [4]. The parameter τ controls the pulse length, therefore it has to be sufficiently large in order to ensure a many-cycle pulse $\omega\tau \gg 1$. The Keldysh parameter is given by $\gamma = \omega/m\varepsilon > 1$. The electric field is derived from this vector potential.

Employing quantum kinetic theory (QKT) we can solve for the particle's distribution function $f(\mathbf{p})$ at a given momentum $\mathbf{p}$. In the multiphoton regime particles are created via the absorption of photons. In this regard, not only the photon energy but also its angular momentum is transfered to the newly formed electron-positron pair. Hence, within this absorption model we can expand any photo-electron wavefunction ψ in terms of spherical harmonics Y_l^m with the number of photons absorbed n as the limiting factor. Squaring the wavefunction then yields the particle's angular distribution

$$f(\vartheta, \varphi) \propto \psi^*\psi$$
$$= \sum_{l=0}^{n} \sum_{l'=0}^{n} \sum_{m=-l}^{l} \sum_{m'=-l'}^{l'} b_{l'm'}^* b_{lm} Y_{l'm'}^* Y_{lm}, \quad (2)$$
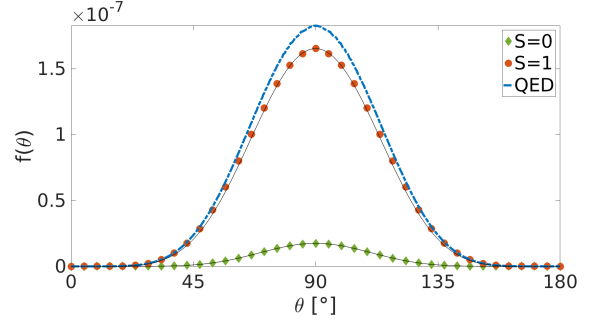
Figure 1: Photoelectron angular momentum $f(\theta)$ for a 4-photon pair production process. The total yield for electron-positron pair production (dashed blue curve) is given by the sum of a state with parallel spin alignment (orange circles) and a state of orthogonal alignment (green diamonds). Parameters: $\varepsilon = 0.075$, $\omega = 0.55m$ and $\tau = 250m^{-1}$. The black lines correspond to fits of the form of $\sin^{2(4-S)}(\theta)$.

with the coefficients b_{lm} and the angular momentum quantum numbers l and m. Rearranging the terms in eq. (2) cleverly and making use of the unique features of circularly polarized light the photoelectron angular momentum distribution can be brought into the remarkably simple form

$$f(\theta) = M_0 \sin^{2n}(\theta) + M_1 \sin^{2(n-1)}(\theta), \qquad (3)$$

where θ is defined as the angle between the fields' propagation direction and the particle's ejection direction.

Basically, in the scenario suggested above (1) all photons have helicity $+1$. Hence, in an n-photon process the pairs' total angular momentum has to be n. However, electrons and positrons are spin-$\frac{1}{2}$ particles, thus their combined spin can be 1 (if their spins align parallel) or 0 (if their spins align anti-parallel). As a result the electrons' angular distribution function can be decomposed into a parallel and an anti-parallel contribution. In Fig. 1 we have illustrated this relation for a 4-photon scenario, where the field's peak strength was $\varepsilon = 0.075$ and its frequency $\omega = 0.55m$.

References

[1] D. L. Burke (SLAC) *et al.*, Phys. Rev. Lett. **79**, 1626 (1997).

[2] C. Kohlfürst, arXiv:1812.03130 [hep-ph].

[3] K. L. Reid, Annu. Rev. Phys. Chem. 2003. 54:397-424.

[4] A. Blinne and H. Gies, Phys. Rev. D **89** (2014), 085001.

Strong-field approximation for spatially structured laser fields[*]

B. Böning[†1,2], *W. Paufler*[1,2], *and S. Fritzsche*[1,2]

[1]Helmholtz-Institut Jena, Germany; [2]Friedrich-Schiller-Universität Jena, Germany

The strong-field approximation (SFA) is widely used to theoretically describe atomic and molecular processes driven by intense laser fields. Of particular interest are the above-threshold ionization (ATI) and high-harmonic generation (HHG). In the former, the target is ionized and the photoelectron absorbs more photons than needed to overcome the threshold. This leads to distinct peaks in the photoelectron energy spectrum which are spaced by the photon energy. In HHG, the photoelectron accelerates in the laser field, recombines with the parent ion and thereby emits a high energetic photon. This provides, for example, table-top sources of ultrashort XUV pulses.

In recent years, developments in laser sources have lead to strong-field experiments in which the spatial dependence of the driving field becomes relevant. First, if an atomic target is ionized by a strong mid-infrared laser pulse, the photoelectron acquires a non-vanishing momentum along the laser propagation direction [1]. This momentum component was termed *peak offset* Δp_z. Second, if the driving laser pulse carries orbital angular momentum (OAM) in addition to the photon's spin angular momentum, HHG leads to the creation of XUV pulses which also carry OAM [2], due to angular momentum conservation. In order to better understand such scenarios involving the transfer of longitudinal and orbital angular momentum to the electron, we developed a nondipole extension of the SFA for laser fields $\mathbf{A}(\mathbf{r}, t)$ with *arbitrary* spatial dependence.

The laser-electron interaction is included in the SFA via nonrelativistic Volkov states, which are usually given only in dipole approximation. We showed that, when nondipole effects are present, these solutions take the form [3]

$$\psi_{\mathbf{p}}(\mathbf{r}, t) = \frac{1}{(2\pi)^{3/2}} e^{-i(E_{\mathbf{p}}t - \mathbf{p}\mathbf{r})} e^{-i\Gamma(\mathbf{r}, t)},$$

where the usual dipole Volkov phase $S_V(t)$ is replaced by a modified Volkov phase $\Gamma(\mathbf{r}, t)$. We included these nondipole Volkov states in the SFA computation of photoelectron momentum distributions in ATI and calculated the peak offsets Δp_z shown in Fig. 1 for different laser wavelength and atomic targets. These theoretical values agree well with the experiment [1]. Only a small discrepancy remains since we neglected focal averaging. This could, however, be included in the above nondipole Volkov states. We further derived the explicit dependence $\Delta p_z \sim I\lambda^2$ with the laser wavelength λ and intensity I from the SFA.
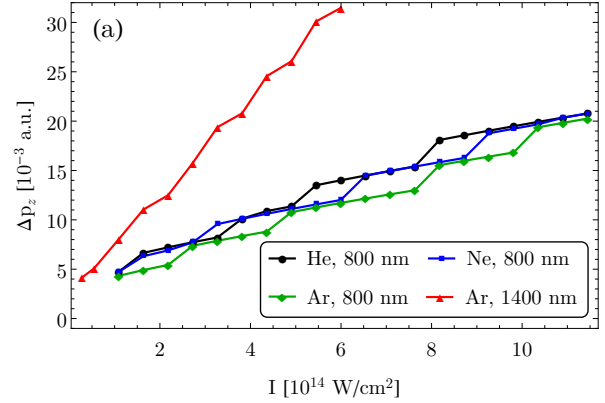
Figure 1: Peak offsets Δp_z of ATI photoelectron momentum distributions as a function of laser intensity I. Results are shown for a circularly polarized plane-wave laser beam and for different atomic targets and laser wavelengths. The parameters are chosen so that results are comparable with the experimental values published in [1].

Since the peak offset vanishes in dipole approximation, this formula stresses the importance of nondipole contributions in strong-field processes driven by long wavelengths, e.g. in the mid-infrared.

Currently, we apply the nondipole SFA discussed here to strong-field processes driven by twisted laser fields carrying OAM. There we will analyze in detail the angular momentum transfer between laser field and photoelectron and its effect on photoelectron momentum distributions. Already in the dipole approximation, our SFA-based study of ATI driven by twisted laser fields showed significant differences to plane-wave laser fields [4]. Furthermore, the nondipole SFA might be used to describe HHG. This new formalism allows an insightful theoretical investigation of these phenomena, especially regaring the role of OAM in the strong field laser-electron interaction.

References

[1] C. T. L. Smeenk *et al.* , *Phys. Rev. Lett.* **106** 193002 (2011)

[2] W. Paufler *et al.* , *Phys. Rev. A* **98** 011401(R) (2018)

[3] B. Böning *et al.* , *Phys. Rev. A*, submitted (2019)

[4] B. Böning *et al.* , *Phys. Rev. A* **98** 023407 (2018)

Tailored orbital angular momentum in high-order harmonic generation with bicircular Laguerre-Gaussian beams [*]

W. Paufler[†][1,2,3], *B. Böning*[1,2,3], *and S. Fritzsche*[1,2,3]

[1]Helmhotz Institut, Jena, Germany; [2]GSI Helmholtzzentrum für Schwerionenforschung GmbH, Darmstadt, Germany; [3]Theoretisch-Physikalisches Institut, Friedrich-Schiller Universität, Jena, Germany

Allen et al. demonstrated that light beams can carry, in addition to their spin angular momentum (SAM), a well-defined orbital angular momentum (OAM) ℓ [1]. Laguerre-Gaussian (LG) modes are the most common light beams with such a property. The OAM induces an azimuthal phase dependence $e^{i\ell\phi}$ that gives rise to helical phase fronts. During the last years the generation of extreme ultraviolet (XUV) vortices through high harmonic generation became an attractive field of research. Recent theoretical and experimental investigations of high harmonic generation (HHG) with linearly polarized LG modes showed that the OAM of a qth harmonic order equals $q\ell$, where ℓ is the OAM of the incident mode [2].

Here we proposed a novel scheme to create XUV vortices that uses a superposition of a right circularly polarized LG mode with frequency ω and its counter rotating second harmonic, which is known as a bicircular field. HHG with such fields produces alternately a right and a lefty circularly polarized harmonic, whereas every third harmonic is suppressed, because of conservation of SAM. This is in contrast to HHG with linearly polarized fields, where every generated harmonic has a linear polarization and all even harmonics are suppressed.

We theoretically showed that HHG with bicircular Laguerre-Gaussian beams obeys the following selection rules:

$$LG_{\ell_1,0}^{\omega\,\circlearrowleft} \oplus LG_{\ell_2,0}^{2\omega\,\circlearrowright} \xrightarrow{HHG} \begin{array}{c} \omega_{H_q} = q\omega = m\omega + n\,2\omega, \\ m - n = \pm 1, \\ \ell_{H_q} = m\,\ell_1 + n\,\ell_2. \end{array}$$

Here ℓ_1 and ℓ_2 are the OAM and m and n are the number of photons absorbed from the right and left circularly polarized Laguerre-Gaussian beam respectively. The energy of a harmonic $\omega_{H_q} = q\omega$ is then given by the total energy of all absorbed photons. Since the SAM of the emitted photon has to be ± 1 the electron absorbs one more photon from the right circularly polarized beam than from the left one or vice versa. This restriction, $m - n = \pm 1$, allows for each harmonic that will be generated only one combination of photons with frequency ω and 2ω and determines therefore the polarization of the emitted harmonic. The OAM of the emitted harmonic is given by $\ell_{H_q} = m\,\ell_1 + n\,\ell_2$ due to conservation of OAM. Again, the restriction that $m - n = \pm 1$ ensures that the generated harmonic is a pure LG mode with a well-defined ℓ_{H_q}. Our calculations show

that the OAM of each harmonic can be directly controlled by the OAM of the incident LG modes. Furthermore, we showed how the OAM of the incoming LG modes have to be chosen in order to generate every possible value of OAM in the emitted harmonics. For a given harmonic order q and OAM ℓ_{H_q} the OAM of the incident beams are given by

$$\ell_1 = \pm\ell_{H_q} + an \quad \text{and} \quad \ell_2 = \mp\ell_{H_q} - am,$$

if $m - n = \pm 1$. Here a is an arbitrary integer, which gives rise to different solutions the OAM of the incident beams. In this contribution, moreover, we generalized the $LG_{\ell_1,0}^{\omega\,\circlearrowleft} \oplus LG_{\ell_2,0}^{2\omega\,\circlearrowright}$ superposition to a $LG_{\ell_1,0}^{r\omega\,\circlearrowleft} \oplus LG_{\ell_2,0}^{s\omega\,\circlearrowright}$ superposition [3]. In addition, we analyzed the emitted harmonics with respect to their divergence and found that the divergence decreases with the harmonic order and increases with the OAM of the emitted harmonic. Recently this has been used to spatially separate left and right circularly polarized XUV vortices. Here, circularly XUV attosecond pulses have been generated and measured [4].
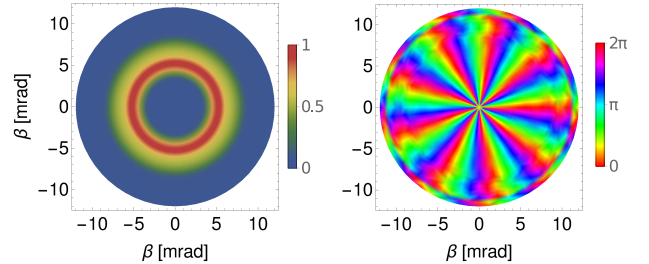
Figure 1: Results obtained for the 13th harmonic. Left: Intensity profile shows the characteristic ring structure of twisted light. On the propagation axis the intensity is zero. Right: Phase profile shows that the OAM of the 13th harmonic is $\ell = 9$.

Despite the circular polarization of each harmonic, in general, the resulting attosecond pulses are linearly polarized, since neighboring harmonics overlap. Thus it would be interesting to see if it is possible to suppress the left or right circularly polarized harmonics in order to achieve circularly polarized XUV attosecond pulses with OAM.

References

[1] Allen L *et al.* 1992 *Phys. Rev. A* **45** 8185

[2] Gariepy G *et al.* 2014 *Phys. Rev. Lett.* **113** 153901

[3] Paufler W *et al.* 2018 *Phys. Rev. A* **98** 011401

[4] Dorney K *et al.* 2018 *Nat. Phot.* **10** 123-130

[†] willi.paufler@uni-jena.de

Polarization of fluorescence light as a precise tool for understanding multiphoton photoionization

J. Hofbrucker [1,2,3], A. V. Volotka[1,2], and S. Fritzsche[1,2,3]

[1] GSI, Darmstadt, Germany; [2] Helmholtz-Institut Jena, Germany; [3] Friedrich-Schiller-Universität Jena, Germany

The advances and increasing number of free-electron lasers (FELs) revolutionized the exploration of inner-shell electron dynamics and nonlinear light-matter interaction by delivering intense extreme-ultraviolet and x-ray beams. However, the accuracy of the extracted cross sections is bound by the systematic uncertainty in the beam parameters which determine the absolute intensity. This causes large experimental uncertainties which in return do not allow to resolve differences between various theoretical approaches [1].

We suggest an alternative measurable quantity which depends less on the beam properties and promises highly accurate comparison of experiment with theory. We consider the production of an oriented ion produced by multi-photon inner-shell ionization of a *p*-electron of neutral atom by circularly polarized light. Since such an ion will be in an excited state, it will relax by a radiative decay to a ground state. We show that by measuring the polarization properties of the subsequent fluorescent light, high accuracy measurements can be carried out at specific incident photon energies. These specific energy points, *nonlinear Cooper minima*, are characterized by zero contribution of the otherwise dominant ionization channel. The zero contribution of the channel originates from fine cancellation of all possible intermediate ionization paths. Due to the ionizing circularly polarized light and vanishing of the otherwise dominant ionization channel, the produced ion is in a fully polarized state with completely depleted population of electron with magnetic projection $m=\pm1$ (the sign depends on the handedness of incident light). As a consequence, the electron in a higher shell is forced to a transition to this pure vacancy, emitting a fluorescence photon which will also be fully polarized. The polarization of fluorescence photons of course depends on their emission direction. We demonstrate that they will be fully polarized independent of the emission angle and that the fluorescence photons will be purely circularly polarized along the propagation direction of the incident beam, while perpendicular to this direction, they will be purely linearly polarized. The figure below shows the calculated results of two-photon ionization of the *p*-electron of magnesium atom by right-circularly polarized light. Total cross section (dot-dashed) and degree of circular and linear polarization of the emitted fluorescence photon P_3 ($\theta=0°$) (full) and $P_1(\theta=90°)$(dashed) are shown as functions of incident photon energy.

Theoretical energy position predictions of nonlinear Cooper minima require accurate treatment of the complete atomic spectrum. Hence, experimental measurements of the nonlinear Cooper minima will allow for comparison of experimental measurements with theory at hitherto unreachable precision. Detection of fluorescence light as a characteristic of multiphoton ionization is a well established method, and therefore, measurements of these properties at the nonlinear Cooper minimum could readily find applications beyond fundamental importance, as it could also serve for applied fields such as spectroscopy of atoms and molecules [2].

References

[1] S. Ghimire et al, Phys. Rev. A **94,** 043418. (2016)

[2] Hofbrucker, A. V. Volotka, and S. Fritzsche, Phys. Rev. Lett. **121**, 053401 (2018).

Figure 1: Two-photon ionization of the *p*-electron of magnesium atom. Total cross section (dot-dashed) and degree of circular and linear polarization of the emitted fluorescence photon $P_3(\theta= 0°)$(full) and $P_1(\theta=90°)$(dashed) as functions of incident photon energy.
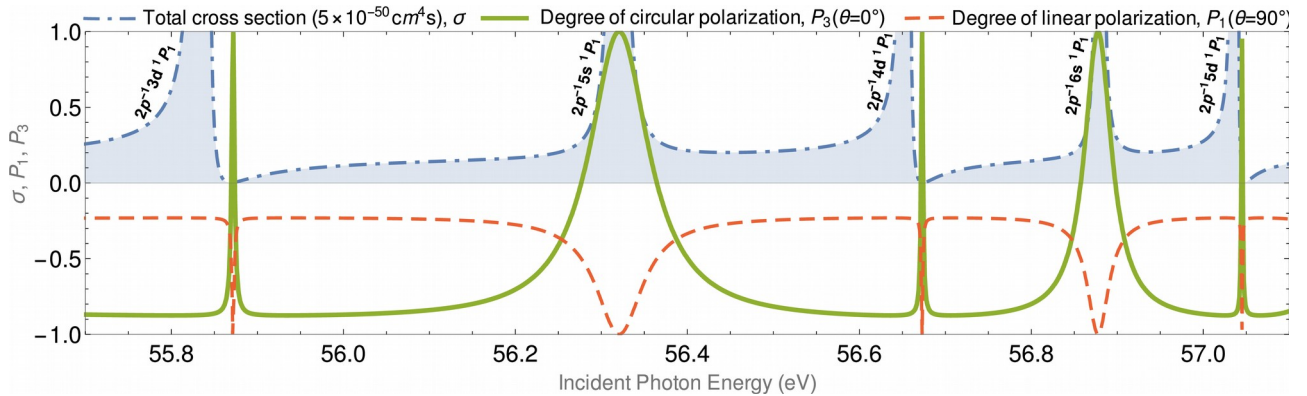
Near L-Edge Photoionization of Triply Charged Iron Ions [*]

R. Beerwerth[†][1,2], S. Schippers[3], and S. Fritzsche[1,2]

[1]Helmholtz Institute Jena, Jena, Germany; [2]Theoretisch-Physikalisches Institut, Universität Jena, 07743 Jena, Germany;
[3]I. Physikalisches Institut, Justus-Liebig-Universität Gießen, 35392 Gießen, Germany

The absorption spectra of atoms and ions are crucial for the spectroscopic analysis of various sources of light such as in astronomy for the determination of abundances of elements or plasma models. At the same time, the absorption of high energy photons leads to the creation of inner shell holes, that decay preferably by Auger processes. In the Auger process an inner shell hole is filled and the excess energy is emitted as kinetic energy of another electron leaving the ion in a final state with one less electron. This final state can still lie above the ionization threshold for the next higher charge state, enabling another (or more) subsequent Auger decays [1]. This leads to a distribution of final charge states which is another important input into e.g. plasma models or the understanding of electronic structure. Due to the large cost of experiments, it is impossible to fulfill this need for atomic data by purely experimental data and theoretical models are needed to fill the gap. However, many-electron atoms with multiple open shells are still a formidable challenge for theory and approximations need to be tested and improved.

In a joint theoretical and experimental work, we performed computations of the absorption cross section of Fe^{3+} in the range of $680 - 1100\,eV$ that covers both the $2p$ and $2s$ ionization thresholds. In addition, complex cascade computations were carried out to model the final charge state distribution of the resulting Fe ions. Both quantities were also obtained experimentally at the PIPE setup at PETRA III by measuring the absolute cross sections for up to five-fold ionization, which is a continuation of our earlier work on Fe^{1+} [2]. The computed as well as the measured absorption cross section is shown in Fig. 1 around the $2p$ edge where several $2p^6 3d^5 \rightarrow 2p^6 \left(3d^6 + 3d^5 nd\right)$ resonances are visible. In contrast, the contribution of resonant $2p \rightarrow 4s$ excitations into the $2p^5 3d^5 4s$ configuration was found to be negligible.

Additionally, we performed extensive calculations of the Auger cascades that emerge when an electron is removed from the $2p$ and $2s$ shells of Fe^{3+}. To model the complete de-excitation pathways by sequential Auger decays, we include all electronic configurations that arise due to Auger decay processes from the core hole excited $2p^5 3d^6$ configuration, giving rise to several thousand fine structure levels for the intermediate charge states and hence millions of Auger transitions. In order to keep the calculations of the Auger transition rates feasible, it was necessary to constrain the size of the Auger matrices, therefore, all wave functions were computed in single configuration approximation utilizing the GRASP2K code [3]. The Auger transi-
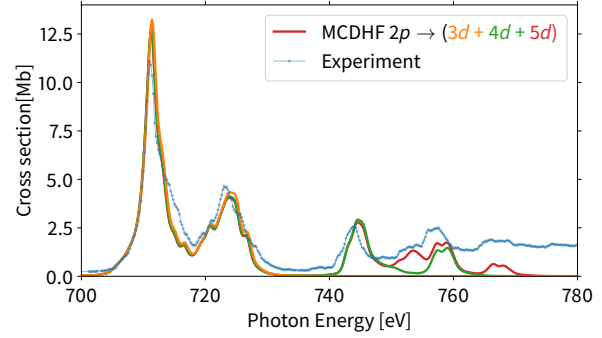
Figure 1: Computed absorption cross section and experimental relative cross section, including $2p \rightarrow nd$ resonances. Computed values are convoluted with a Voigt profile with Gaussian FWHM $= 1.0$ eV as well as $\Gamma = 0.4$ eV. The computed MCDHF energies have been shifted by -2.2 eV.

tion rates are computed with the RATIP code [4].

When direct double Auger processes as well as shake-up transitions are neglected, only the production of ions up to Fe^{6+} is energetically possible since the populated levels with the highest energy in the cascade pathways belong to the $3s^{-2}$ configuration in Fe^{4+}. In the higher product charge states, there are several inner-shell hole configurations that, for energetic reasons, are (partially) forbidden to decay via two-electron Auger processes. For example, the high lying fine structure levels of the $3p^4 3d^6$ configuration can decay by a two-electron Auger process to $3p^5 3d^4$, while this decay path is forbidden for the low-lying levels. However, these levels are still above the ionization threshold. They can instead decay by a three-electron Auger decay where a third electron undergoes a $3d \rightarrow 3p$ shake down transition and thereby reach the $3d^3$ ground configuration of Fe^{5+}. In general, such multi-electron processes are expected to be slow compared to a two-electron Auger process. Nevertheless, they can still be faster than the competing radiative processes that would result in Fe^{4+} product ions.

Our theoretically predicted charge-state fractions are in very good agreement with the experimental result and substantially improve previous theoretical predictions due to the more detailed treatment at fine structure level and the inclusion of some shake down processes.

References

[1] R. Beerwerth et al., The Europ. Phys. J. D, 71 (2017), 253
[2] S. Schippers et al., The Astroph. J. 849:5 (2017)
[3] P. Jönsson et al., Comput. Phys. Commun. 184 (2013), 2197
[4] S. Fritzsche, Comput. Phys. Commun. 183 (2012), 1525

Line strength calculations of the $1s^2 2s 2p\,^1P_1 - 1s^2 2s^2\,^1S_0$ spin allowed *E1* transition in Be-like carbon

M. Bilal[1,2], A. V. Volotka[2], R. Beerwerth[1,2], J. Rothhardt[2,3,4], V. Hilbert[2,4], S. Fritzsche[1,2]

[1]TPI Jena, Germany; [2]HI Jena, Germany; [3]IOF Jena, Germany; [4]IAP Jena, Germany

Our understanding of the structure and dynamics of many-electron atoms and ions depends on a detailed analysis and comparison of theoretical predictions with experimental observations of atomic properties. Two important and complementary properties of atomic states are transition energies and transition rates. For transition energies, the present experimental accuracy reaches the order of 10^{-18}. For transition rates of many-electrons atoms and ions, in contrast, most of the experiments provide uncertainties in the region of $30 - 1\%$. Whereas only few experiments provide the uncertainty in the region $1 - 0.1\%$. In this context, high hopes are pinned on the femtosecond laser technology [1] which has already demonstrated a great success in studies of chemical reactions, wave function dynamics, photoionization time delays, etc. Recently, it has been also proposed to use a compact high-power XUV-ray source in a combination with the storage ring at GSI to perform precision spectroscopy and lifetime measurements of the $1s^2 2s 2p\,^1P_1$ state in Be-like carbon [2]. In principle, the relative accuracy could reach the order $10^{-4} - 10^{-5}$. The excited state $1s^2 2s 2p\,^1P_1$ decays to the $1s^2 2s^2\,^1S_0$ ground state through a strong spin allowed *E1* transition.

Here, we present a detailed calculation of the line strength of the $1s^2 2s 2p\,^1P_1 - 1s^2 2s^2\,^1S_0$ transition in Be-like carbon in the prospect of high precision experiment. We develop various electron correlation models and use orthogonal and nonorthogonal set of orbitals for the initial and final states in these correlation models by employing multiconfiguration Dirac-Hartree-Fock method [3].
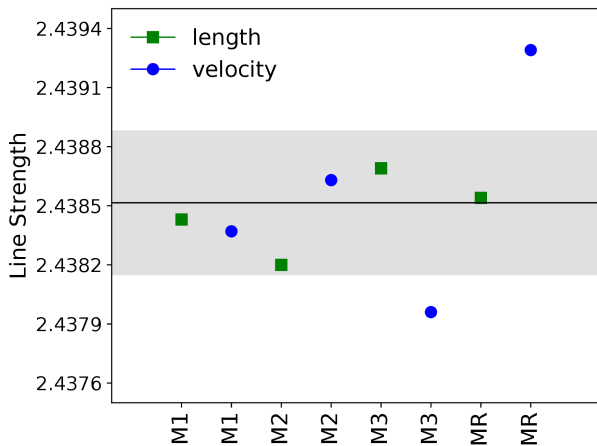
Figure 1: Line strength of the $1s^2 2s 2p\,^1P_1 - 1s^2 2s^2\,^1S_0$ transition in Be-like carbon plotted against the present Models. Green squares represent to the length forms and blue circles to the velocity forms. The black solid line is the average of the both length and velocity forms. The grey shaded region is one standard deviation from the black line.

It is found, that the accuracy assessment based on an agreement between the gauges might lead to a significant error underestimation. For this reason, we estimate the uncertainty from the differences between the results obtained within all the correlation models developed, namely M1, M2, M3 and MR as shown in Fig. 1. These models account the correlations with various sets of the initial and the final state wave functions [4]. In addition, the finite nuclear mass effect to the line strength is evaluated and its gauge invariance is demonstrated after taking into account the recoil correction to the transition operator. As a result, the calculated line strength amounts to
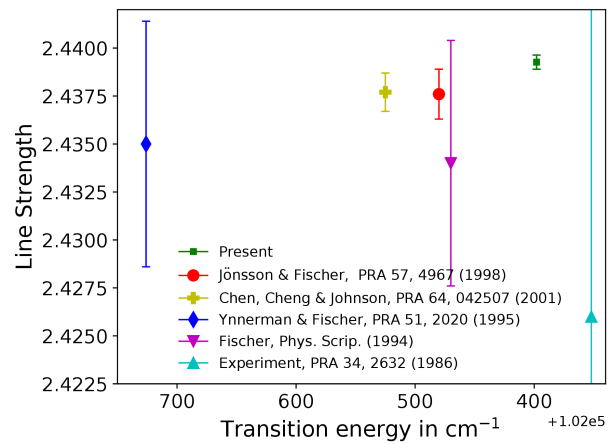
Figure 2: A comparison of the present line strength of the $1s^2 2s 2p\,^1P_1 - 1s^2 2s^2\,^1S_0$ transition in Be-like carbon with other theories and experiment.

$2.43926(37)$ with the relative accuracy 1.5×10^{-4} [4].

The achieved relative uncertainty of the line strength represents a reliable theoretical benchmark of *E1* line strength in a view of upcoming high precision lifetime measurement of the $1s^2 2s 2p\,^1P_1$ state of Be-like carbon (see Fig. 2).

Extensions of current studies to heavier Be-like ions allow us to improve the theoretical accuracy of transition rates. The given (numerical) uncertainty together with the high precision experiments will allow an alternative spectroscopic test than the energy alone and will provide further insight into the atomic structure of many- electrons atoms and ions [4].

References

[1] A. H. Zewail, The Journal of Physical Chemistry A, 104 (2000) 5660.

[2] J. Rothhardt et al., X-Ray Spectrometry (In Press 2019).

[3] P. Jönsson et al., Comput. Phys. Commun. 184 (2013) 2197.

[4] M. Bilal et al., submitted to Phys. Rev. A (2019).

Isotope shift parameters for the $5s_{1/2}$–$5p_{1/2}$ transition in doubly-charged yttrium[*]

S. O. Stock[1,2], R. Beerwerth[1,2], and S. Fritzsche[1,2]

[1]Helmholtz Institute Jena, Germany; [2]Theoretisch-Physikalisches Institut, Friedrich-Schiller-Universität Jena, Germany

The investigation of isotope shifts is an important instrument in nuclear structure research since it links nuclear properties like the mean-square charge radius to atomic transition energies which can be studied with high-resolution spectroscopy. For a specific atomic transition, the isotope shift $\delta\nu^{A,A'}$ between two isotopes A and A' is usually parametrized using two parameters M and F, which relate to the mass and field shift, respectively:

$$\delta\nu^{A,A'} = M\frac{m_{A'} - m_A}{m_{A'}m_A} + F\,\delta\langle r^2\rangle^{A,A'}$$

Here, the mass shift parameter M quantifies the recoil effects due to the different nuclear masses m_A and $m_{A'}$, and the field shift parameter F relates to the energy shift due to the difference in the nuclear potentials generated by nuclei with different charge distributions. Here, $\delta\langle r^2\rangle^{A,A'}$ is the difference in mean-square charge radii between the isotopes. The parameters M and F depend on the specific atomic transition and can often only be obtained by means of atomic structure calculations or semiempirical estimates.

Here, we present our theoretical calculations in support of an experiment which studied isotope shifts in short-lived yttrium isotopes using collinear laser spectroscopy [1]. In order to determine the isotope shift parameters M and F for the $5s_{1/2}$–$5p_{1/2}$ transition in Y^{2+}, we performed large-scale multiconfiguration Dirac–Hartree–Fock (MCDHF) calculations. The atomic wave functions were created using the GRASP2K atomic structure package [2]. In order to get an accurate wave function representation, we generated a set of systematically enlarged multiconfiguration bases by including virtual excitations from a set of reference configurations to at most seven layers of correlation orbitals.

First, a zero order set of 578 relativistic configuration state functions (CSFs) for the $5s_{1/2}$, $5p_{1/2}$, and $5p_{3/2}$ states was created, including higher-excited configurations of the same symmetry. From this large CSF set, a small subset was extracted by only selecting CSFs with at least a 0.001 share of the $5s_{1/2}$ or $5p_{1/2}$ level. This resulted in a set of 18 CSFs which were used as the reference to generate the systematically enlarged bases by including single and double excitations from the $4p$, $4d$, $5s$, and $5p$ orbitals into correlation orbitals $n\ell$ with $\ell \leq g$ as well as into the zero order set. The correlation layers only include CSFs which couple to at least one of the 18 reference CSFs via the Dirac–Coulomb Hamiltonian. With all seven correlation layers, the basis set consisted of 600 656 CSFs.

Table 1: Calculated transition energies ΔE and isotope shift parameters M and F for each number of layers of the computation. The mass shift parameter M is the sum of the normal (NMS) and specific mass shift (SMS).

| Layer | ΔE [cm^{-1}] | M [GHz u] | | F [MHz fm^{-2}] |
		NMS	SMS	
0	33 383	998	−958	−1925
1	33 735	363	−235	−1953
2	33 863	481	−325	−1951
3	33 851	443	−333	−1964
4	33 853	470	−352	−1960
5	33 851	467	−345	−1964
6	33 850	475	−346	−1962
7	33 850	477	−347	−1964

Based on the generated MCDHF wave functions, the mass shift parameter M was obtained by calculating the expectation values of the nuclear recoil operator using the RIS3 program [3]. In order to obtain the field shift parameter F, the $5s_{1/2}$–$5p_{1/2}$ transition energy was calculated for different model nuclei ($A = 89, 91, 93, 96, 98$). Each nucleus is modeled as a Fermi-distributed charge density

$$\rho(r) = \frac{\rho_0}{1 + \exp((r - c)/a)}$$

where c is related to the radius of the nuclear charge density and a to the nuclear skin thickness.

The calculated transition energies and isotope shift parameters are shown in Table 1 for each number of correlation layers. Adding correlation layers leads to a convergence of the isotope shift parameters to the values

$$M = 130\,\text{GHz u} \quad\text{and}\quad F = -1964\,\text{MHz fm}^{-2}.$$

The calculated transition energy of $33\,850\,\text{cm}^{-1}$ is in good agreement with the experimental value of $33\,934\,\text{cm}^{-1}$.

References

[1] L. J. Vormawah et al., "Isotope shifts from collinear laser spectroscopy of doubly charged yttrium isotopes", Physical Review A **97**, 042504 (2018).

[2] P. Jönsson et al.,"New version: GRASP2K relativistic atomic structure package", Computer Physics Communications **184**, 2197 (2013).

[3] C. Nazé et al.,"RIS3: A program for relativistic isotope shift calculations", Computer Physics Communications **184**, 2187 (2013).

Interelectronic-interaction corrections to hyperfine splitting in Li-like ions

V. P. Kosheleva[1,2,3], *A. V. Volotka*[1,2], *D. A. Glazov*[3], *and S. Fritzsche*[1,2,4]

[1]Helmholtz Institute Jena, 07743 Jena, Germany; [2]GSI Helmholtzzentrum für Schwerionenforschung GmbH, 64291 Darmstadt, Germany; [3]Department of Physics, St. Petersburg State University, 199034 St. Petersburg, Russia; [4]Theoretisch-Physicalisches Institut, Friedrich-Schiller-Universität, 07743 Jena, Germany

Investigation of the hyperfine structure (hfs) in highly-charged ions provides a unique possibility to test QED in strongest electric and magnetic fields. Recent theoretical studies are motivated by experimental breakthrough in measuring hfs in H-like ions which nowadays reached the accuracy of less than 0.002% [1, 2]. It should be noted here that the correction to the hfs due to the spatial distribution of the nuclear magnetization (so-called Bohr-Weisskopf effect) masks radiative corrections. This in turn was the reason for studies of hfs in both H-like and Li-like ions with the same nucleus allowing to cancel the Bohr-Weisskopf correction using the concept of specific difference [3]. Since the specific difference is mainly determined by screened radiative and interelectronic-interaction effects the accurate theoretical evaluation of these corrections is demanded. We report on the complete evaluation of the two-photon exchange corrections to the hfs in Li-like ions in the framework of rigorous QED approach within the extended Furry picture. These interelectronic-interaction effects have been already studied in Ref. [4] in the standard Furry picture. In the framework of extended Furry picture the interelectronic interaction is partly taken into account already in the zeroth order. Hence, in contrast to the standard Furry picture, the valence-electron wave function obey the Dirac equation with the effective potential $V_{\text{eff}}(\mathbf{r})$:

$$V_{\text{eff}}(\mathbf{r}) = V_{\text{nucl}}(\mathbf{r}) + V_{\text{scr}}(\mathbf{r}), \qquad (1)$$

where $V_{\text{nucl}}(\mathbf{r})$ is the potential of the nucleus and $V_{\text{scr}}(\mathbf{r})$ is some local screening potential induced by the electrons of the closed shell(s). Such approach can accelerate the convergence of perturbation expansion. In the present work we used 3 starting potentials: Coulomb (no screening), core-Hartree, and Kohn-Sham. The total theoretical value of the hyperfine splitting can be written as follows:

$$\Delta E_{\text{hfs}} = E_F G_a(Z)(1 - \delta_{\text{BW}}), \qquad (2)$$

where δ_{BW} is the hfs correction due to the Bohr-Weisskopf effect, a denotes the valence electron. $G_a(Z)$ is a dimensionless function expressed within the perturbation theory as

$$G_a(Z) = G_a^{(0)}(Z) + G_a^{(1)}(Z) \\ + G_a^{(2)}(Z) + G_a^{(3+)}(Z). \qquad (3)$$

The terms in Eq. (3) refer to the interelectronic-interaction corrections of the first $[G_a^{(1)}(Z)]$, second $[G_a^{(2)}(Z)]$, and higher $[G_a(Z)^{(3+)}]$ orders. The one- and two-photon-exchange corrections were treated in the framework of rigorous QED approach. The higher-order corrections were
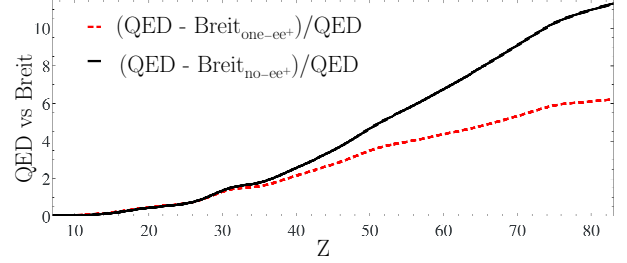
Figure 1: Comparison of the two-photon-exchange correction $G_a^{(2)}(Z)$ to the ground-state hfs in Li-like ions obtained with the Konh-Sham potential within the rigorous QED treatment and within the Breit approach (no-pair ($\text{Breit}_{\text{no}-\text{ee}+}$) and one-pair ($\text{Breit}_{\text{one}-\text{ee}+}$) approximations). The solid (black) and dashed (red) lines correspond to the deviation of the indicated Breit approximations from the QED approach.

obtained within the Breit approximation by means of the recursive perturbation theory [5].

Now let us compare the results of the rigorous QED treatment of the two-photon-exchange correction $G_a^{(2)}(Z)$ with the results obtained in the Breit approach in no-pair ($\text{Breit}_{\text{no}-\text{ee}+}$) and one virtual-pair ($\text{Breit}_{\text{one}-\text{ee}+}$) approximations. In Fig. 1 one can see the deviation of $\text{Breit}_{\text{no}-\text{ee}+}$ (solid black line) and $\text{Breit}_{\text{one}-\text{ee}+}$ (dashed red line) approaches from the QED treatment of the two-photon-exchange correction $G_a^{(2)}(Z)$ for a wide range of the nuclear charge number Z.

From Fig. 1 it is seen that for small Z (≤ 10) the deviation between QED approach and Breit approximations ($\text{Breit}_{\text{no}-\text{ee}+}$/$\text{Breit}_{\text{one}-\text{ee}+}$) is less than 1% and with the growth of Z it becomes more pronounced. So, for bismuth ($Z = 83$) the difference between the rigorous QED treatment and $\text{Breit}_{\text{one}-\text{ee}+}$ approximation is about 5%, while the QED–$\text{Breit}_{\text{no}-\text{ee}+}$ difference is more than 11%. This firmly confirms the importance of the QED treatment of the interelectronic interaction.

References

[1] J. Ullmann *et al.*, J. Phys. B **48**, 144022 (2015).

[2] J. Ullmann *et al.*, Nat. Commun. **8**, 15484 (2017).

[3] V. M. Shabaev *et al.*, Phys. Rev. Lett. **86**, 3959 (2001).

[4] A. V. Volotka *et al.*, Phys. Rev. Lett. **108**, 073001 (2012).

[5] D. A. Glazov *et al.*, Nucl. Instrum. Methods Phys. Res. B **408**, 46 (2017).

One-dimensional quantum walks driven by two entangled coins

S. Panahiyan[*1,2] *and S. Fritzsche*[†1,2]

[1]Helmholtz-Institut Jena, Jena, Germany; [2]GSI Helmholtzzentrum für Schwerionenforschung, Darmstadt, Germany

We study a one-dimensional quantum walk with four internal degrees of freedom (two entangled qubits) driven by two entangled coins. We demonstrate that the entanglement, introduced by the coins, enables one to steer the walker's state from a classical behaviour to novel one not found for one-dimensional walks otherwise. We show that states with a symmetric density distribution and a maximum of the entropy are found only for maximally entangled initial states. On the other hand, the type of probability density distribution (PDD) and its variance are only determined by entangled coins.

Quantum walk with two entangled coins

Quantum walk (QW) has been found an efficient framework to develop new (quantum) algorithms [1], simulate other quantum systems [2], explore topological phases, build neural networks and engineer quantum states. QW is known also as universal computational primitives [3]. Experimentally, QW has been realized with photons and ions [4, 5]. Entanglement is a resource of quantum systems with no classical counterpart [6]. This resource plays a crucial role in applications of quantum information such as superdense coding, teleportation, quantum computation and algorithmic construction. Naturally, it is also possible to use the entanglement as a resource in QWs. Here, we consider a single walker with four internal degrees of freedom (due to two entangled qubits) in one-dimensional position space.

Setup of the walk and results

The walker is a quantum system that moves stepwise in position space due to its four internal degrees of freedom represented by two entangled qubits. The Hilbert space of internal degrees of freedom, $\mathcal{H}_C$, is spanned by $\{|00\rangle, |11\rangle, |10\rangle, |01\rangle\}$. The coin operator of the walk is given by tensor product of two single-qubit coin operators, $\widehat{C} = \widehat{C'} \otimes \widehat{C'}$ where

$$
\begin{aligned}
\widehat{C'} = &\cos\theta \, |0\rangle_C \langle 0| + \sin\theta \, |0\rangle_C \langle 1| \\
&+ \sin\theta \, |1\rangle_C \langle 0| - \cos\theta \, |1\rangle_C \langle 1| , \quad (1)
\end{aligned}
$$

The walker moves along a one-dimensional lattice where its Hilbert space, $\mathcal{H}_P$, is spanned by $\{|i\rangle_P : i \in \mathbb{Z}\}$. The conditional shift operator that moves the walker is given by

$$
\widehat{S} = \begin{cases}
|00\rangle_C \otimes |i\rangle_P \Longrightarrow |00\rangle_C \otimes |i+1\rangle_P \\
|11\rangle_C \otimes |i\rangle_P \Longrightarrow |11\rangle_C \otimes |i-1\rangle_P \\
Otherwise \otimes |i\rangle_P \Longrightarrow Otherwise \otimes |i\rangle_P
\end{cases} \quad (2)
$$

The Hilbert space of the walker is given by $\mathcal{H} \equiv \mathcal{H}_P \otimes \mathcal{H}_C$ and the walk is performed by T times application of the evolution operator on initial state of the walker, $|\psi\rangle_{Fin} = [\widehat{S}\widehat{C}]^T [(\cos\eta \, |00\rangle_C + e^{I\phi} \sin\eta \, |11\rangle_C) \otimes |0\rangle_P]$.
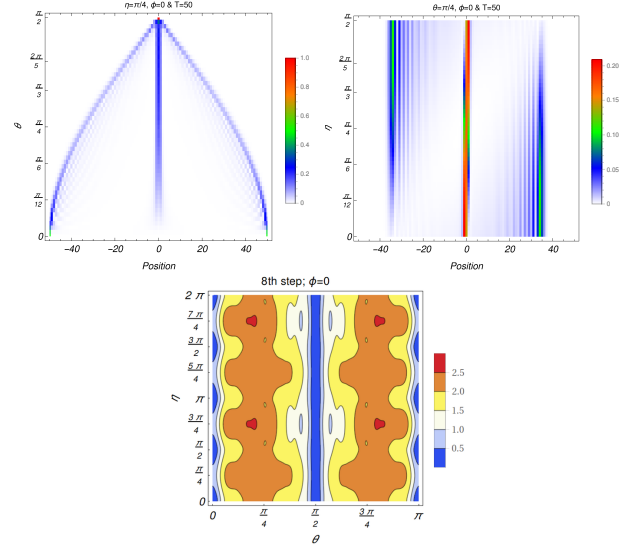
Figure 1: Up panels: probability density distribution in positions space as function of θ and η. Down panel: entropy of walk in position space at $8th$ step.

Evidently, the entanglement between two qubits could be used as a resource for obtaining different PDD in position space including classical like behavior to novel ones (up-left panel in Fig. 1). The symmetry of PDD (up-right panel in Fig. 1), its homogeneity, maximization of entropy (down panel in Fig. 1) and amplitudes of probability density in each position are functions of the amount of entanglement in the initial state. These show that the entangled qubits and the amount of entanglement between them could be means for state engineering and quantum simulation.

References

[1] N. Shenvi et al, Phys. Rev. A 67, 052307 (2003).

[2] M. Mohseni et al, J. Chem. Phys. 129, 174106 (2008).

[3] N. B. Lovett et al, Phys. Rev. A 81, 042330 (2010).

[4] A. Schreiber et al, Phys. Rev. Lett. 104, 050502 (2010).

[5] F. Zahringer et al, Phys. Rev. Lett. 104, 100503 (2010).

[6] R. Horodecki et al, Rev. Mod. Phys. 81, 865 (2009).

[*] shahram.panahiyan@uni-jena.de

[†] s.fritzsche@gsi.de

Publications

A. Adelmann, B. Hermann, R. Ischebeck, M. C. Kaluza, U. Locans, N. Sauerwein, and R. Tarkeshian
Real-Time Tomography of Gas-Jets with a Wollaston Interferometer
Applied Sciences-Basel **8**, 443 (2018).

P. Amaro, U. Loureiro, L. Safari, F. Fratini, P. Indelicato, T. Stohlker, and J. P. Santos
Quantum interference in laser spectroscopy of highly charged lithiumlike ions
Physical Review A **97**, 022510 (2018).

A. K. Arunachalam, M. B. Schwab, A. Savert, and M. C. Kaluza
Observation of non-symmetric side-scattering during high-intensity laser-plasma interactions
New Journal of Physics **20**, 033027 (2018).

R. Battesti et al.
High magnetic fields for fundamental physics
Physics Reports-Review Section of Physics Letters **765**, 1 (2018).

G. A. Becker et al.
Ring-like spatial distribution of laser accelerated protons in the ultra-high-contrast TNSA-regime
Plasma Physics and Controlled Fusion **60**, 055010 (2018).

W. Becker, S. P. Goreslavski, D. B. Milosevic, and G. G. Paulus
The plateau in above-threshold ionization: the keystone of rescattering physics
Journal of Physics B-Atomic Molecular and Optical Physics **51**, 162002 (2018).

K. Bergner, M. Muller, R. Klas, J. Limpert, S. Nolte, and A. Tunnerman
Scaling ultrashort laser pulse induced glass modifications for cleaving applications
Applied Optics **57**, 5941 (2018).

A. Bernhard et al.
Progress on experiments towards LWFA-driven transverse gradient undulator-based FELs
Nuclear Instruments and Methods in Physics Research Section a-Accelerators Spectrometers Detectors and Associated Equipment **909**, 391 (2018).

M. Bilal, A. V. Volotka, R. Beerwerth, and S. Fritzsche
Line strengths of QED-sensitive forbidden transitions in B-, Al-, F- and Cl-like ions
Physical Review A **97**, 052506 (2018).

J. H. Bin et al.
Enhanced Laser-Driven Ion Acceleration by Superponderomotive Electrons Generated from Near-Critical-Density Plasma
Physical Review Letters **120**, 074801 (2018).

A. Blinne, D. Schinkel, S. Kuschel, N. Elkina, S. G. Rykovanov, and M. Zepf
A systematic approach to numerical dispersion in Maxwell solvers
Computer Physics Communications **224**, 273 (2018).

A. A. Bondarevskaya et al.
Considerations towards the possibility of the observation of parity nonconservation in highly charged ions in storage rings
Physica Scripta **93**, 025401 (2018).

B. Boning, W. Paufler, and S. Fritzsche
Above-threshold ionization by few-cycle Bessel pulses carrying orbital angular momentum
Physical Review A **98**, 023407 (2018).

S. Breitkopf, N. Lilienfein, T. Achtnich, C. Zwyssig, A. Tunnermann, I. Pupeza, and J. Limpert
Velocity- and pointing-error measurements of a 300-r/min self-bearing permanant-magnet motor for optical applications
Review of Scientific Instruments **89**, 063110 (2018).

J. Buldt, M. Muller, R. Klas, T. Eidam, J. Limpert, and A. Tunnermann
Temporal contrast enhancement of a femtosecond fiber CPA system by filtering of SPM broadened spectra
in Fiber Lasers Xv: Technology and Systems, edited by I. Hartl, and A. L. Carter , (2018).

C. Buth, R. Beerwerth, R. Obaid, N. Berrah, L. S. Cederbaum, and S. Fritzsche
Neon in ultrashort and intense x-rays from free electron lasers
Journal of Physics B-Atomic Molecular and Optical Physics **51**, 055602 (2018).

M. Chemnitz, C. Gaida, M. Gebhardt, F. Stutzki, J. Kobelke, A. Tunnermann, J. Limpert, and M. A. Schmidt
Carbon chloride-core fibers for soliton mediated supercontinuum generation
Optics Express **26**, 3221 (2018).

M. Chemnitz et al.
Thermodynamic control of soliton dynamics in liquid-core fibers
Optica **5**, 695 (2018).

J. M. Cole et al.
Experimental Evidence of Radiation Reaction in the Collision of a High-Intensity Laser Pulse with a Laser-Wakefield Accelerated Electron Beam
Physical Review X **8**, 011020 (2018).

J. G. Cubiss et al.
Charge radii and electromagnetic moments of At195-211
Physical Review C **97**, 054327 (2018).

J. Deprince, P. Palmeri, P. Quinet, S. Fritzsche, M. Bautista, C. Mendoza, T. R. Kallman, and J. A. Garcia
Plasma-Environment Effects on the Atomic Structure and K Lines of He- and Li-like Oxygen Ions
in Workshop on Astrophysical Opacities, edited by C. Mendoza, S. TurckChieze, and J. Colgan , 289 (2018).

J. Ding, D. Schumacher, D. Jahn, A. Blazevic, and M. Roth
Simulation studies on generation, handling and transport of laser-accelerated carbon ions
Nuclear Instruments and Methods in Physics Research Section a-Accelerators Spectrometers Detectors and Associated Equipment **909**, 168 (2018).

V. Dinu and G. Torgrimsson
Trident pair production in plane waves: Coherence, exchange, and spacetime inhomogeneity
Physical Review D **97**, 036021 (2018).

C. Gaida et al.
Watt-scale super-octave mid-infrared intrapulse difference frequency generation
Light-Science and Applications **7**, 94 (2018).

C. Gaida, M. Gebhardt, T. Heuermann, F. Stutzki, C. Jauregui, and J. Limpert
Ultrafast thulium fiber laser system emitting more than 1 kW of average power
Optics Letters **43**, 5853 (2018).

C. Gaida et al.
High-power frequency comb at 2 mu m wavelength emitted by a Tm-doped fiber laser system
Optics Letters **43**, 5178 (2018).

T. Gassner et al.
Wavelength-dispersive spectroscopy in the hard x-ray regime of a heavy highly-charged ion: the 1s Lamb shift in hydrogen-like gold
New Journal of Physics **20**, 073033 (2018).

M. Gebhardt et al.
Nonlinear pulse compression stage delivering 43-W few-cycle pulses with GW peak-power at 2-mu m wavelength
in Fiber Lasers Xv: Technology and Systems, edited by I. Hartl, and A. L. Carter , (2018).

E. Gelfer, N. Elkina, and A. Fedotov
Unexpected impact of radiation friction: enhancing production of longitudinal plasma waves
Scientific Reports **8**, 6478 (2018).

H. Gies, F. Karbstein, and C. Kohlfurst
All-optical signatures of strong-field QED in the vacuum emission picture
Physical Review D **97**, 036022 (2018).

H. Gies, F. Karbstein, C. Kohlfurst, and N. Seegert
Photon-photon scattering at the high-intensity frontier
Physical Review D **97**, 076002 (2018).

H. Gies and R. Martini
Curvature bound from gravitational catalysis
Physical Review D **97**, 085017 (2018).

H. Gies and R. Sondenheimer
Renormalization group flow of the Higgs potential
Philosophical Transactions of the Royal Society a-Mathematical Physical and Engineering Sciences **376**, 20170120 (2018).

J. S. M. Ginges and A. V. Volotka
Testing atomic wave functions in the nuclear vicinity: The hyperfine structure with empirically deduced nuclear and quantum electrodynamic effects
Physical Review A **98**, 032504 (2018).

B. Goswami, A. V. Volotka, and S. Fritzsche
Influence of a stray magnetic field on the measurement of long-range spin-spin interaction
Journal of Physics Communications **2**, 055025 (2018).

T. Grigorova, R. Sollapur, A. Hoffmann, A. Hartung, A. Schwuchow, J. Bierlich, J. Kobelke, M. A. Schmidt, and C. Spielmann
Measurement of the Dispersion of an Antiresonant Hollow Core Fiber
Ieee Photonics Journal **10**, 7104406 (2018).

M. M. Günther, A. V. Volotka, M. Jentschel et al.
Dispersive refraction of different light to heavy materials at MeV gamma-ray energies
Physical Review A **97**, 063843 (2018).

S. H. Hendi, B. E. Panah, and S. Panahiyan
Black Hole Solutions in Gauss-Bonnet-Massive Gravity in the Presence of Power-Maxwell Field
Fortschritte Der Physik-Progress of Physics **66**, 1800005 (2018).

S. H. Hendi, B. E. Panah, S. Panahiyan, H. Liu, and X. H. Meng
Black holes in massive gravity as heat engines
Physics Letters B **781**, 40 (2018).

S. H. Hendi, B. E. Panah, S. Panahiyan, and M. Momennia
Magnetic solutions in Einstein-massive gravity with linear and nonlinear fields
European Physical Journal C **78**, 432 (2018).

S. Herzer et al.
An investigation on THz yield from laser-produced solid density plasmas at relativistic laser intensities
New Journal of Physics **20**, 063019 (2018).

T. Heuermann, C. Gaida, M. Gebhardt, and J. Limpert
Thulium-doped nonlinear fiber amplifier delivering 50 fs pulses at 20 W of average power
Optics Letters **43**, 4441 (2018).

C. M. Heyl, S. B. Schoun, G. Porat, H. Green, and J. Ye
A nozzle for high-density supersonic gas jets at elevated temperatures
Review of Scientific Instruments **89**, 113114 (2018).

P. Hilz et al.
Isolated proton bunch acceleration by a petawatt laser pulse
Nature Communications **9**, 423 (2018).

84

J. Hofbrucker, A. V. Volotka, and S. Fritzsche
Maximum Elliptical Dichroism in Atomic Two-Photon Ionization
Physical Review Letters **121**, 053401 (2018).

D. Hoff, F. J. Furch, T. Witting, K. Ruhle, D. Adolph, A. M. Sayler, M. J. J. Vrakking, G. G. Paulus, and C. P. Schulz
Continuous every-single-shot carrier-envelope phase measurement and control at 100 kHz
Optics Letters **43**, 3850 (2018).

Y. Hua et al.
87-W 1018-nm Yb-fiber ultrafast seeding source for cryogenic Yb: yttrium lithium fluoride amplifier
Optics Letters **43**, 1686 (2018).

K. Hutten et al.
Ultrafast quantum control of ionization dynamics in krypton
Nature Communications **9**, 719 (2018).

D. Jahn et al.
First application studies at the laser-driven LIGHT beamline: Improving proton beam homogeneity and imaging of a solid target
Nuclear Instruments and Methods in Physics Research Section a-Accelerators Spectrometers Detectors and Associated Equipment **909**, 173 (2018).

D. Jahn et al.
Chemical-vapor deposited ultra-fast diamond detectors for temporal measurements of ion bunches
Review of Scientific Instruments **89**, 093304 (2018).

C. Jauregui, J. Limpert, A. Tunnermann

Ieee, Ultra-large mode area fibers for high power lasers2018), 2018 Optical Fiber Communications Conference and Exposition , (2018).

C. Jauregui, C. Stihler, A. Tunnermann, and J. Limpert
Pump-modulation-induced beam stabilization in high-power fiber laser systems above the mode instability threshold
Optics Express **26**, 10691 (2018).

C. Jauregui, C. Stihler, A. Tunnermann, and J. Limpert
Transverse mode instabilities in burst operation of high-power fiber laser systems
in Fiber Lasers Xv: Technology and Systems, edited by I. Hartl, and A. L. Carter , (2018).

C. Jauregui, F. Stutzki, A. Tunnermann, and J. Limpert
Thermal analysis of Yb-doped high-power fiber amplifiers with Al:P co-doped cores
Optics Express **26**, 7614 (2018).

N. Jayakumar et al.
Polarization evolution in single-ring antiresonant hollow-core fibers
Applied Optics **57**, 8529 (2018).

F. Karbstein
Vacuum birefringence in the head-on collision of x-ray free-electron laser and optical high-intensity laser pulses
Physical Review D **98**, 056010 (2018).

F. Karbstein and E. A. Mosman
Photon polarization tensor in circularly polarized Hermite- and Laguerre-Gaussian beams
Modern Physics Letters A **33**, 1850044 (2018).

F. Karbstein, M. Wagner, and M. Weber
Determination of Lambda(nf=2)/MS and analytic parametrization NIS of the static quark-antiquark potential
Physical Review D **98**, 114506 (2018).

V. Y. Kharin, D. Seipt, and S. G. Rykovanov
Higher-Dimensional Caustics in Nonlinear Compton Scattering
Physical Review Letters **120**, 044802 (2018).

J. Kirtzel, S. Madhavan, N. Wielsch, A. Blinne, Y. Hupfer, J. Linde, K. Krause, A. Svatos, and E. Kothe
Enzymatic Bioweathering and Meta l Mobilization From Black Slate by the Basidiomycete Schizophyllum commune
Frontiers in Microbiology **9**, 2545 (2018).

R. Klas, A. Kirsche, M. Tschernajew, J. Rothhardt, and J. Limpert
Annular beam driven high harmonic generation for high flux coherent XUV and soft X-ray radiation
Optics Express **26**, 19318 (2018).

A. Kleinschmidt et al.
Intense, directed neutron beams from a laser-driven neutron source at PHELIX
Physics of Plasmas **25**, 053101 (2018).

A. Klenke, M. Muller, H. Stark, M. Kienel, C. Jauregui, A. Tunnermann, and J. Limpert
Coherent Beam Combination of Ultrafast Fiber Lasers
Ieee Journal of Selected Topics in Quantum Electronics **24**, 0902709 (2018).

A. Klenke, M. Muller, H. Stark, F. Stutzki, C. Hupel, T. Schreiber, A. Tunnermann, and J. Limpert
Coherently combined 16-channel multicore fiber laser system
Optics Letters **43**, 1519 (2018).

A. Klenke, M. Muller, H. Stark, A. Tunnermann, and J. Limpert
Sequential phase locking scheme for a filled aperture intensity coherent combination of beam arrays
Optics Express **26**, 12072 (2018).

C. Kohlfurst
Phase-space analysis of the Schwinger effect in inhomogeneous electromagnetic fields
European Physical Journal Plus **133**, 191 (2018).

C. Kohlfurst and R. Alkofer
Ponderomotive effects in multiphoton pair production
Physical Review D **97**, 036026 (2018).

J. Korner et al.
Spectroscopic investigations of thulium doped YAG and YAP crystals between 77 K and 300 K for short-wavelength infrared lasers
Journal of Luminescence **202**, 427 (2018).

V. P. Kosheleva, V. A. Zaytsev, A. Surzhykov, V. M. Shabaev, and T. Stohlker
Elastic scattering of twisted electrons by an atomic target: Going beyond the Born approximation
Physical Review A **98**, 022706 (2018).

T. Kurz et al.
Calibration and cross-laboratory implementation of scintillating screens for electron bunch charge determination
Review of Scientific Instruments **89**, 093303 (2018).

S. Kuschel, M. B. Schwab, M. Yeung, D. Hollatz, A. Seidel, W. Ziegler, A. Savert, M. C. Kaluza, and M. Zepf
Controlling the Self-Injection Threshold in Laser Wakefield Accelerators
Physical Review Letters **121**, 154801 (2018).

R. Lachheb, A. Herrmann, A. A. Assadi, J. Reiter, J. Korner, J. Hein, C. Russel, R. Maalej, and K. Damak
Judd-Ofelt analysis and experimental spectroscopic study of erbium doped phosphate glasses
Journal of Luminescence **201**, 245 (2018).

B. F. Lei, J. W. Wang, V. Kharin, M. Zepf, and S. Rykovanov
gamma-Ray Generation from Plasma Wakefield Resonant Wiggler
Physical Review Letters **120**, 134801 (2018).

J. Limpert

Ieee, Toward multi-kW femtosecond fiber lasers based on mutlicore fibers 2018), 2018 Ieee Photonics Society Summer Topical Meeting Series , (2018).

Y. Lin, Y. G. Yuan, F. Fang, and Z. Y. Tan
A study of electric field distribution in Benjamin type proportional counter using finite element method
Applied Radiation and Isotopes **135**, 142 (2018).

A. V. Maiorova, S. Fritzsche, R. A. Muller, and A. Surzhykov
Elastic scattering of twisted electrons by diatomic molecules
Physical Review A **98**, 042701 (2018).

I. A. Maltsev, V. M. Shabaev, R. V. Popov, Y. S. Kozhedub, G. Plunien, X. Ma, and T. Stohlker
Electron-positron pair production in slow collisions of heavy nuclei beyond the monopole approximation
Physical Review A **98**, 062709 (2018).

J. Y. Mao et al.
Energy enhancement of the target surface electron by using a 200 TW sub-picosecond laser
Optics Letters **43**, 3909 (2018).

P. Micke et al.
The Heidelberg compact electron beam ion traps
Review of Scientific Instruments **89**, 063109 (2018).

M. Muller, A. Klenke, H. Stark, J. Buldt, T. Gottschall, A. Tunnermann, and J. Limpert
1.8 kW 16-channel ultrafast fiber laser system
in Fiber Lasers Xv: Technology and Systems, edited by I. Hartl, and A. L. Carter , (2018).

M. Muller, A. Klenke, A. Steinkopff, H. Stark, A. Tunnermann, and J. Limpert
3.5 kW coherently combined ultrafast fiber laser
Optics Letters **43**, 6037 (2018).

R. A. Muller et al.
Hyperfine interaction with the Th-229 nucleus and its low-lying isomeric state
Physical Review A **98**, 020503 (2018).

O. Novak, R. Kholodov, A. Surzhykov, A. N. Artemyev, and T. Stohlker
K-shell ionization of heavy hydrogenlike ions
Physical Review A **97**, 032518 (2018).

R. Obaid et al.
LCLS in-photon out: fluorescence measurement of neon using soft x-rays
Journal of Physics B-Atomic Molecular and Optical Physics **51**, 034003 (2018).

L. Obst-Huebl et al.
All-optical structuring of laser-driven proton beam profiles
Nature Communications **9**, 5292 (2018).

J. Palaudoux et al.
Selectivity of the Br 3d(-1) Auger decays in HBr
Physical Review A **98**, 043406 (2018).

B. E. Panah, S. H. Hendi, S. Panahiyan, and M. Hassaine
BTZ dilatonic black holes coupled to Maxwell and Born-Infeld electrodynamics
Physical Review D **98**, 084006 (2018).

S. Panahiyan and S. Fritzsche
Controlling quantum random walk with a step-dependent coin
New Journal of Physics **20**, 083028 (2018).

A. A. Peshkov, A. V. Volotka, A. Surzhykov, and S. Fritzsche
Rayleigh scattering of twisted light by hydrogenlike ions
Physical Review A **97**, 023802 (2018).

K. Poder et al.
Experimental Signatures of the Quantum Nature of Radiation Reaction in the Field of an Ultraintense Laser
Physical Review X **8**, 031004 (2018).

R. V. Popov, A. I. Bondarev, Y. S. Kozhedub, I. A. Maltsev, V. M. Shabaev, Tupitsyn, II, X. W. Ma, G. Plunien, and T. Stohlker
One-center calculations of the electron-positron pair creation in low-energy collisions of heavy bare nuclei
European Physical Journal D **72**, (2018).

S. Raeder et al.
Probing Sizes and Shapes of Nobelium Isotopes by Laser Spectroscopy
Physical Review Letters **120**, 232503 (2018).

M. Reichert, A. Eichhorn, H. Gies, J. M. Pawlowski, T. Plehn, and M. M. Scherer
Probing baryogenesis through the Higgs boson self-coupling
Physical Review D **97**, 075008 (2018).

O. N. Rosmej et al.
Generation of keV hot near-solid density plasma states at high contrast laser-matter interaction
Physics of Plasmas **25**, 083103 (2018).

J. Rothhardt, G. K. Tadesse, W. Eschen, and J. Limpert
Table-top nanoscale coherent imaging with XUV light
Journal of Optics **20**, 113001 (2018).

M. Ruijter, V. Y. Kharin, and S. G. Rykovanov
Analytical solutions for nonlinear Thomson scattering including radiation reaction
Journal of Physics B-Atomic Molecular and Optical Physics **51**, 225701 (2018).

S. G. Rykovanov, J. W. Wang, V. Y. Kharin, B. Lei, C. B. Schroeder, C. G. R. Geddes, E. Esarey, and W. P. Leemans
Plasma Channel Undulator for Narrow-Bandwidth X-Ray Generation
in X-Ray Lasers 2016, edited by T. Kawachi et al.2018 , 163 (2018).

G. M. Samarin, M. Zepf, and G. Sarri
Radiation reaction studies in an all-optical set-up: experimental limitations
Journal of Modern Optics **65**, 1362 (2018).

Z. Samsonova et al.
Hard X-ray Generation from ZnO Nanowire Targets in a Non-Relativistic Regime of Laser-Solid Interactions
Applied Sciences-Basel **8**, 1728 (2018).

T. K. Sato et al.
First Ionization Potentials of Fm, Md, No, and Lr: Verification of Filling-Up of 5f Electrons and Confirmation of the Actinide Series
Journal of the American Chemical Society **140**, 14609 (2018).

T. Saule, M. Hogner, N. Lilienfein, O. de Vries, M. Plotner, V. S. Yakovlev, N. Karpowicz, J. Limpert, and I. Pupeza
Cumulative plasma effects in cavity-enhanced high-order harmonic generation in gases
Apl Photonics **3**, 101301 (2018).

A. M. Sayler, E. Eckner, J. McKenna, B. D. Esry, K. D. Carnes, I. Ben-Itzhak, and G. G. Paulus
Nonunique and nonuniform mapping in few-body Coulomb-explosion imaging
Physical Review A **97**, 033412 (2018).

S. Schmidt et al.
The nuclear magnetic moment of Bi-208 and its relevance for a test of bound-state strong-field QED
Physics Letters B **779**, 324 (2018).

S. Schmidt, T. Murbock, Z. Andelkovic, G. Birkl, K. Konig, W. Nortershauser, R. C. Thompson, and M. Vogel
Sympathetic cooling in two-species ion crystals in a Penning trap
Journal of Modern Optics **65**, 538 (2018).

C. Schneider, G. Torgrimsson, and R. Schutzhold
Discrete worldline instantons
Physical Review D **98**, 085009 (2018).

K. S. Schulze
Fundamental limitations of the polarization purity of x rays
Apl Photonics **3**, 126106 (2018).

W. Schumaker et al.
Making pions with laser light
New Journal of Physics **20**, 073008 (2018).

P. Seidel et al.
Cryogenic Current Comparators for Larger Beamlines
Ieee Transactions on Applied Superconductivity **28**, 1601205 (2018).

V. P. Shevelko, Y. A. Litvinov, T. Stohlker, and I. Y. Tolstikhina
Lifetimes of relativistic heavy-ion beams in the High Energy Storage Ring of FAIR
Nuclear Instruments and Methods in Physics Research Section B-Beam Interactions with Materials and Atoms **421**, 45 (2018).

L. V. Skripnikov et al.
New Nuclear Magnetic Moment of Bi-209: Resolving the Bismuth Hyperfine Puzzle
Physical Review Letters **120**, 093001 (2018).

C. Stihler, C. Jauregui, A. Tunnermann, and J. Limpert
Modal energy transfer by thermally induced refractive index gratings in Yb-doped fibers
Light-Science and Applications **7**, 59 (2018).

C. Stihler, C. Jauregui, A. Tunnermann, and J. Limpert
Phase-shift evolution of the thermally-induced refractive index grating in high-power fiber laser systems induced by pump-power variations
Optics Express **26**, 19489 (2018).

C. Stihler, C. Jauregui, A. Tunnermann, and J. Limpert
Towards the control of the modal energy transfer in transverse mode instabilities
in Fiber Lasers Xv: Technology and Systems, edited by I. Hartl, and A. L. Carter , (2018).

L. Stoyanov, G. Maleshkov, M. Zhekova, I. Stefanov, D. N. Neshev, G. G. Paulus, and A. Dreischuh
Far-field pattern formation by manipulating the topological charges of square-shaped optical vortex lattices
Journal of the Optical Society of America B-Optical Physics **35**, 402 (2018).

L. Stoyanov, G. Maleshkov, M. Zhekova, I. Stefanov, G. G. Paulus, and A. Dreischuh
Far-field beam reshaping by manipulating the topological charges of hexagonal optical vortex lattices
Journal of Optics **20**, 095601 (2018).

A. Surzhykov, V. A. Yerokhin, S. Fritzsche, and A. V. Volotka
Diagnostics of polarization purity of x rays by means of Rayleigh scattering
Physical Review A **98**, 053403 (2018).

G. K. Tadesse et al.
High resolution XUV Fourier transform holography on a table top
Scientific Reports **8**, 8677 (2018).

I. Tamer, S. Keppler, M. Hornung, J. Korner, J. Hein, and M. C. Kaluza
Spatio-Temporal Characterization of Pump-Induced Wavefront Aberrations in Yb3+-Doped Materials
Laser and Photonics Reviews **12**, 1700211 (2018).

G. Torgrimsson, C. Schneider, and R. Schutzhold
Sauter-Schwinger pair creation dynamically assisted by a plane wave
Physical Review D **97**, 096004 (2018).

Tupitsyn, II, N. A. Zubova, V. M. Shabaev, G. Plunien, and T. Stohlker
Relativistic calculations of x-ray transition energies and isotope shifts in heavy atoms
Physical Review A **98**, 022517 (2018).

S. Upadhyay, S. H. Hendi, S. Panahiyan, and B. E. Panah
Thermal fluctuations of charged black holes in gravity's rainbow
Progress of Theoretical and Experimental Physics, 093e01 , (2018).

A. S. Varentsova, V. A. Agababaev, D. A. Glazov, A. M. Volchkova, A. V. Volotka, V. M. Shabaev, and G. Plunien
Interelectronic-interaction contribution to the nonlinear Zeeman effect in boronlike ions
Physical Review A **97**, 043402 (2018).

M. Vockert, G. Weber, U. Spillmann, T. Krings, T. Stohlker

Iop, in Fairness 2017: Fair Next Generation Scientists 20172018 , (2018).

L. J. Vormawah et al.
Isotope shifts from collinear laser spectroscopy of doubly charged yttrium isotopes
Physical Review A **97**, 042504 (2018).

J. W. Wang et al.
Very-long distance propagation of high-energy laser pulse in air
Physics of Plasmas **25**, 113111 (2018).

A. H. Woldegeorgis, B. Beleites, F. Ronneberger, R. Grosse, and A. Gopal
Investigating the influence of incident laser wavelength and polarization on particle acceleration and terahertz generation
Physical Review E **98**, 061201 (2018).

A. Woldegeorgis, T. Kurihara, M. Almassarani, B. Beleites, R. Grosse, F. Ronneberger, and A. Gopal
Multi-MV/cm longitudinally polarized terahertz pulses from laser-thin foil interaction
Optica **5**, 1474 (2018).

A. Woldegeorgis, T. Kurihara, B. Beleites, J. Bossert, R. Grosse, G. G. Paulus, F. Ronneberger, and A. Gopal
THz Induced Nonlinear Effects in Materials at Intensities above 26 GW/cm(2)
Journal of Infrared Millimeter and Terahertz Waves **39**, 667 (2018).

D. Wu, X. T. He, W. Yu, and S. Fritzsche
Particle-in-cell simulations of laser-plasma interactions at solid densities and relativistic intensities: the role of atomic processes
High Power Laser Science and Engineering **6**, e50 (2018).

D. Wu, W. Yu, Y. T. Zhao, S. Fritzsche, and X. T. He
Characteristics of X/gamma-ray radiations by intense laser interactions with high-Z solids: The role of bremsstrahlung and radiation reactions
Matter and Radiation at Extremes **3**, 293 (2018).

D. Wurzler, N. Eicke, M. Moller, D. Seipt, A. M. Sayler, S. Fritzsche, M. Lein, and G. G. Paulus
Velocity map imaging of scattering dynamics in orthogonal two-color fields
Journal of Physics B-Atomic Molecular and Optical Physics **51**, 015001 (2018).

P. Wustelt, F. Oppermann, L. Yue, M. Moller, T. Stohlker, M. Lein, S. Grafe, G. G. Paulus, and A. M. Sayler
Heteronuclear Limit of Strong-Field Ionization: Fragmentation of HeH+ by Intense Ultrashort Laser Pulses
Physical Review Letters **121**, 073203 (2018).

L. Yue, P. Wustelt, A. M. Sayler, F. Oppermann, M. Lein, G. G. Paulus, and S. Grafe
Strong-field polarizability-enhanced dissociative ionization
Physical Review A **98**, 043418 (2018).

U. Zastrau et al.
A sensitive EUV Schwarzschild microscope for plasma studies with sub-micrometer resolution
Review of Scientific Instruments **89**, 023703 (2018).

V. A. Zaytsev, A. S. Surzhykov, V. M. Shabaev, and T. Stohlker
Analysis of angular momentum properties of photons emitted in fundamental atomic processes
Physical Review A **97**, 043808 (2018).

D. Zille, D. Adolph, M. Moller, A. M. Sayler, and G. G. Paulus
Chirp and carrier-envelope-phase effects in the multiphoton regime: measurements and analytical modeling of strong-field ionization of sodium
New Journal of Physics **20**, 063018 (2018).

M. Zurch et al.
Coherent Diffraction Imaging with Tabletop XUV Sources
in X-Ray Lasers 2016, edited by T. Kawachi et al. , 231 (2018).

Theses

S. Fuchs

Optische Kohärenztomographie mit extrem ultravioletter Strahlung

Dissertation

Friedrich-Schiller-Universität, Physikalisch-Astronmische Fakultät, (2018).

M. Reuter

Characterisation of a Laser Wakefield Accelerator with Ultra-Short Probe Pulses

Dissertation

Friedrich-Schiller-Universität, Physikalisch-Astronmische Fakultät, (2018).

A. Peshkov

Interaction of atoms with twisted light

Dissertation

Friedrich-Schiller-Universität, Physikalisch-Astronmische Fakultät, (2018).

S. Kuschel

Erzeugung dichter Elektronenpulse mit Laser-Plasma-Beschleunigern für QED-Experimente in hohen Feldern

Dissertation

Friedrich-Schiller-Universität, Physikalisch-Astronmische Fakultät, (2018).

F. Kröger

Charge State Tailoring for Relativistic Heavy Ion Beams

Masterarbeit

Friedrich-Schiller-Universität, Physikalisch-Astronmische Fakultät, (2018).

B. Deng

Implementation of Imaging Technique for Observation of Laser Plasma Wakefield Acceleration inside Capillary Discharge Waveguide

Masterarbeit

Friedrich-Schiller-Universität, Physikalisch-Astronmische Fakultät, (2018).

F. Irshad

Single-Shot Optical Probing of Laser-Generated Plasmas

Masterarbeit

Friedrich-Schiller-Universität, Physikalisch-Astronmische Fakultät, (2018).

A. Massinger

Aufbau und Charakterisierung eines zeitaufgelösten 2D Plasma Anrege-Abfrage-Systems

Masterarbeit

Friedrich-Schiller-Universität, Physikalisch-Astronmische Fakultät, (2018).

N. Sahraei

Simulation, Fabrication and Analysis of γ-ray Planar Parabolic Compound Refractive Lenses

Masterarbeit

Friedrich-Schiller-Universität, Physikalisch-Astronmische Fakultät, (2018).

B. Baghdasaryan

Two-color above-threshold ionization of atoms and ions

Bachelorarbeit

Friedrich-Schiller-Universität, Physikalisch-Astronmische Fakultät, (2018).

P. Abele

Above-threshold ionization of atoms in different initial states

Bachelorarbeit

Friedrich-Schiller-Universität, Physikalisch-Astronmische Fakultät, (2018).

V. Neef

Charakterisierung eines Mikroskops zum Zweck der Untersuchung von Laser-Plasma-Wechselwirkungen am JETI-100-Lasersystem

Bachelorarbeit

Friedrich-Schiller-Universität, Physikalisch-Astronmische Fakultät, (2018).

F. P. G. Stehr

Aufbau, Charakterisierung und Anwendung eines optischen Systems zur Charakterisierung relativistischer Elektronenpulse

Bachelorarbeit

Friedrich-Schiller-Universität, Physikalisch-Astronmische Fakultät, (2018).

P. Luckner

Entwicklung, Aufbau und Charakterisierung eines optischen, hochgenauen Target-Positioniersystems

Bachelorarbeit

Friedrich-Schiller-Universität, Physikalisch-Astronmische Fakultät, (2018).

B. Arndt

Time-of-flight Measurements at HILITE

Bachelorarbeit

Friedrich-Schiller-Universität, Physikalisch-Astronmische Fakultät, (2018).

S. Supp

Schichtdickenmessung durch Interferenz an dünnen Flüssigkeitsfilmen

Wissenschaftliche Hausarbeit (Lehramt Gymnasium)

Friedrich-Schiller-Universität, Physikalisch-Astronmische Fakultät, (2018).